UNIVERSITY OF SOUTHAMPTON

FACULTY OF NATURAL AND ENVIRONMENTAL SCIENCES

Biomedical Sciences

Utilising high resolution imaging to interrogate blood vessel and bone cell interactions

by

Juan Antonio Núñez Muñoz

Thesis for the degree of Doctor of Philosophy

April 2018

UNIVERSITY OF SOUTHAMPTON

ABSTRACT

FACULTY OF NATURAL AND ENVIRONMENTAL SCIENCES

Thesis for the degree of Doctor of Philosophy

Utilising high resolution imaging to interrogate blood vessel and bone cell interactions

Juan Antonio Núñez Muñoz

Fragility fractures represent a socio-economic burden, yet effective systematic treatments for the prevention of osteoporotic fractures are still lacking. Bone is a dynamic and highly vascularised tissue. Evidence suggests that with ageing, low bone mass and disruption of the microstructure and mechanical properties could be driven by reduced vascular supply and blood vessel attracting signals. However, it remains unclear whether alterations in the intracortical vasculature occur with age and if preservation of the cortical vasculature could prevent bone fractures. The main objective of this PhD was to develop and utilise high resolution micro-computed tomography (μCT) imaging ex-vivo of cortical bone microstructure to test the hypothesis that bone vascular networks are altered with age. The following aims have been addressed i) To develop an image processing and analysis framework that allows for systematic measurement of the 3D architecture of cortical porosity comprising vascular canal networks and osteocyte lacunae in murine cortical bone ii) Application and validation of developed methodology to assess the effects of age on vascular canal phenotype iii) Extension of methodology to a unique transgenic mouse strain were osteoblast-derived vascular endothelial growth factor (VEGF) has been deleted iv) Application of phase-contrast enhanced X-ray tomography imaging to visualise soft tissue within vascular canal networks. Using both desktop μCT (1.7 μm) and synchrotron X-ray tomography (0.65 μm), cortical bone microstructure was assessed at a sufficient spatial resolution to detect and extract cortical porosity. Extracted porosity measurements from synchrotron X-ray tomography were classified into vascular canals and osteocyte lacunae and 3D spatial relationships computed. First, the tibiofibular junction from 15-week and 10-month-old female C57BL/6J mice (n=6) was selected and vascular networks compared. It was found that the posterior region of the tibiofibular junction had a higher vascular canal volume than the anterior, lateral and medial regions (+127.62%, 693.08% and 659.64% respectively, $p<0.05$) at 15 weeks of age. By 10 months, bone cortices were thinner (-13.04%, $p<0.01$) and reduction in vascular density was evident in the posterior region (-46.54%, $p<0.01$) providing the first evidence for location of the intracortical vasculature impacting age related effects on bone porosity. To explore the effect of osteoblast-derived VEGF on the intracortical microstructure, VEGF was knocked out (KO) in mature osteocalcin (Ocn) expressing osteoblasts. Again, the tibiofibular junctions of aged (1 year) wildtype (WT) and transgenic (VEGF Ocn KO) female mice (n=5) were imaged, analysed and compared. Results revealed that the lack of osteoblast-derived VEGF increased total porosity (vascular networks and osteocyte lacunae combined) in the tibiofibular junction (+39.92%, $p<0.01$) with changes evident in the anterior and posterior compartments. Attempts to extend the use of the developed methodology to separate osteocyte lacunae from vascular canals was unsuccessful in the VEGF Ocn KO model due to low mineralised matrix in the VEGF Ocn KO bones. Finally, an approach that allows the 3D visualisation and assessment of the soft tissues in calcified bone using phase contrast-enhanced X-ray tomography has been reported. Using this technique, vascular structures were detected within 95.77% of the intracortical canals of the murine tibiofibular junction, supporting the theory that the intracortical network is the living space of the bone vasculature. This project has developed novel methodology which has allowed demonstration of an age-related reduction in the intracortical vasculature associated with reduced cortical bone thickness and deleterious changes in bone porosity due to the lack of VEGF, thus supporting further investigations into targeting the blood supply to treat age-related bone disease.

Table of Contents

List of Tables

List of Figures

DECLARATION OF AUTHORSHIP

I, Juan Antonio Núñez Muñoz declare that this thesis and the work presented in it are my own and has been generated by me as the result of my own original research.

“Utilising high resolution imaging to interrogate blood vessel and bone cell interactions”

I confirm that:

1. This work was done wholly or mainly while in candidature for a research degree at this University;
2. Where any part of this thesis has previously been submitted for a degree or any other qualification at this University or any other institution, this has been clearly stated;
3. Where I have consulted the published work of others, this is always clearly attributed;
4. Where I have quoted from the work of others, the source is always given. With the exception of such quotations, this thesis is entirely my own work;
5. I have acknowledged all main sources of help;
6. Where the thesis is based on work done by myself jointly with others, I have made clear exactly what was done by others and what I have contributed myself;
7. Parts of this work have been published as:

Papers

- Núñez JA, Goring A, Hesse E, Thurner PJ, Schneider P, Clarkin CE. (2017) Simultaneous visualisation of calcified bone microstructure and intracortical vasculature using synchrotron X-ray phase contrast-enhanced tomography. Scientific Reports.

- Núñez JA, Goring A, Javaheri B, Gomez-Nicola Diego, Hesse E, Pitsillides AA, Schneider P, Thurner PJ, Clarkin CE. (2017) Regional diversity in the murine cortical vascular network is revealed by synchrotron X-ray tomography and is reduced with age (2018). European Cells & Materials.

- Mosey H, Núñez JA, Goring A, Clarkin CE, Staines KA, Lee PD, Pitsillides AA, Javaheri B. (2017) Sost deficiency does not alter bone's lacunar or vascular porosity. Frontiers in Materials.

Abstracts

- Núñez JA, Goring A, Thurner PJ, Schneider P, Clarkin CE. Utilising high resolution imaging to interrogate blood vessel and bone cell interactions. Medical Engineering Centres Annual Meeting and Bioengineering 2014. Imperial College, London.
- Núñez JA, Goring A, Hesse E, Thurner PJ, Schneider P, Clarkin CE. Identification of regional diversity in blood vessel structure within murine cortical bone. Bone Research Society Meeting 2016. University of Liverpool.
- Núñez JA, Goring A, Hesse E, Thurner PJ, Schneider P, Clarkin CE. Age-related and site-specific changes in the intracortical vascular network revealed by high-resolution synchrotron X-ray computed tomography, MEIBioeng16. University of Oxford.
- Núñez JA, Goring A, Hesse E, Thurner PJ, Schneider P, Clarkin CE. Regional changes in cortical bone porosity in mice lacking vascular endothelial growth factor revealed by synchrotron X-ray tomography. Poster presentation. Cell biology: osteoblasts and bone formation. ECTS 2017. Salzburg, Austria.
- Núñez JA, Goring A, Hesse E, Thurner PJ, Schneider P, Clarkin CE. Simultaneous visualisation of calcified bone ultrastructure and intracortical vasculature using synchrotron X-ray phase-contrast tomography. ECTS 2017. Salzburg, Austria.

Signed: .....

Date:

Contributors

All experiments and data analysis were performed by the author with the following exception:

- Histological examination (in Chapters 4 and 6) was performed with help of Alice Goring, University of Southampton.
- Genotyping of transgenic animals (in Chapter 5) was performed with help of Alice Goring, University of Southampton.

Definitions and Abbreviations

µCT	micro-Computed Tomography
BMU	Basic Multicellular Unit
Cre	cyclisation recombinase
CT	Computed Tomography
DNA	deoxyribonucleic acid
DXA	Dual-energy X-ray Absorptiometry
FOV	Field of View
FRAX®	Fracture Risk Assessment Tool
HR-pQCT	High Resolution peripheral Quantitative Computed Tomography
KO	knockout
LoxP (or lox)	locus of X(cross)-over
Ocn Cre	mouse expressing Cre recombinase under the control of the osteocalcin promoter
Ocn	osteocalcin
OPG	osteoprotegerin
Osx	osterix

PCR	Polymerase Chain Reaction
pixel	picture element
PMMA	polymethacrylate
RANK	receptor activator of NF-κB
RANKL	receptor activator of NF-κB ligand
SLS	Swiss Light Source
SR	Synchrotron Radiation
TOMCAT	Beamline for TOmographic Microscopy and Coherent rAdiology experimenTs
$VEFG^{fl/fl}$	mouse carrying floxed alleles of VEGF
VEGF Ocn KO	mutant mouse where VEGF has been specifically deleted from osteoblasts (expressing osteocalcin)
VEGF Osx KO	mutant mouse where VEGF has been specifically deleted from osteoblast lineage cells (expressing osterix)
VEGF	Vascular Endothelial Growth Factor
voxel	volume element
WT	wild type

Chapter 1: Background

1.1 Fragility fractures: A growing global health problem

The human skeleton provides mechanical and protective function. It is a site for the regulation of calcium ion homeostasis and the production of blood cells (Boskey and Coleman, 2010). Bone integrity maintenance throughout life is a delicate business. Figure 1.1 illustrates the changes in skeletal calcium with age in men and women. In childhood and adolescence the skeleton increases in density and strength. Bones stop growing in length between the ages of 16 and 18, but bone density continues to increase slowly with a peak bone mass attained during the third decade of life. The regulation of peak bone mass is not well understood but a number of factors have been identified and the most important are genetic influences, physical activity and nutritional factors (Masi, 2008). The higher the peak bone mass gained at younger age, the longer the bone mass can be preserved.

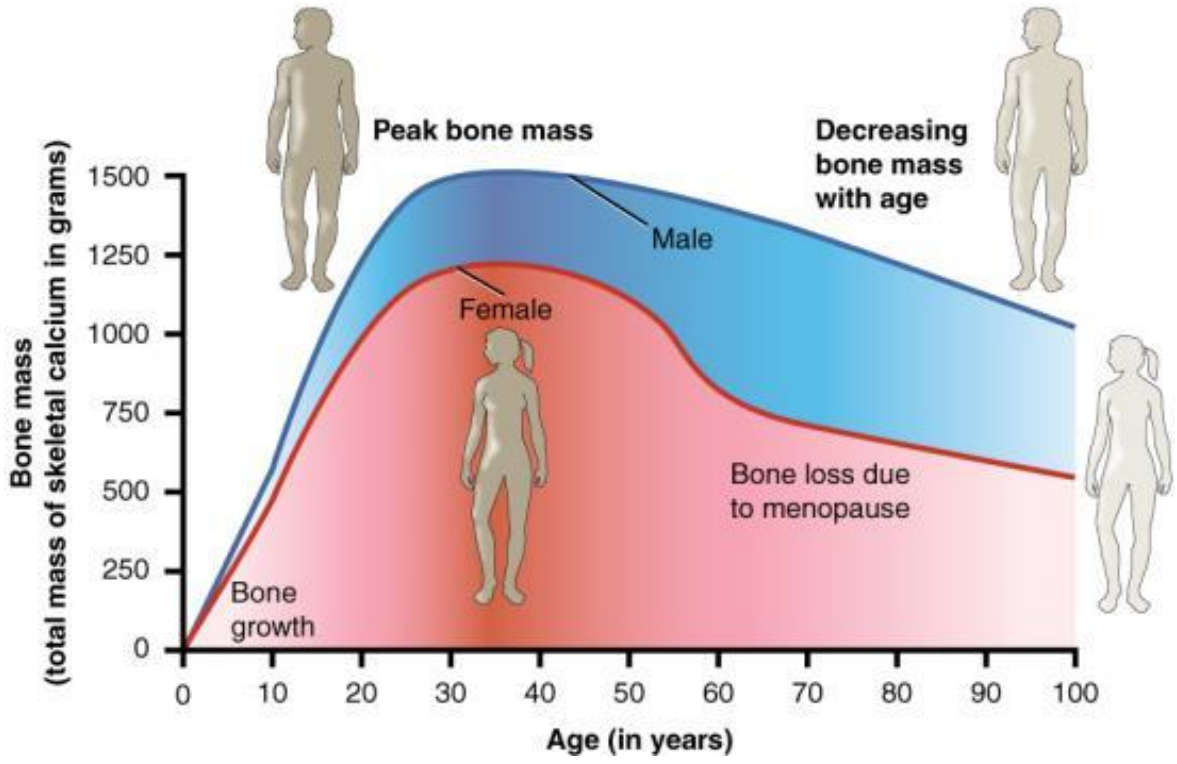

Figure 1.1. Changes in skeletal calcium with age – Bone density peaks at about 30 years of age. Women lose bone mass more rapidly than men (Young et al., 2003).

During adult life the mechanical integrity of the skeleton is maintained by a process called bone remodelling where bone demolition and new bone construction take place at the same time. After that bone loss increases gradually as part of the natural ageing process. This bone loss becomes more rapid in women for several years following the menopause since ovarian failure dramatically decreases estrogen secretion. Estrogen plays a pivotal role in the skeleton acting in order to conserve bone mass (Hughes et al., 1996; Manolagas, 2000). As with estrogen, the major action of testosterone at the tissue level is to reduce bone resorption (Bellido et al., 1995). Men, who do not experience sudden loss of gonadal sex steroid, have slower age-related bone loss but can lose about half as much bone with ageing as women (Clarke and Khosla, 2010).

Thus, as a result of the aging process, bones deteriorate with an accumulation of deleterious changes in geometry, mineralisation, organic matrix, porosity, cellular activity, ability for repair and strength in rodents and humans reported in the literature (Boskey and Coleman, 2010). Weaker bones are more susceptible to fracture and severe age-relate bone deterioration leads to osteoporosis. Osteoporosis literally means “porous bones”. The term is derived from the classical Greek words “osteo” which means bone and “porous” which means pore. The internationally agreed definition of osteoporosis is “a progressive systemic skeletal disease characterised by low bone mass and microarchitectural deterioration of bone tissue, with a consequent increase in bone fragility and susceptibility to fracture” (World Health Organization, 1994). Osteoporosis occurs when the bone mass decreases more quickly than the body can replace it, leading to a net loss of whole bone strength. As a result, the skeleton becomes fragile, so mechanical forces that would not ordinary result in fracture can lead to a broken bone. The broken bones can result in severe pain, significant disability and even mortality. Both hip and spinal fractures are also associated with a higher risk of death - 20% of those who suffer a hip fracture die within 6 months of the fracture (Åkesson et al., 2013).

Thus, osteoporosis and fragility fractures are age-associated. However, we still do to fully understand why this does not occurs in all individuals and it remains a major area of investigation. Individuals are arbitrarily defined as being osteoporotic when their bone mineral density (BMD) is >2.5 SD below the mean value among healthy young woman in

that population (Fogelman and Blake, 2000; Kanis, 2002). Dual-energy X-ray absorptiometry (DXA) scanning of the spine and hip remains the technique of choice for BMD assessment. The fundamental principle behind DXA is the measurement of the transmission through the body of X-rays of two different photon energy levels. Measurements at two energy levels enable the areal densities of two different types of tissue to be inferred, bone mineral and soft tissue. Spine and hip scanning are the most important measurement sites because they are frequent sites of fractures (Fogelman and Blake, 2000). Estimation of fracture risk can be performed with instruments such as Fracture Risk Assessment tool (FRAX®) to combine BMD measurements and risk factors and identify people that may be at risk of developing osteoporosis. Despite the fact that BMD is the most common diagnostic used to assess fracture risk, the mineral phase is only one of several constituents that make up the complex composite that is bone and some fractures cannot be explained by BMD alone, in fact up to 90% of the variation in strength cannot be explained by BMD (Müller, 2003). Bone quality depends on other parameters such us microarchitecture, prevalence of microcracks and bone matrix material properties (Thurner et al., 2010). Thus, broadening our understanding of bone physiological mechanisms not only has the potential to unravel new treatments but also influence the ways in which bone diseases are diagnosed.

Even though preventive strategies such as calcium, vitamin D and exercise may reduce the impact of age-related bone loss, many patients will become candidates for pharmacologic therapies. A variety of options are available: drug therapy may be divided into antiresorptive, anabolic and mixed effect. Antiresorptive drugs slow down the rate of bone dissolution whereas anabolic drugs stimulate bone formation. Estrogen replacement and bisphosphonates are examples of antiresorptive treatment options. However, after being used for the prevention and treatment of osteoporosis for many years, estrogen has been associated with a small increased risk for breast and uterine cancer (Blahos, 2007). Bisphosphonates (including alendronate and risendronate that are administered orally), on the other hand, produce a positive bone mass balance and increase bone strength in an initial stage. Nevertheless, they do this by inhibiting resorption which is important in bone remodelling and repair. Bone microdamage accumulation and reduced toughness are

disadvantages of the treatment with bisphosphonates which can lead to atypical fractures (Aspenberg and Schilcher, 2014). Teriparatide (parathyroid hormone 1–34 peptide) is a representative drug of the anabolic therapies. Teriparatide stimulates bone formation within a few weeks. However, with continued administration, the stimulatory effect begins to wane. Clinical practice has adopted the strategy of teriparatide use followed by an antiresorptive agent that will maintain and may even improve the bone mineral density response. However, their long term potential adverse effects are as yet unknown (Blahos, 2007; Stevenson, 2011). An example of mixed or dual model therapy is Strontium ranelate that increases bone formation and reduces bone resorption by stimulating osteoblast replication, differentiation and activity while slowing down osteoclast differentiation and activity (Demontiero et al., 2012). Clinical trials for sclerostin antibodies are currently being developed for the treatment of postmenopausal osteoporosis. Sclerostin is produced by osteocyte cells as a potent bone formation inhibitor that prevents osteoblastogeneis. Sclerostin blockade results in increased bone mass (Demontiero et al., 2012; MacNabb et al., 2016).

Worldwide, a fall from a standing height or less resulting in a fracture is estimated to occur every 3 seconds (Johnell and Kanis, 2006). The International Osteoporosis Foundation defines this type of injury as fragility fracture. Our bodies should be able to sustain a fall from this height, without a fracture, unless there is some underlying cause to suspect a bone disorder, like osteoporosis that weakens our bone structure.

Fragility fractures are common; at 50 years of age, one in three women and one in five men will suffer a fracture in their remaining lifetime (Dawson-Hughes et al., 2013). For women this risk is higher than the risk of breast, ovarian and uterine cancer combined. For men, the risk is higher than the risk for prostate cancer. Approximately 50% of people with one osteoporotic fracture will have another, with the risk of new fractures rising exponentially with each fracture (Dawson-Hughes et al., 2013).

The risk of sustaining a fracture increases exponentially with age due not only to the decrease in bone mass, but also due to the increased rate of falls among the elderly (Åkesson et al., 2013). The elderly represents the fastest growing segment of the

population. Thus as life expectancy increases for the majority of the world's population, the financial and human costs associated with osteoporotic fractures will increase dramatically (Åkesson et al., 2013).

Globally, during year 2000, there were an estimated 9 million new fragility fractures, of which 1.6 million were at the hip, 1.7 million at the wrist, 0.7 million at the humerus and 1.4 million symptomatic vertebral fractures (Johnell and Kanis, 2006). Europe and the Americas accounted for half of all these fractures, while most of the remainder occurred in the Western Pacific region and Southeast Asia (Johnell and Kanis, 2006).

The human suffering associated with these common serious injuries is immense and the financial costs are staggering. In 2005, the International Osteoporosis Foundation estimated the total direct cost of osteoporotic fractures in Europe to be 32 billion EUR per year (Kanis and Johnell, 2005), a figure which is projected to rise to 38.5 billion EUR by 2025 (Ström et al., 2011). In 2002, the combined cost of all osteoporotic fractures in the United States was estimated to be 20 billion USD per year (Cummings and Melton, 2002). The economic consequences of unchecked increases in the prevalence of osteoporosis amongst the rapidly ageing populations of Asia, Latin America and the Middle East must be a major concern for policy makers in these regions. In 2006, 1.6 billion USD was spent in China on hip fracture care, a figure that is set to rise to 12.5 billion USD by 2020 and 265 billion USD by 2050 (Mithal and Lau, 2009).

Osteoporotic fractures are one of the most common causes of disability and a major contributor to medical care costs in many regions of the world. During the next two decades, almost half a billion people will reach retirement age (Cooper et al., 2011). The number of fractures due to osteoporosis will increase causing significant disability, loss in quality of life and healthcare costs unless action is taken. Effective systematic treatments for the prevention of osteoporotic fractures are still lacking. Recent evidence has emerged that the bone loss in osteoporosis may be driven by reduced vascular supply and blood vessel attracting signals (Ding et al., 2011; Liu et al., 2012; Senel et al., 2013)(Ding et al., 2011; Liu et al., 2012; Senel et al., 2013). Evidence suggests that blood vessel attracting signals are reduced with age in multiple cell types (Efimenko et al., 2011; Jiang et al., 2008;

Pola et al., 2004; Rivard et al., 1999; Wilson et al., 2010) and reduced levels of circulating proangiogenic factors such as Vascular Endothelial Growth Factor (VEGF) have been found in postmenopausal osteoporotic women (Senel et al., 2013). However, further studies are needed to determine whether the vasculature could be a therapeutic target to treat age-related degenerative bone diseases.

1.2 Bone structure

The human skeleton gives the body its shape and provides physical support and protection for the systems contained within it. The skeleton accounts for approximately 20% of the total body mass. It forms part of the musculoskeletal system that enables us to move, provides an environment for blood cell production and acts as a storage area for minerals such as calcium. It is not a static organ, but is constantly changing to adjust to its environment (Clarke, 2008).

The structure of bone is optimised so that it is strong yet relatively light weight. These properties are conferred to a large degree by its architecture. Figure 1.2. shows the typical bone structure. The long bones are tubular in shape, with a strong outer shell, or cortical layer, surrounding a softer, spongier core called trabecular bone. The combination of the two tissues makes these bones strong and light, but flexible enough to absorb stress without failure. The amount of each type of tissue in bone is dependent on the function of the bone. For example, the vertebrae are similarly constructed, with a thick cortical layer surrounding sheets of trabecular bone (Parfitt, 2013). Blood vessels and nerves ramify through Haversian and Volkmann canals to irrigate and innervate the cortical tissue. The inner and outer surfaces of the bone tissue are covered inside and outside by connective tissue membranes, respectively the endosteum and periosteum.

Bone is a composite material, consisting of crystals of mineral bound to protein. Composites are formed by combining materials together to form an overall structure that is better than the sum of the individual components. The basic building block of the bone

material is the mineralized collagen fibril (Thurner, 2009). It is composed of the fibrous protein collagen in a structural form that is also present in skin, tendon, and a variety of other soft tissues. Type I collagen constitutes the main component of a three-dimensional matrix into which the mineral forms but there are hundreds of non-collagenous proteins that comprise less than 10% of the total protein content. Crystals of carbonate hydroxyapatite is the only mineral type in mature bone and provides hardness and stiffness. The importance of water for the mechanical functioning of bone cannot be underestimated: water is the third major component in bone and mechanical measurements of dry bone are different from those of wet bone. Figure 1.3 shows the multiscale structure of bone. Bone material has highly complex structures, described in terms of up to 7 hierarchical levels of organization, which range in scale from nanometres to millimetres. Mature bone is organised in a plywood-like structure called lamellae which has a regular parallel alignment of collagen into sheets (Weiner and Wagner D., 1998). The vertebrate skeleton has evolved to fulfil a variety of functions. The bones of vertebrates are all made from the same basic material (Taylor, 2000). Furthermore, specialised bone cells actively remove older bone and replace it with younger bone to repair damage and adapt to new mechanical requirements (Weiner and Wagner D., 1998).

As a metabolically active tissue, bone is composed of several types of cells. These cells include osteoclasts, osteoblasts, osteocytes and lining cells. Osteoclasts are the only cells that are known to be capable of resorbing bone. Activated multinucleated osteoclasts are derived from mononuclear precursor cells of the monocyte-macrophage lineage. Osteoclasts function in the resorption of mineralized tissue and are found attached to the bone surface at sites of active bone resorption. Their characteristic feature is a ruffled edge where active resorption takes place with the secretion of hydrogen ions and bone-resorbing enzymes. Secretion of hydrogen ions lowers the pH within the bone-resorbing compartment creating the conditions for an acidic environment that can be as low as 4.5 and helps calcium mobilisation. The secreted bone-resorbing enzymes such as tartrate-resistant acid phosphatase, cathepsin K, matrix metalloproteinase 9 and gelatinase digest the organic phase of the matrix (Clarke, 2008). Osteoblasts synthesise new bone matrix on

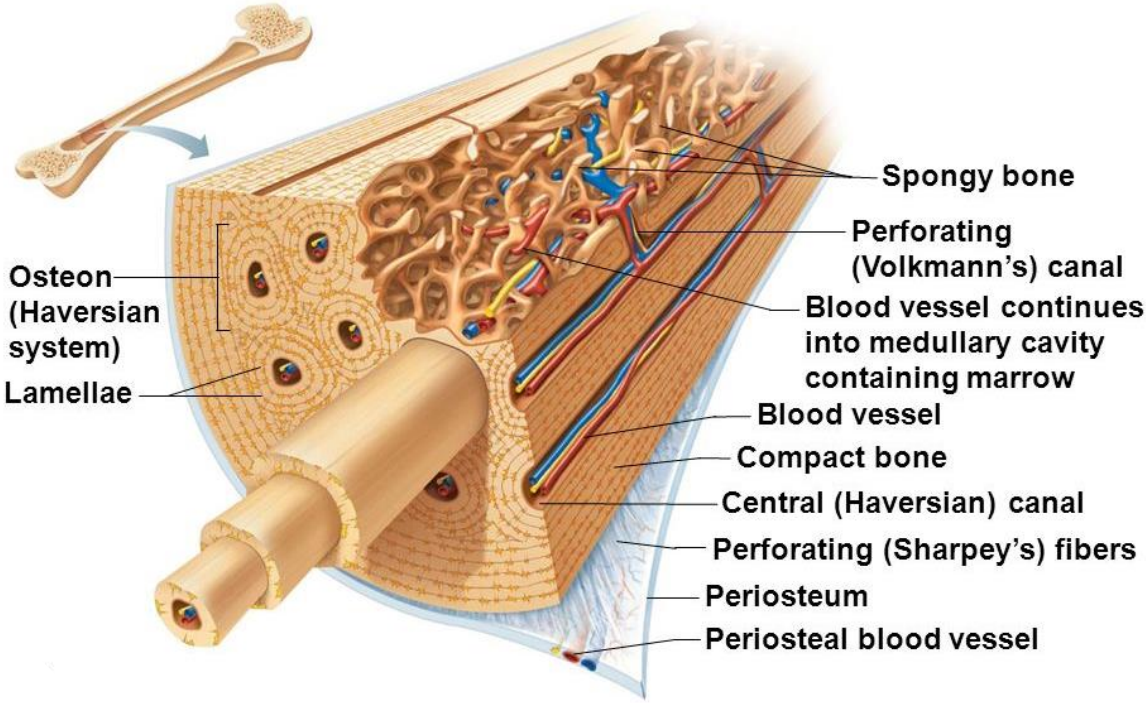

Figure 1.2. Human bone structure. Blood vessels ramify through Haversian and Volkmann canals in the cortex (Marieb, 2015).

bone-forming surfaces and are responsible for its subsequent mineralisation. They produce new collagenous organic matrix and control mineralisation. Osteoblasts release vesicles that concentrate calcium and phosphate and enzymatically destroy mineralisation inhibitors such as pyrophosphate or proteoglycans (Clarke, 2008). Osteoblast cells are derived from mesenchymal stem cells. Osteocytes represent terminally differentiated osteoblasts that become incorporated within the newly formed osteoid, which eventually becomes calcified bone. Osteocyte lacunae are the spaces in the mineralised matrix where the osteocyte cells reside. These cells function within syncytial networks to support bone structure and metabolism and have extensive filopodial processes that lie within the canaliculi in mineralised bone. Osteocytes regulate exchange of mineral in the bone fluid

within lacunae and the canalicular network. Osteocyte cells maintain connection with each other and the bone surface via their multiple filopodial cellular processes. They are thought to be ideally situated to respond to changes in physical forces upon bone and to transduce messages to cells on the bone surface, directing them to initiate resorption or formation responses (Clarke, 2008). The majority of bone surfaces that are not undergoing formation or resorption are lined by bone lining cells. Lining cells are thought to be quiescent osteoblasts. They serve as a blood-bone barrier and retain the ability to redifferentiate into osteoblasts upon exposure to parathyroid hormone or mechanical forces. Protective lining cells may also regulate influx and efflux off mineral ions into and out of bone extracellular fluid (Clarke, 2008). Lining cells contribute to bone remodelling by lifting off the surface of bone before resorption to form a specialised microenvironment where osteoclast can work Figure 1.4 and Figure 1.5 illustrate the different bone cell types.

The shape and size of both cortical and trabecular bone can be altered in response to different kinds of stress produced by physical activity. For example, in most people the cortex of their dominant arm is larger than that of their non-dominant arm. The difference in cortex size is even larger for tennis players and other athletes who routinely use a dominant arm in their sporting activities (Rockville; Office of the Surgeon General (US), 2004). Throughout life, bones change in size, shape and position. Two processes guide these changes—modelling and remodelling.

Bone formation can occur as a single anabolic process (modelling) or coupled with a second catabolic process of bone resorption (remodelling). Modelling is when bone resorption and bone formation occur on separate surfaces (formation and resorption are not coupled). An example of this process is during long bone increases in length and diameter. Bone modelling occurs during birth to adulthood and is responsible for gain in skeletal mass and changes in skeletal form. Remodelling is the replacement of old tissue by new bone tissue. This mainly occurs in the adult skeleton to maintain bone integrity (Clarke, 2008). This process involves the coupling of bone formation and bone resorption. Bone resorption occurs first and takes approximately 2-4 weeks in each cycle, whereas (after the

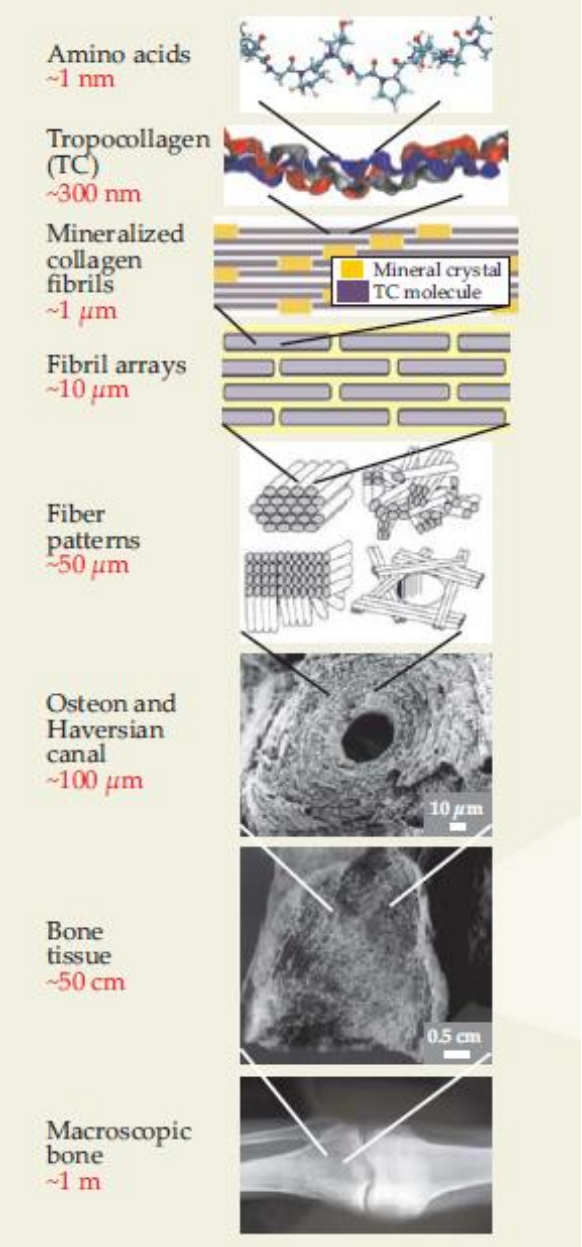

Figure 1.3. Multiscale structure of bone. Collagen protein molecules known as tropocollagen form from three chains of amino acids and provide the structural basis for mineralised collagen fibrils, the basic building blocks of bone. Several collagen fibrils, each linked by an organic phase, form fibril arrays. Each array makes up a single collagen fibre and several fibres form geometric patterns that provide structure to the cellular components of bone. The boundaries between packets of fibres create what are known as lamellar interfaces. That microstructure forms distinct mesoscale arrangements: compact or cortical bone and spongy or cancellous bone. Macroscopic cortical bone is complex. Osteons surround and protect blood vessels (Gerard J. Tortora and Nielsen, 2013).

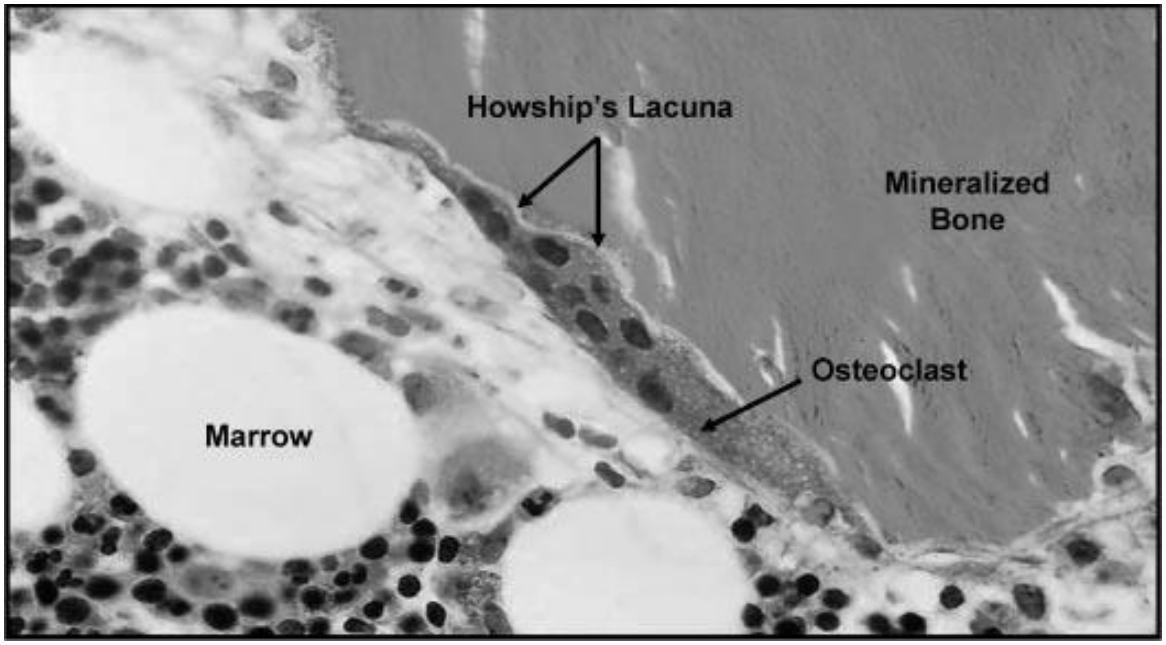

Figure 1.4. Osteoclast cells resorbing bone (Clarke, 2008).

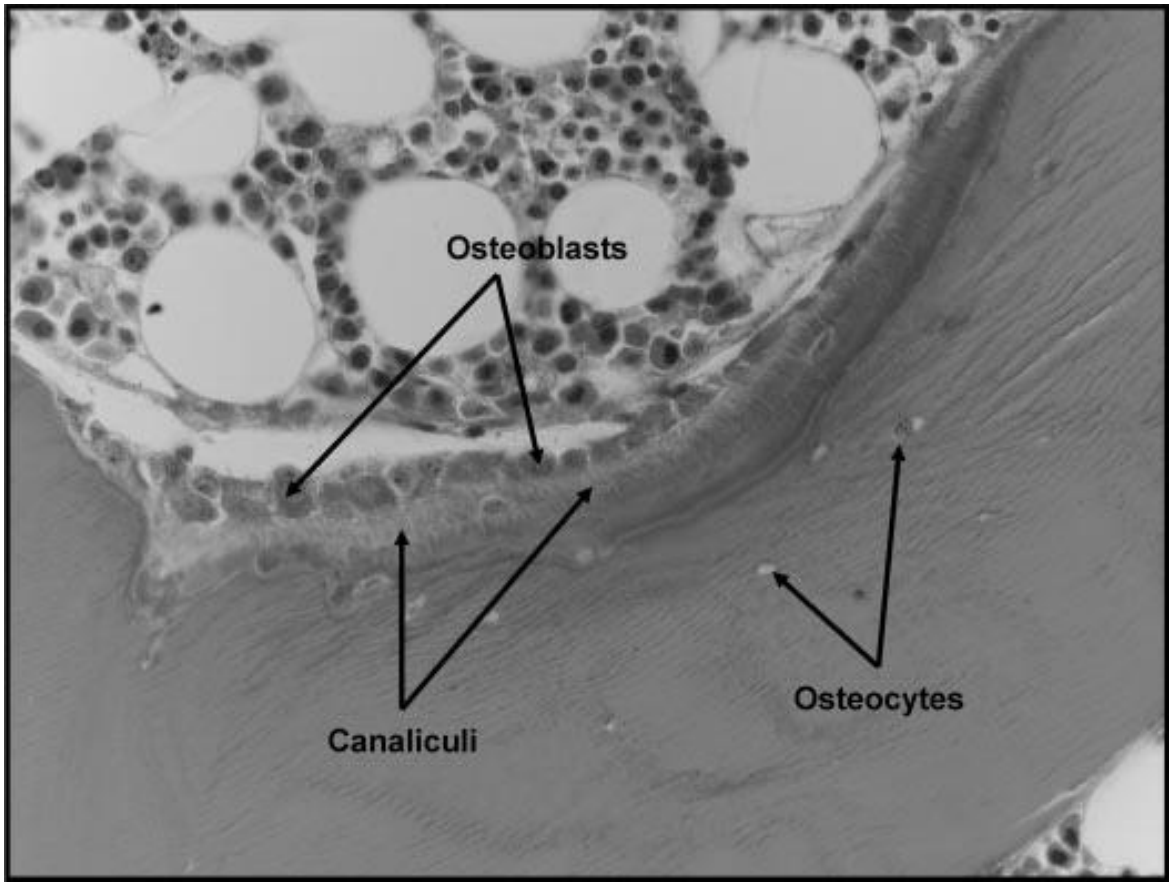

Figure 1.5. Osteoblasts forming new bone and osteocytes (Clarke, 2008).

reversal phase) bone formation phase takes approximately 2-4 months to complete (Clarke, 2008). Osteoclasts and osteoblasts work together in an enclosed compartment formed by a canopy formed by osteoblasts and lining cells. In cortical bone, the process of bone remodelling is carried out by a complex and unique structure, the basic multicellular unit (BMU) that comprises a cutting cone of osteoclasts in front and a closing cone lined by osteoblasts following behind (Parfitt, 1994). Figure 1.6 shows the structure of a BMU in cortical bone. Mechanical regulation and biochemical control have been hypothesised and investigated to explain how coupling between osteoclasts and osteoblasts in a BMU is regulated. Osteocytes, osteoblasts and lining cells respond to mechanical strain providing a mechanism for bone repair. Strain-induced osteocyte signals are thought to control the activity of osteoclasts and osteoblasts (van Oers et al., 2008). Cells in osteoblast and osteoclast lineages can also communicate with each other via diffusible paracrine factors such as RANK (receptor activator of NF-κB), RANKL (receptor activator of NF-κB ligand) and OPG (osteoprotegerin) at distinct phases of bone remodelling in a BMU (Matsuo and Irie, 2008).

Bone is a dynamic tissue that is constantly renewed throughout the life time. To respond to its dual roles of support and regulation of calcium and phosphorus, as well as to repair any damage to the skeleton, bone is constantly changing. This requires an exquisitely controlled regulatory system that involves specialized cells that communicate with each other. These cells must respond to many different signals, internal and external, mechanical and hormonal, and systemic and local. It is not surprising that with so many different tasks to perform and so many different factors regulating how the skeleton grows, adapts and responds to changing demands, there are many ways that these processes can go wrong.

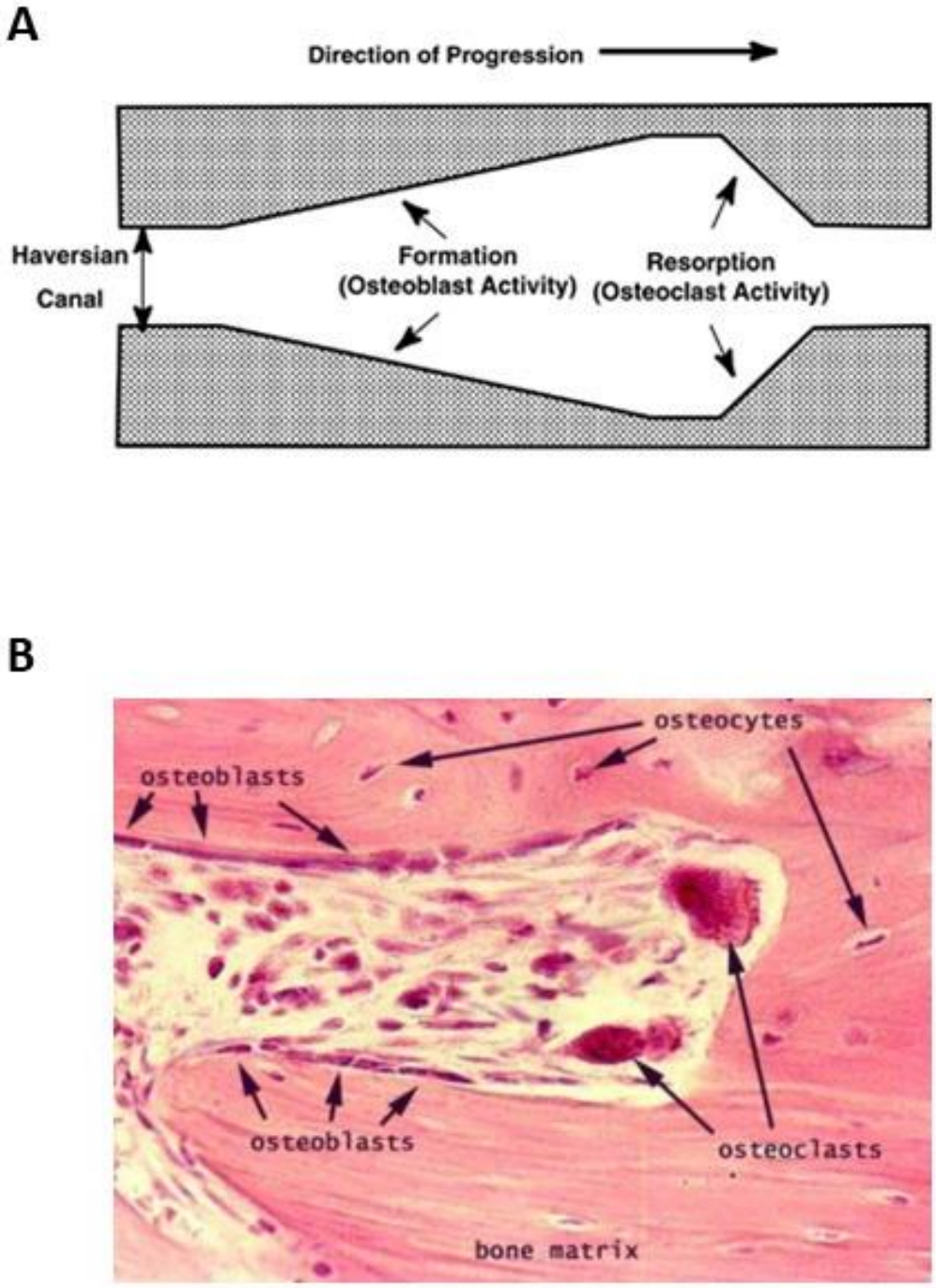

Figure 1.6. The Basic Multicellular Unit (BMU) in cortical bone. BMUs progress across bone with osteoclastic resorption leading the way. Soon after resorption is complete at a given location, osteoblasts begin to deposit osteoid. In cortical bone remodelling takes place in Haversian canals. (A) BMU diagram (Hernandez et al., 2000). (B) Histology section (haematoxylin and eosin staining) of a BMU.

1.3 Bone vasculature

For centuries, the vasculature has been thought to be a mere passive conduit for the transport and distribution of the blood fluid around the body. However, the intricate network of blood vessels plays a crucial role in the formation, homeostasis, and regeneration of adjacent organs and tissues. Organised in a hierarchical fashion, the vasculature delivers soluble factors and various types of cells to all tissues in a carefully regulated manner. Specialised endothelial cells, known for their remarkable heterogeneity and diverse functions (Cleaver and Melton, 2003; Garlanda and Dejana, 1997), line the entire circulatory system, from the heart to the smallest capillaries, to form a complex and large organ capable of communicating with surrounding tissue and circulating cells. With so many tasks to perform and so many different regulatory factors that give them both sensory and effector capacities, it is not surprising that there are many ways that the processes they control can go astray. In fact, vascular dysfunction has been linked to the pathogenesis of a broad spectrum of the most devastating diseases of our time. A solid body of scientific literature reports on the involvement of vascular dysfunction in atherosclerosis, cancer (both tumour growth and metastasis), infectious diseases, stroke, heart disease, diabetes, kidney failure, Alzheimer's and other age-associated diseases (Le Couteur and Lakatta, 2010; Rajendran et al., 2013). As a result, the vasculature has proved to be a reliable tool for the diagnosis and treatment of many of these conditions.

Today, the role of the vasculature in skeletal pathology remains poorly understood as the structural nature of skeletal tissue has made it exceptionally difficult to directly investigate the vasculature within it. Bone blood vessels are deeply encased in the calcified tissue and techniques applicable to soft tissue are frequently difficult to apply to the skeleton, such as confocal laser scanning microscopy or light sheet microscopy (Georgiadis et al., 2016; Goggin et al., 2016). What we do know is that the processes of bone growth, mineralisation, repair and rejuvenation are dependent upon the vascular supply (Carano and Filvaroff, 2003; Carulli et al., 2013; Glowacki, 1998). Bone cells can communicate with the vasculature (de Castro et al., 2015; Clarkin et al., 2008; Hu and Olsen, 2016a; Prasadam et al., 2014) in normal conditions and a loss of this communication could be involved in the onset of bone pathologies.

Bone is highly vascularised throughout life and it was proposed in 1930 that the vascular network might be an active mediator of skeletal adaptation (Jaffe, 1930). Today, it is generally accepted that skeletal development and growth, bone modelling, remodelling as well as repair are entirely dependent upon direct interactions with the vascular supply (Carulli et al., 2013). Proximity to the bone vessels (Ham, 1952) also influences bone cell survival and the reduction of the blood supply induces a consequent decrease of bone forming activity (Carulli et al., 2013). Additionally, blood vessels are present in bone remodelling units, and it has been hypothesised that vasculature has a role in coordinating coupling between osteoclasts and osteoblasts (Parfitt, 2000).

The general association between ageing and bone vascular function has not been widely recognised (Alagiakrishnan et al., 2003; Brandi and Collin-Osdoby, 2006; Jaffe, 1930; Laroche, 2002). It has recently been shown however, that the oxygen consumption of human bone declines with age and that this is accompanied by decreased vascular conductance (Dinenno et al., 1999), which could have a direct effect on bone health. Moreover, the importance of the relationship between bone tissue and the vascular system is highlighted by the progression of age-related degenerative bone diseases, such as osteoporosis, where modifications in blood supply and reduced number of arterial capillaries in the bone marrow have been associated with bone loss (Alagiakrishnan et al., 2003; Burkhardt et al., 1987; Reeve et al., 1988). In addition, there are bone segments with a terminal vascularisation (proximal femur, carpal scaphoid, talus) that are typically at high risk due to the lack of an appropriate collateral vascular network and, in cases of alterations in their unique blood supply, bone metabolism and bone health are dramatically affected; more frequently by reduced bone formation activity (Carulli et al., 2013).

Endothelial cells in bone have been found to control blood flow by the production of vasodilators (Davis and Wood, 1992) and recent investigations have demonstrated that endothelial cells in trabecular tissue are functionally specialised and heterogeneous (Kusumbe et al., 2014). In particular, capillaries in trabecular tissue can be subdivided into two categories (identified as types L and H by Kusumbe et al) with one of the subtypes declining in number after adolescence. The authors of this study suggested that this finding

could influence interaction with osteogenic cells and could be linked to age-related bone changes. It is unknown if these different types of capillaries are present in cortical bone. What we know is that bone cells can communicate with the vasculature. Vascular Endothelial Growth Factor (VEGF) is the pivotal factor linking angiogenesis to bone growth and remodelling (Maes et al., 2010). VEGF has been thought to be a specific mitogen for vascular endothelial cells but VEGF's actions within adult bone appear to be complex and VEGF receptors and sensitivity to VEGF have been reported by both osteoblasts and osteoclasts (Clarkin and Gerstenfeld, 2013). VEGF family is a potent mitogen family for endothelial cells and has a key role in angiogenesis. Many members of the VEGF family have been found to control communication between osteoblasts and endothelial cells. VEGF-A has been the most studied member of the family and is one of the main promoters of angiogenesis. It belongs to a family of homodimeric proteins consisting of six-members: VEGF-A, VEGF-B, VEGF-C, VEGF-D, VEGF-E and placental growth factor. VEGF-A exists as several isoforms ($VEGF_{165}$, $VEGF_{189}$ and $VEGF_{206}$ being the predominant ones and sequestered in the extracellular matrix) (Clarkin and Gerstenfeld, 2013). All the VEGF-A isoforms can activate two tyrosine kinase receptors: VEGF receptor 1 and VEGF receptor 2. Receptor activation in endothelial cells induces phosphorylation and leads to the transduction of different signals promoting processes such as endothelial cell migration, proliferation and enhancement of angiogenesis (Clarkin and Gerstenfeld, 2013). Bone forming osteoblast cells appear to be a predominant source of pro-angiogenic VEGF (Clarkin et al., 2008) in bone and a reciprocal paracrine relationship between osteoblasts and endothelial cells has been reported to exist during fracture repair (Hu and Olsen, 2016a). VEGF has been identified as an essential mediator during the process of angiogenesis since disruption of a single VEGF allele and postnatal ablation of VEGF experiments have shown abnormal organ development because of defective vasculogenesis, angiogenesis and large vessel formation (Carmeliet et al., 1996; Ferrara et al., 1996; Gerber et al., 1999). Evidence indicates that VEGF leads to high bone mass phenotype and increased number of blood vessels when it is overexpressed (Maes et al., 2010) whereas the lack of VEGF in osteoprogenitors results in a reduced bone mass phenotype (Liu et al., 2012). Moreover, evidence indicates that bone angiogenesis is indispensable for bone gain induced by exercise since VEGF blockade fully prevents bone

adaptation to training (Yao et al., 2004). For all this, it is reasonable to hypothesize that VEGF is required for a healthy skeleton. However, reduced VEGF expression has been linked to the ageing of multiple cell types in several studies (Efimenko et al., 2011; Jiang et al., 2008; Pola et al., 2004; Rivard et al., 1999; Wilson et al., 2010), which could favour a deficient blood supply and change the bone mass dramatically. Indeed, loss of osteoblast derived pro-angiogenic VEGF in mice results in an osteoporotic phenotype and also negatively impacts fracture repair (Hu and Olsen, 2016a; Liu et al., 2012) and reduced levels of circulating VEGF have been found in postmenopausal women (Senel et al., 2013). In addition to VEGF, other factors such as calcitonin (Chigurupati et al., 2005) or parathyroid hormone-related protein (Isowa et al., 2010) have been linked to angiogenesis in bone.

In recent years the influence of oxygen tension and hypoxia on bone function has become a major research focus (Arnett, 2010). A reduced or disrupted blood supply causes hypoxia. Low oxygen tension values trigger a cascade of biochemical reactions and the transcription of hypoxia-regulated genes. These genes are involved in a variety of cellular processes including angiogenesis, energy metabolism, cell proliferation/survival and pH control (Marenzana and Arnett, 2013). Hypoxia is one of the most potent reported inducers of VEGF production in bone, up-regulating VEGF expression by osteoblasts (Clarkin and Gerstenfeld, 2013). Hypoxia is associated with tissue acidosis and a reduced ambient pH activates osteoclasts and makes them grow in size and number (Arnett et al., 2003; Arnett, 2010; Dandajena et al., 2012; Al Hadi et al., 2013; Utting et al., 2010) increasing the resorption activity. In contrast, osteoblast growth, differentiation and, thus, bone formation are inhibited by hypoxia (Utting et al., 2006). Additionally, the discovery that hyperoxia has an osteogenic effect and decreases osteoclast formation and function (Al Hadi et al., 2013) reinforces the idea that a rich vascular supply is required to maintain bone formation activity and structural integrity.

Both aging and loss of sex steroids have adverse effects on skeletal homeostasis (Al Hadi et al., 2013). Sex steroids play a pivotal role in the skeleton acting in order to preserve bone mass. The major action of estrogen and testosterone at the tissue level is to reduce bone resorption (Bellido et al., 1995; Hughes et al., 1996; Manolagas, 2000). Moreover, it

is known that estrogen has a potent angiogenic effect (Losordo and Isner, 2001). Furthermore, evidence indicates that estrogen is a key regulator of VEGF production by osteoblasts and that ovariectomy decreases VEGF expression (Pufe et al., 2007) and bone vascularisation (Mekraldi et al., 2003). These results suggest that estrogen withdrawal and the progression of postmenopausal osteoporosis could influence VEGF production and blood supply to bone. However, the potential for targeting VEGF within the bone microenvironment to treating diseases is limited, primary because of our current knowledge of the complexity of VEGFs actions on bone cells, the lack of clarity surrounding its autocrine, paracrine functions, the bone cells which express functional receptors and if this functionality changes. Much of our understanding surrounding the effects of VEGF on bone cells is currently during bone growth and development, yet given the broad repertoire of VEGF receptor signalling reported by bone cells, it is likely that VEGF and its receptors continue to play vital roles coupling osteogenic and angiogenic processes in adult bone during remodelling and repair (Clarkin and Gerstenfeld, 2013).

Considerable progress has been made towards better understanding the role of the vasculature in the pathophysiology of bone. Clearly, this will remain a fruitful topic for research because of the strong links to common bone disorders (Marenzana and Arnett, 2013). Broadening our understanding of the basic physiological mechanisms linking vascular function to bone metabolism has the potential to unravel new pharmacological approaches to activate bone growth, accelerate fracture healing or build new vascular network in engineering tissues.

1.4 Bone tissue as a porous medium

Porous media are materials containing pores which are typically filled with a fluid and are most often characterised by their porosity. In the case of bone tissue, the anatomy of the bone porosity can be linked to the mechanical properties of the tissue (Schneider et al., 2013) and the bone fluid not only transports nutrients, waste products and mineral ions but also has been suggested to have a role in bone mechanosensory system (Cowin, 1999).

Poroelasticity is a theory that models the interaction of deformation and fluid flow in a fluid-saturated porous medium and can be applied to bone tissue. The deformation of the medium influences the flow of the fluid and vice versa (Cowin, 1999).

Particularly, cortical bone geometry and intracortical porosity are linked to bone stiffness, strength and fracture risk (Barth et al., 1992; Bell et al., 1999; Evans and Bang, 1967; Saha and Hayes, 1977; Schneider et al., 2013; Wachter et al., 2001). Cortical bone is perforated by an interconnected network of porous canals that comprises the living space of the vasculature and/or remodelling units that has been identified as the major contributor to local tissue porosity (Schneider et al., 2013). Osteocyte lacunae are the spaces in the mineralised matrix where the osteocyte cells reside and also contribute to bone porosity. Osteocyte lacunae may act as stress concentrators and play a crucial role in strain amplification necessary to trigger biochemical responses to loading as well as damage detection (Vaughan et al., 2013; Verbruggen et al., 2012). Figure 1.7 shows cortical bone porosity in murine bone associated to the canal network and the osteocyte lacunar system. A third source of bone porosity is the canalicular system that comprises the processes that connect osteocytes to each other and the bone surface. Figure 1.8 illustrates the lacunar and canalicular porosity in the cortex of a murine femur.

In addition to the canal network, lacunar and canalicular systems, microcracks are also present in bone as a result of fatigue. Fatigue is the gradual degradation of a mechanical component due to repeated, cyclic load loading. In medical circles, fatigue fractures of bones are better known as stress fractures and occur when bone damage (Taylor, 2000) and excessive bone remodelling are accumulated. It has been hypothesised that remodelling is the only mechanism by which fatigue damage can be removed from bone and it has been proposed that the fatigue life of a human tibia under normal loading may be less than three years if remodelling is not present to remove fatigue damage (Martin, 2003). Moreover, remodelling has been observed to be targeted at fatigue microdamage in the sense that it originates in response to, and in the immediate vicinity, of microcracks (Martin, 2003).

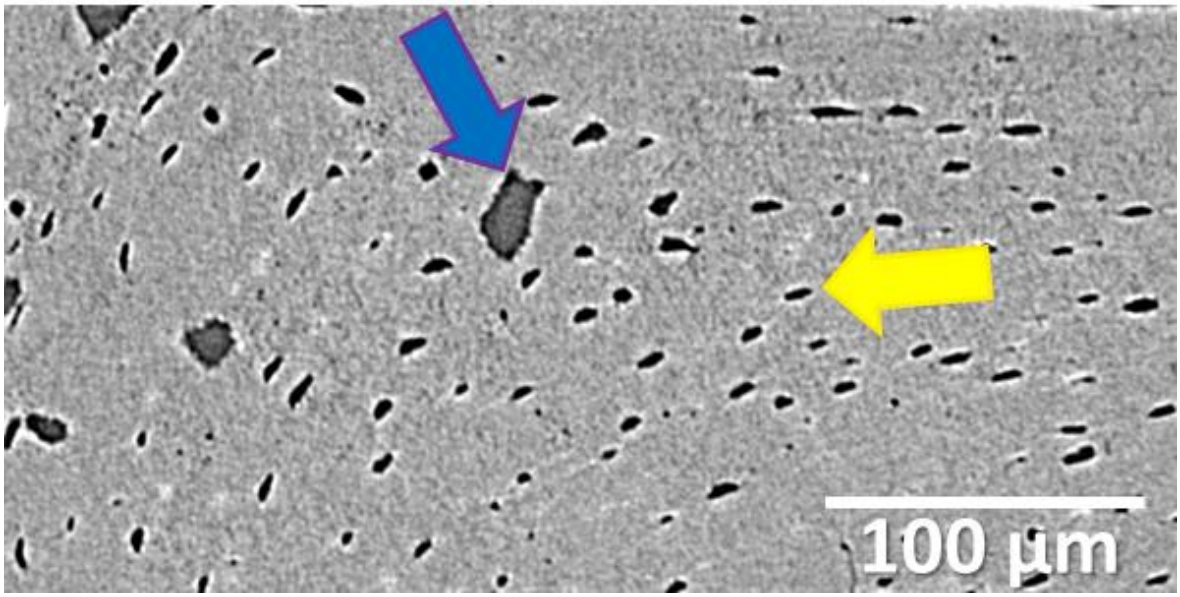

Figure 1.7. Reconstructed micro-Computed Tomography (µCT) raw data of the cortex of the murine tibiofibular junction. Data assessed at 650 nm nominal resolution. Yellow arrow indicates osteocyte lacunae and blue arrow cortical canal.

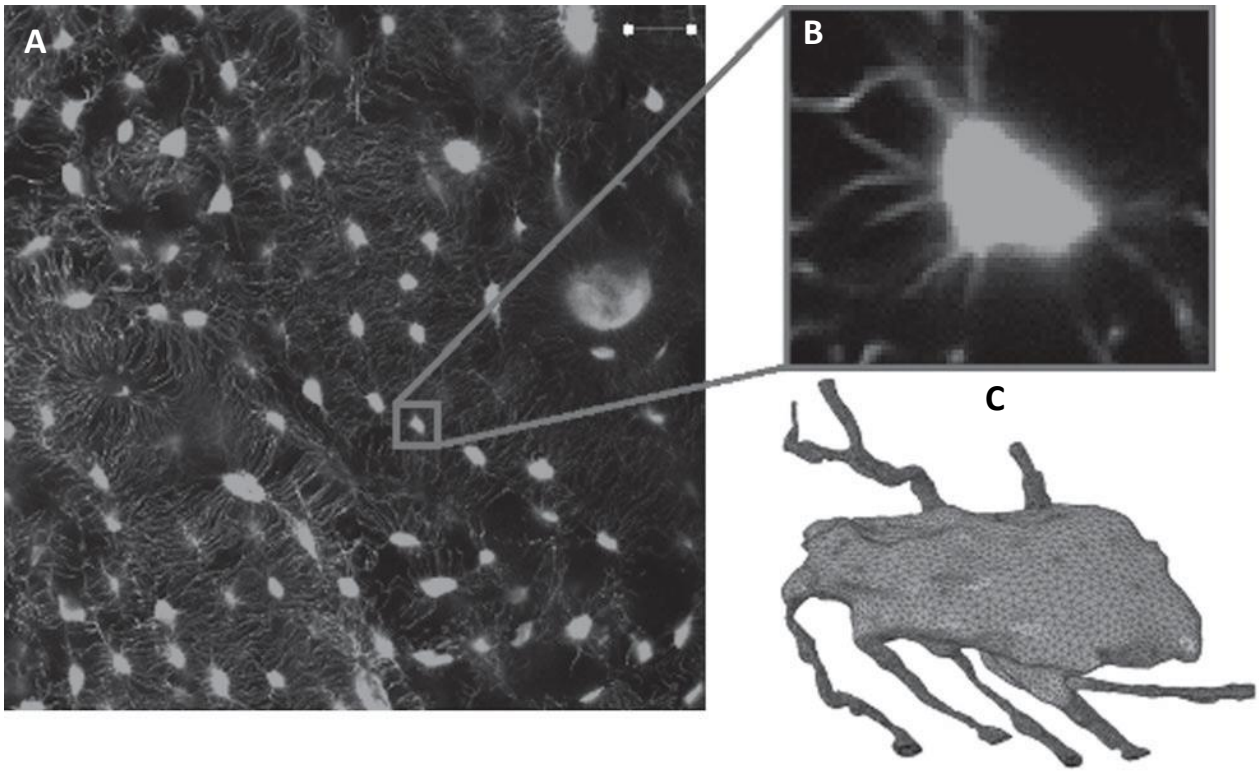

Figure 1.8. Lacuno-canalicular system in bone. (A) Confocal microscopy scan of the lacunar-canalicular network with (B) an individual osteocyte and (C) a finite element volume mesh of the osteocyte (Verbruggen et al., 2012).

Another important fact is that bone intracortical porosity has been shown to increase with age in humans (Cooper et al., 2007a; Zebaze and Seeman, 2015). Figure 1.9 illustrates cortical changes with age in women. Figure 1.9A shows an age-related increased in the intracortical porosity while Figure 1.9B shows an age-related thinning of the cortex. Although an increase in intracortical porosity compromises bone mechanical competence, it has not been investigated how these changes relate with bone vasculature that resides in the porosity network.

1.5 Visualising bone porosity utilising X-ray micro-computed tomography

For years, the study of porous media such as bone has been limited to destructive methods such as thin sectioning, and the imaging techniques relying on those methods were inherently 2D. Indeed, the 3D structural information was obtained by cutting the object into very thin slices, which were visualised in the light microscope, and then the 2D information was interpolated into a 3D structure model (Terribile and FitzPatrick, 1992). Stereology applied to histological sections has been the gold standard for the evaluation of bone tissue microarchitecture. The method consists of analysing 2D histological sections using conventional histomorphometry and has been widely used to extract 3D information of trabecular size and spacing, as well as porosity (Dempster et al., 2013). However, an accurate analysis of the original 3D bone structure cannot be made on the base of 2D information. In fact, this method is not only time-consuming but also rather unreliable since the bone structure itself can be altered by the preparation technique and the distance between slices is usually too coarse to avoid loss of 3D information. Additionally, due to the highly anisotropic organisation of bone, the evaluation of its 3D architecture based on 2D measures could lead to wrong conclusions (Matrecano, 2011). Thanks to the recent advances in technology it has been possible to switch to techniques that provide 3D images. When considering all the techniques, those based on X-rays are the most widespread since

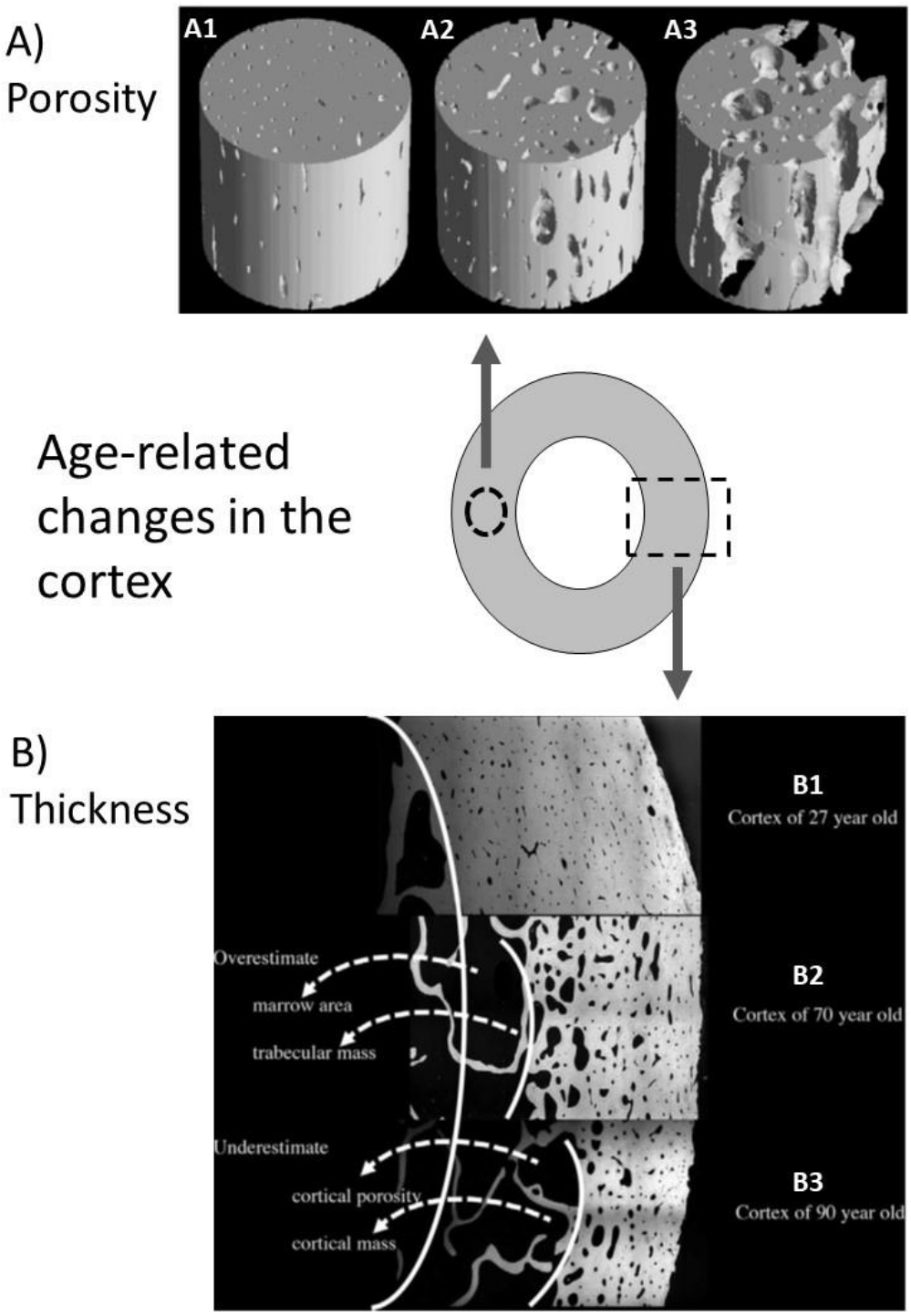

Figure 1.9. Age-relate changes in human cortical bone. (A) Age-related changes in cortical bone porosity. 3D rendering of micro-Computed Tomography (µCT) of cortical bone volumes: (A1) 20 year-old female, (A2) 61 year-old female, (A3) 87 year-old female [adapted from (Cooper et al., 2007a)]. (B) Age-related thinning of the cortex: (B1) 27 year old, (B2) 70 year old and (B3) 90 year old woman [adapted from (Zebaze and Seeman, 2015)].

they are non-destructive, fast and reach good resolutions. Computed Tomography (CT) offers several advantages. First of all, the sample is preserved so further analysis such as mechanical testing or histological sectioning can be conducted on the same tissue. Additionally, CT provides a digital data format as output, allows repeatability of measures and makes it possible to directly observe the changes that take place inside a material with no need of hypothesis on the media structure (Matrecano, 2011). Moreover, CT systems are highly developed and commercialised. In particular, the µCT systems can be considered as high-resolution version of the CT medical scanners. The division between conventional CT and µCT is an artificial distinction linked to the resolution. Typically, the spatial resolution of conventional medical CT scanners is in the range of 0.5 – 2.5 mm, which corresponds to voxels (volume elements) of 0.12 – 15 cubic mm. µCT gives the possibility to improve this spatial resolution by seven to eight orders of magnitude in terms of volume, depending on the application. Indeed, the actual resolution needed relates to the type and shape of the microstructural features of interest. They are being developed at a slower rate than the latter, because they are not used for clinical application, but are used above all in research.

The µCT systems began to grow in number in mid-to-late 1990s when common practice became to study human diseases by carrying out experiments on animals, and therefore their cost has decreased a lot. The development of CT devices in the medical field has been conditioned by the several constraints due to their use on patients. Firstly, the dose of X-rays received by the patient must be kept to a minimum, because of its toxicity. Second, the acquisition time can last only a few seconds, to prevent involuntary patient movements (e.g., breath, tremor, etc.) that could degrade the image quality. In general, these constraints do not apply for the imaging of inanimate objects, where the possibility of extending the exposure time, and then the dose, is used to improve the signal-to-noise ratio in the data. Nowadays, the µCT is widely used in many fields including electronics, biology, geology, materials science, food industry, oil and semiconductor industry, archaeology and biomedical engineering (Matrecano, 2011).

Most organs have already been analysed with µCT (Schambach et al., 2010). Furthermore, µCT has been used as a convenient technique to study trabecular and cortical bone architecture (Liu et al., 2010; Schneider et al., 2007; Thurner et al., 2010) and has been shown to be suitable to image the canal network and the bone cell network in 3D (Mader et al., 2013; Schneider et al., 2007) ex-vivo since submicron resolutions can be reached when there are no limitations to the amount of radiation that the sample can be exposed to and involuntary movement is not an issue. The situation is different using in vivo imaging and the resolution is usually limited to $\simeq 5$ micrometres in rodents which is insufficient to assess cortical porosity. In the case of humans and larger animals, High Resolution peripheral Quantitative Computed Tomography (HR-pQCT) can be used to assess bone microstructure including trabecular details and some cortical pores (resolution limited to 80 micrometres) (Lespessailles et al., 2017).

1.6 Challenges in the visualisation of the cortical bone vasculature

Our understanding of the physiological mechanisms regulating vascular behaviour in aged bone is challenging due to the inaccessibility of blood vessels, which are deeply encased within adult bone tissue. In particular the cortex or outer compact shell of most of our bones has an interconnected network of canals that comprises the living space of the vasculature (Schneider et al., 2013), namely vascular canals. Cortical bone accounts for 80% of the mass of bone (Burr, 2016) with significant contribution to bone strength, while being structurally more important than trabecular bone at most skeletal sites (Holzer et al., 2009; Mazess, 1990). Furthermore, loss of cortical rather than trabecular bone predominates in some types of fractures with cortical bone being the most important contributor to bone strength at many anatomical sites (Ferretti et al., 1995; Holzer et al., 2009; Mazess, 1990). Indeed, 70% of all age-related appendicular bone loss is cortical (Zebaze and Seeman, 2015). However, today it remains unclear whether alterations in the intracortical vasculature occur with age, if an abnormal intracortical vasculature accompanies skeletal diseases, if the vasculature can influence age-related bone loss and consequently to what extent preservation of the cortical vasculature could prevent bone fractures. Therefore,

imaging and characterisation of the bone vascular network *in situ* and hence in 3D is a promising approach to better understand bone health.

In the past, visualisation of the bone vasculature has been problematic due to the nature of the skeletal tissue itself and efforts have been focussed on inferring the 3D structure of the vascular network within bone. Histology has been a gold standard for years used in both clinical diagnosis and biomedical research. However, the technique requires special sample preparation including embedding, sectioning (most frequently preceded by decalcification) and staining and is also destructive and two-dimensional. Compared with histological examination, bone specimens can be evaluated in 3D and non-destructively using X-ray μCT; not requiring special sample preparation. Standard μCT or X-ray absorption-based μCT essentially maps the local X-ray attenuation of the specimen in 3D at a micrometre range. Although conventional absorption-based μCT is not sensitive enough to provide sufficient contrast for soft tissues, such as the vasculature, it has been used to provide spatial clues for the location of the blood vessels that reside within the intracortical canal network. The intracortical canal network can be extracted as a negative imprint of the calcified tissue from standard μCT images and several studies have done this in human (Cooper et al., 2003; Cooper et al., 2007a; Cooper et al., 2007b) and rodent bone (Britz et al., 2010; Britz et al., 2012; Schneider et al., 2007; Schneider et al., 2013; Thurner et al., 2010).

Bone cells can communicate with the vasculature (de Castro et al., 2015; Clarkin et al., 2008; Hu and Olsen, 2016a; Prasadam et al., 2014) in normal conditions and a loss in the quality of this communication could be involved in the onset of bone pathologies such as osteoporosis. Moreover, bone cell survival depends on the proximity to blood vessels (Ham, 1952) with osteocytes being the most abundant cells within the skeleton. Visualisation of the osteocytes has been problematic in the past due to the relatively small number cell density the mineralised nature of their extracellular matrix. In the last few years efforts have been focussed on detecting the non-mineralised spaces or lacunae where the osteocyte cells reside and large-scale analyses at the tissue level have been carried out to detect the osteocyte lacunae and quantify their morphology in 3D using μCT

(Dong et al., 2014; Mader et al., 2013; Palacio-Mancheno et al., 2014; Tommasini et al., 2012). The capabilities of standard µCT can be significantly extended when synchrotron radiation (SR) facilities are used as X-ray sources compared to lab-based X-ray sources, as higher spatial resolutions can be achieved at sufficient signal-to-noise ratios and scanning times to resolve intracortical microstructures within a few minutes, such as the intracortical network or osteocyte lacunae (Dong et al., 2014; Mader et al., 2013; Schneider et al., 2007; Schneider et al., 2013).

Investigations have been carried out in the past, perfusing the vascular circuit with a highly X-ray absorbing contrast agent to visualise the vasculature (Fei et al., 2010; Roche et al., 2012; Schneider et al., 2009). However there are some problems associated with these studies; specifically that differences in the rheology of the perfused agent and the blood fluid, it is very difficult to ensure that the agent has fully filled the vascular lumen (especially the smaller capillaries within the bone cortex), which results in disjoint vascular components and missing vascular segments as reported by Schneider et al (Schneider et al., 2009). Most frequently, the contrast agent perfusion is used in conjunction with decalcified bone (Fei et al., 2010; Roche et al., 2012) to allow image segmentation, which makes it impossible to assess the intracortical bone microstructure and the vascular morphology at the same time. Furthermore, when calcified samples are used, distinct segmentation of the vasculature and the mineralised tissue is problematic, not only because of the high X-ray absorption of the two components, but also due to the limited contrast between them.

1.7 The mouse as a model

Although humans and mice may look different, at a physiological and anatomical level they are remarkably similar. Mice have the same organs and organ systems which perform the same functions in the same way. The mouse genome is known, has been sequenced and we share approximately 95% of our DNA with mice and many genes responsible for complex diseases such as atherosclerosis or hypertension are shared between mice and

humans. Moreover, we can use knockout mice to work out what effect individual genes have in our body and recreate human genetic diseases. Additionally, mice have a rapid generation time and limited pathogenic risk. Although in comparison to humans, the skeletal mass of mice remains stable for a protracted period during their lifespan, mice can be ovariectomised to make them sex-hormone deficient, and to stimulate the accelerated loss of bone that occurs in women following menopause. In women, estrogen is known to be involved in the metabolism of both vascular bone tissues and estrogen withdrawal is associated with a rapid bone loss. Ovariectomy-induced bone loss in the mouse and postmenopausal bone loss share many similar characteristics and the ovariectomised mouse has been widely used as an animal model for postmenopausal bone loss (Jee and Yao, 2001; Kalu, 1991). However, a clear structural difference between the human and murine skeleton is that mice lack obvious osteonal or Haversian canals in cortical bone and secondary remodelling (Felder et al., 2017). In mice the function of the intracortical canals is therefore less clear. In relation to the vasculature, blood vessels run within Haversian canals in humans and, thus, mice seem to lack this longitudinal irrigation system within bone.

Hypothesis and aims

Evidence is today accumulating around the role the vasculature plays in contributing to age-related skeletal pathologies such as osteoporosis and thus targeting the vasculature to treat degenerative bone disease may provide a new therapeutic option for treatment of the disease.

The main objective of this PhD thesis is to use high resolution μCT imaging of cortical bone microstructure to test the research hypothesis that bone vascular networks will be altered with age and the following aims have been addressed:

Aim 1: Develop an image processing and analysis framework that allows for systematic measurement of the 3D architecture of vascular networks within cortical bone assessed by high resolution μCT ex-vivo. This aim was accomplished through the following specific steps:

Step 1.1: Detection of the mineralised tissue within the cortical bone

Step 1.2: Cortical porosity extraction

Step 1.3: Cortical porosity classification into vascular canals and osteocyte lacunae

Step 1.4: Computation of 3D spatial relationships between canals and lacunae

Step 1.5: Selection of an appropriate skeletal site in the murine skeleton where the effect of age in the intracortical vascular network can be evaluated.

Aim 2: Apply the developed methodology to assess age-related changes on vascular canal networks within cortical bone in female mice.

Step 2.1: 3D characterisation of the intracortical vascular networks within the young-adult murine tibiofibular junction

Step 2.2: Assessment of changes in the intracortical vascular networks with age.

Aim 3: Extend the use of the developed methodology to assess cortical microstructure in a transgenic mouse (female) where VEGF was deleted specifically from osteoblasts.

Step 3.1: Extract cortical porosity for transgenic animals where VEGF was specifically deleted from osteoblasts and WT controls

Step 3.2: Assess changes in the intracortical microstructure due to the lack of VEGF.

Aim 4: Apply phase contrast-enhanced X-ray tomography imaging to visualise soft tissue within cortical bone.

Step 4.1: Exploit the high degree of coherence of third generation synchrotron light sources to enhance imaging contrast and visualise the 3D structure the soft tissue comprising the intracortical bone vasculature (with no prior sample preparation).

Step 4.2: Demonstrate that the intracortical microstructure can be assessed simultaneously along with the vasculature using the same imaging set-up.

Chapter 2: Principles of X-ray tomography imaging and image processing

2.1 Introduction

X-ray µCT imaging was used to access cortical bone microstructure within this PhD thesis. The cortical bone CT images were then processed and analysed to detect the mineralised tissue, extract porosity, classify porosity into vascular canals and osteocyte lacunae and compute 3D distances between canals and lacunae. This chapter summarises the principles behind X-ray tomography imaging and the processing and analysis of the images. These tools will be combined in Chapter 3 to develop a methodology for the extraction and quantification of the bone features and achieve the aims of the PhD project.

2.2 µCT imaging

2.2.1 CT Fundamentals

X-ray CT is based on the attenuation of X-radiation through a material. 2D radiographic images or projections are taken around a single axis of rotation. The physical principles behind CT is modelled by the Lambert-Beer's law. Through a homogeneous object, an incident radiation of wavelength λ suffers an attenuation given by the following equation:

$$I = I_0 e^{-\mu x} \quad (2.1)$$

where I_0 is the intensity of the incident radiation, and I is the beam's intensity after it traverses a material of thickness x characterized by a linear attenuation coefficient μ (cm^{-1}). The attenuation coefficient μ it is a strong function of the effective material atomic number Z, as well as the photon energy of the x-ray beam. The absorption mechanism results from the interaction between two effects: photoelectric absorption and the Compton scattering. For low X-ray energies, photoelectric absorption is predominant, instead for higher energies, the Compton scattering is more prevalent. Further details can be found in specialised texts (Hsieh, 2009).

Equation (2.1) can be written in its differential form to shift the focus on what occurs within each small thickness element dx:

$$\frac{dI}{I} = -\mu dx \quad (2.2)$$

Let s be a path along an object, the more general form can be obtained:

$$I = I_0 e^{-\int \mu(s) ds} \quad (2.3)$$

where $\mu(s)$ is the linear absorption coefficient at the position s along the ray. We can rewrite the equation (2.3) as:

$$\int \mu(s) ds = ln \frac{I_0}{I} = p_\vartheta(s) \quad (2.4)$$

where ϑ is the orientation of the x-rays. The central problem of computed tomography is to assign the correct value of μ to each position in the material based only on the knowledge of the line integrals for the various orientations and positions.

Locating and defining the different contributions to attenuation requires measuring $\frac{I_0}{I}$ for many different ray directions ϑ, and many different positions for a given ϑ. The sum of attenuation values at each position along the profile at ϑ angle, is called Radon Transform or projection, $P_\vartheta(s)$. The set of projections, collected at enough well-chosen directions ϑ, is called a sinogram.

A 3D image of the inside of the sample is generated from the projections in a digital process known as reconstruction. The filtered back-projection algorithm is widely used for tomographic reconstruction. As the name suggests, the filtered back-projection algorithm consists of two distinct phases: filtration and back-projection. Generally, the reconstruction is carried out in polar coordinates and the map of $\mu(x, y)$ is obtained going through the following steps:

1. Computing the Fourier transform $F_\vartheta(u, v)$ of measured projection P_ϑ for each angle ϑ;
2. Multiplying $F_\vartheta(u, v)$ by the weighting function (the transform of the filter) to obtain $F'_\vartheta(u, v)$;
3. Computing the inverse Fourier transform of $F'_\vartheta(u, v)$ and summing over the image plane (direct space or spatial domain), which is the back-projection process.

The raw data obtained in this way by the reconstruction algorithm do not correspond yet to an image but rather to a matrix holding the absorption values in the reconstructed cross sections. After reconstruction, the raw data cross sections are converted into a grey scale image (Matrecano, 2011).

2.2.2 µCT desktop scanners and synchrotron facilities

A µCT desktop scanner available in the facilities of the Faculty of Engineering and the Environment and applying for beamtime in a synchrotron facility were the two options to image bone using X-ray tomography at the beginning of this PhD project. µCT desktop systems incorporate a X-ray tube to generate X-radiation. In the tube, electrons emitted from the cathode are accelerated by an electric potential difference to collide with a heavy metal anode (generally a metal such as Cu, Mo, Ag, or W). Upon striking the target, the electrons are decelerated to produce radiation. Only a very small fraction of the energy of the electron beam is converted to X-radiation; most of the energy is instead released as heat (Matrecano, 2011). Figure 2.1 shows the ZEISS Xradia Versa desktop scanner available in the facilities of the µ-VIS centre for computed tomography at University of Southampton. Magnification in this type of X-ray microscope is achieved by using projection geometry with a point source and optical systems, similar to a regular visible light microscope. Figure 2.2 shows the internal view of this desktop scanner and its principal elements.

Figure 2.1. ZEISS Xradia Vers external view.

Synchrotron technology uses highly energetic electrons moving in a large circle as a source of X-radiation. Figure 2.3 illustrates the elements within synchrotron systems. Electrons are firstly accelerated in the linear accelerator and then deflected through electromagnetic field in the storage ring to create radiation. This radiation is then used in experimental stations located on different beamlines. Synchrotron technology offers some advantages over desktop systems. These advantages are due to the different radiation that the two systems generate. The radiation generated in the X-ray tubes of a desktop system is polychromatic. The absorption coefficient μ depends on the energy of the X-ray photons and this dependency is not considered in the reconstruction process which induces a non-linear error in the recorded data. Synchrotron radiation is monochromatic and of a very high intensity which translates into better quality images and faster acquisitions.

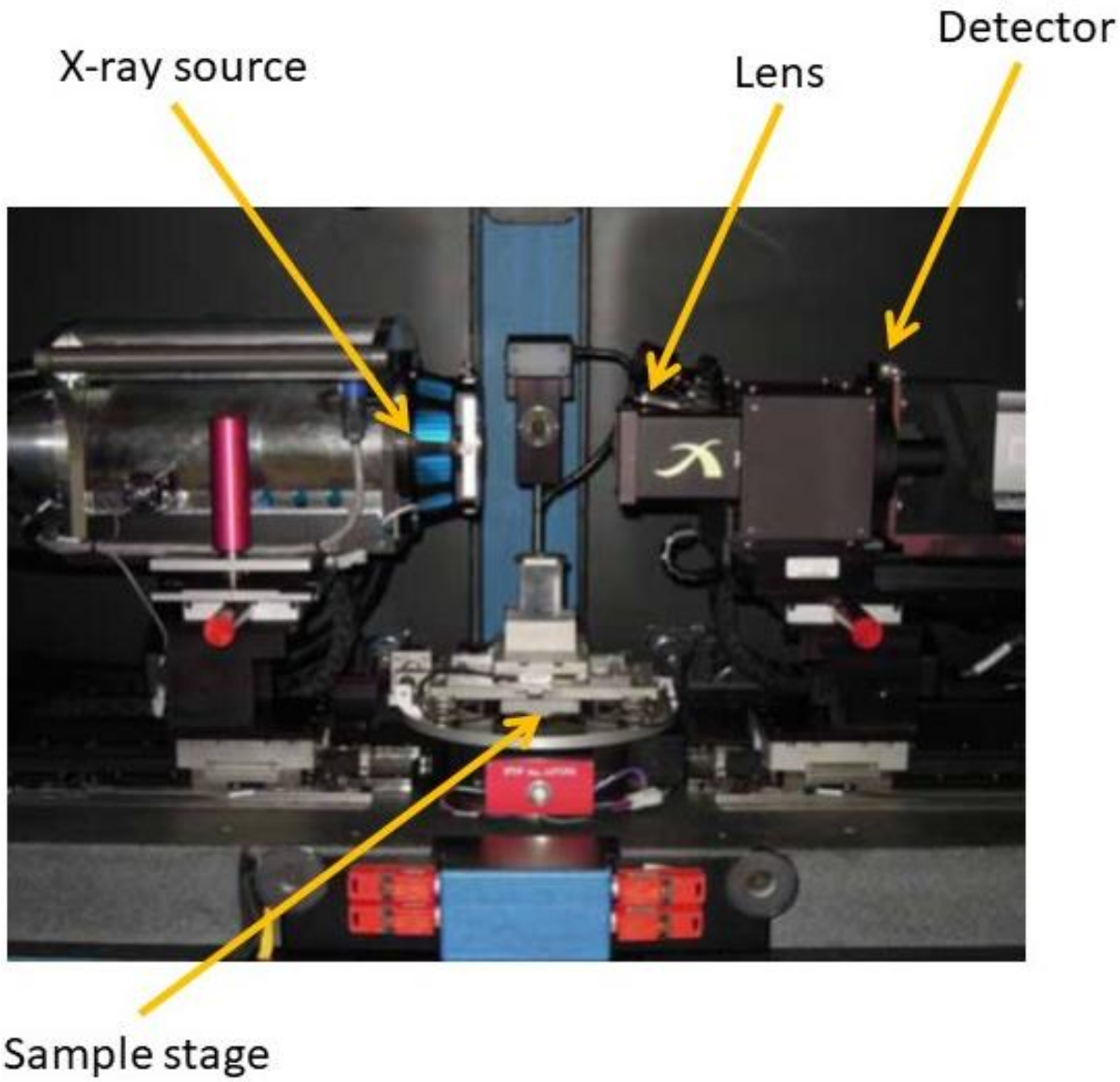

Figure 2.2. ZEISS Xradia Versa internal view and principal elements. In this type of X-ray microscope magnification is achieved by using projection geometry and optical systems.

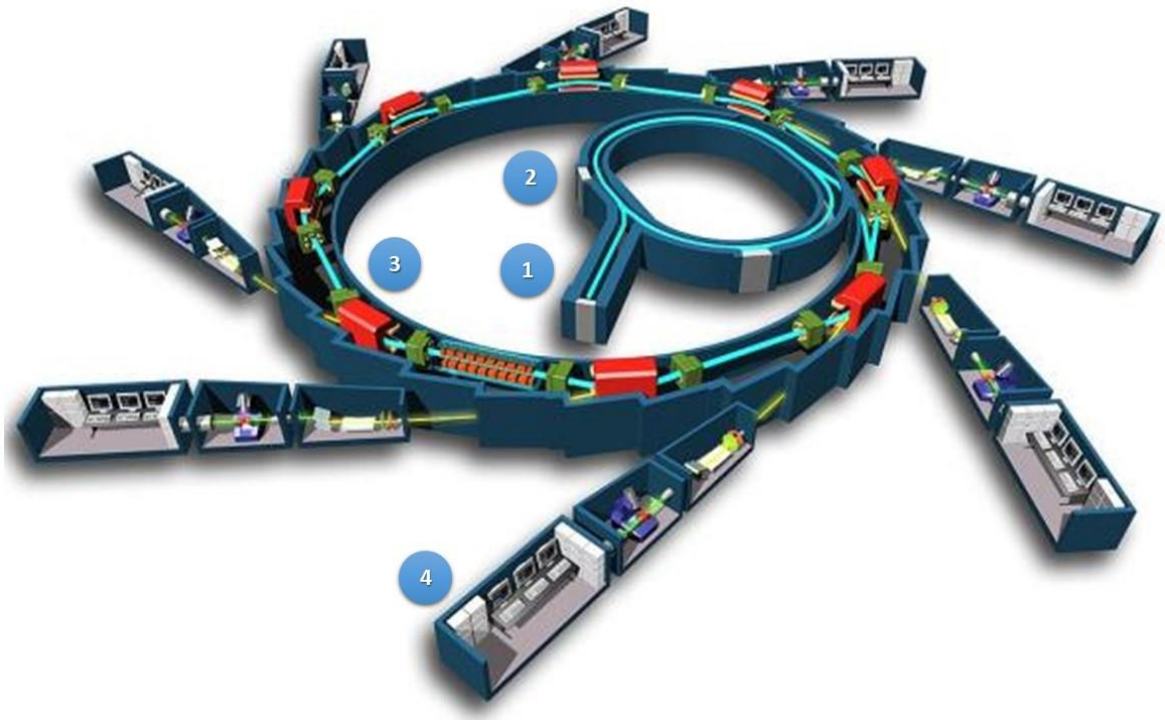

Figure 2.3. Synchrotron technology. Electrons are generated (1), accelerated (2), deflected through electromagnetic field in the storage ring (3) to create extremely bright light. Light is channelled down beamlines to workstations (4) where it is used to scan the samples.

2.3 Image processing and feature extraction

2.3.1 Greyscale digital images

CT data are greyscale images. A 2D digital image consists in a grid of picture elements, known as pixels. In a grey scale image each pixel is associated with a numerical value that represents the intensity (shade of grey). Figure 2.4 illustrates this concept. Digital images can be processed to extract features, identify and separate different objects within them and quantify distances, areas and shapes.

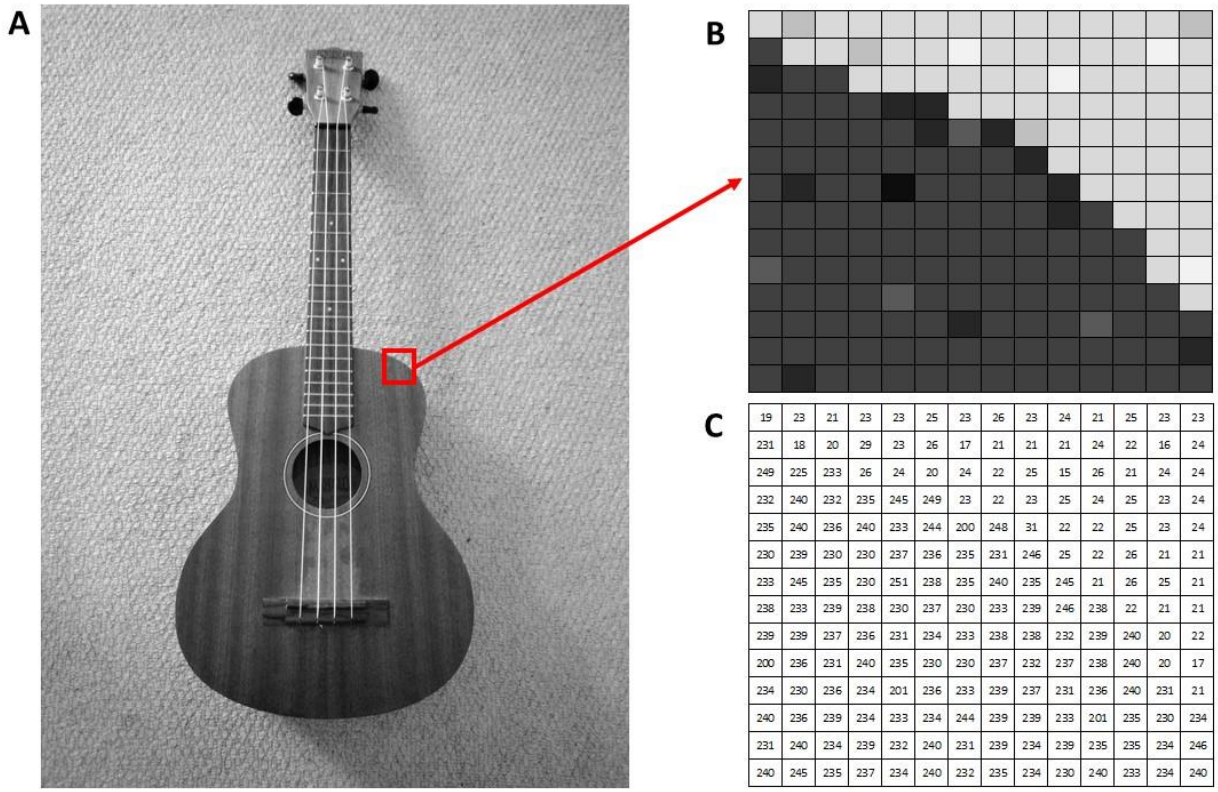

Figure 2.4. Grayscale image of a ukulele (A). Pixels within the magnified region of the image (B) and their numerical representation to encode intensity (C).

2.3.2 Thresholding

Thresholding is one of simplest methods for image segmentation. It is used to divide the image into segments or regions, known as object and background. The result of this image operation is a binary image that consists in pixels with only two possible values: black and white (or ones and zeros, or object of interest and background). The global thresholding methods uses a single fixed constant value as threshold for the classification of the pixels within the image. If the numeric value of a particular pixel is greater that the threshold, that pixel is classified as object (or black) and if the intensity of the pixel is less that the fixed constant the pixel is part of the background (or white). Figure 2.5 illustrates this concept.

The histogram of a digital image is a graphical representation of the intensity distribution within an image. Figure 2.6 shows the histogram of the image in Figure 2.5A. Histograms of images with clear object and background have a bimodal histogram which means that two peaks can be identified in the histogram.

Global thresholding and the histogram of the image will be used to detect the mineralised tissue within the CT images as it will be explained in Chapter 3.

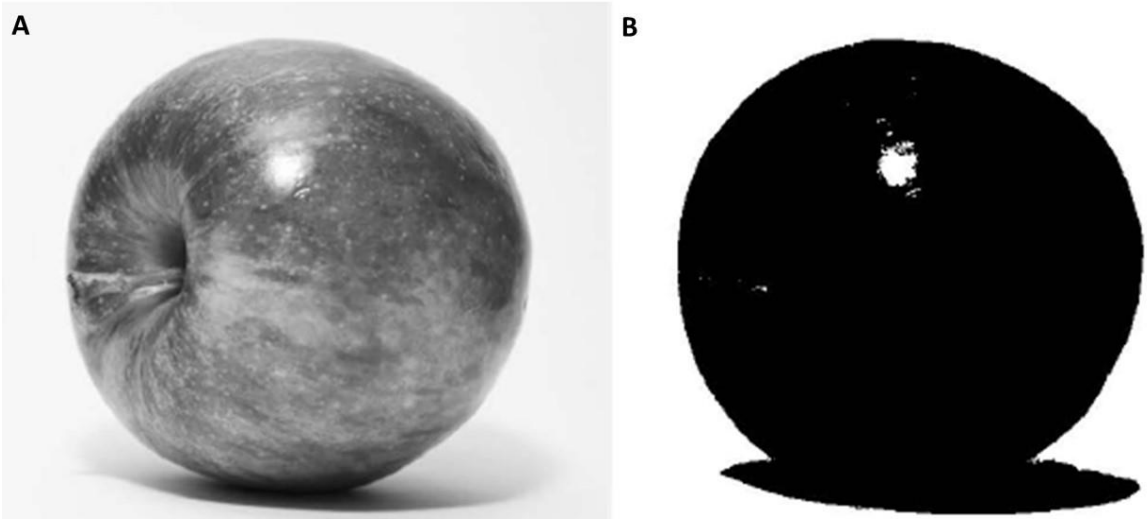

Figure 2.5. Global Thresholding. Grayscale image of an apple (A). Object and background in black and white colours respectively for thresholded image (B).

2.3.3 Morphological operations

Morphological operations are a collection of transformations related to the shape or morphology of the features in an image. In the particular case of a binary image, these transformations derived from mathematical morphology are used to remove small spots, fill holes, extract boundaries, separate and merge objects. Morphological operations will be used to extract cortical bone porosity from the CT images as it will be explained in Chapter 3.

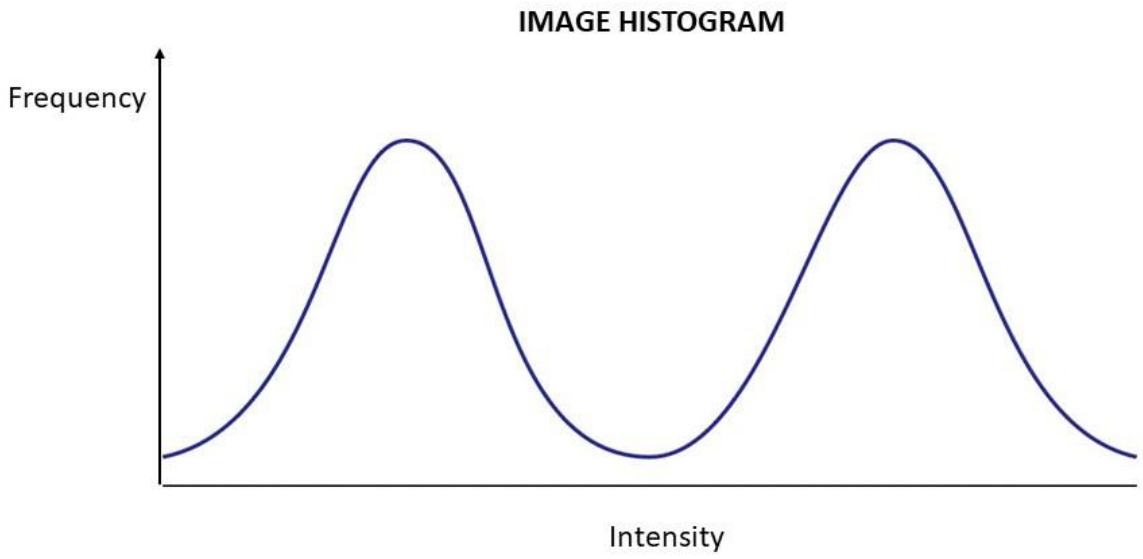

Figure 2.6. Image histogram with two peaks corresponding to the two segments in the image 2.5A.

Erosion is one of the two basic morphological operations. The basic effect of the operator on a binary image is to erode away the boundaries of regions of foreground (object) pixels. Thus, areas of foreground pixels shrink in size, and holes within those areas become larger. Dilation produces the opposite effect, enlarging the boundaries of regions of foreground pixels. Thus, areas of foreground pixels grow in size while holes within those regions become smaller. Figure 2.7 illustrates the effect of erosion and dilation.

Opening is a combination of the two basic operations: an erosion followed by a dilation. Closing is the opposite process consisting in a dilation operation followed by an erosion. Opening can be used to separate objects and remove small spots while closing is useful to merge objects and fill small holes. Figure 2.8 shows the effects of opening and closing on simple digital images.

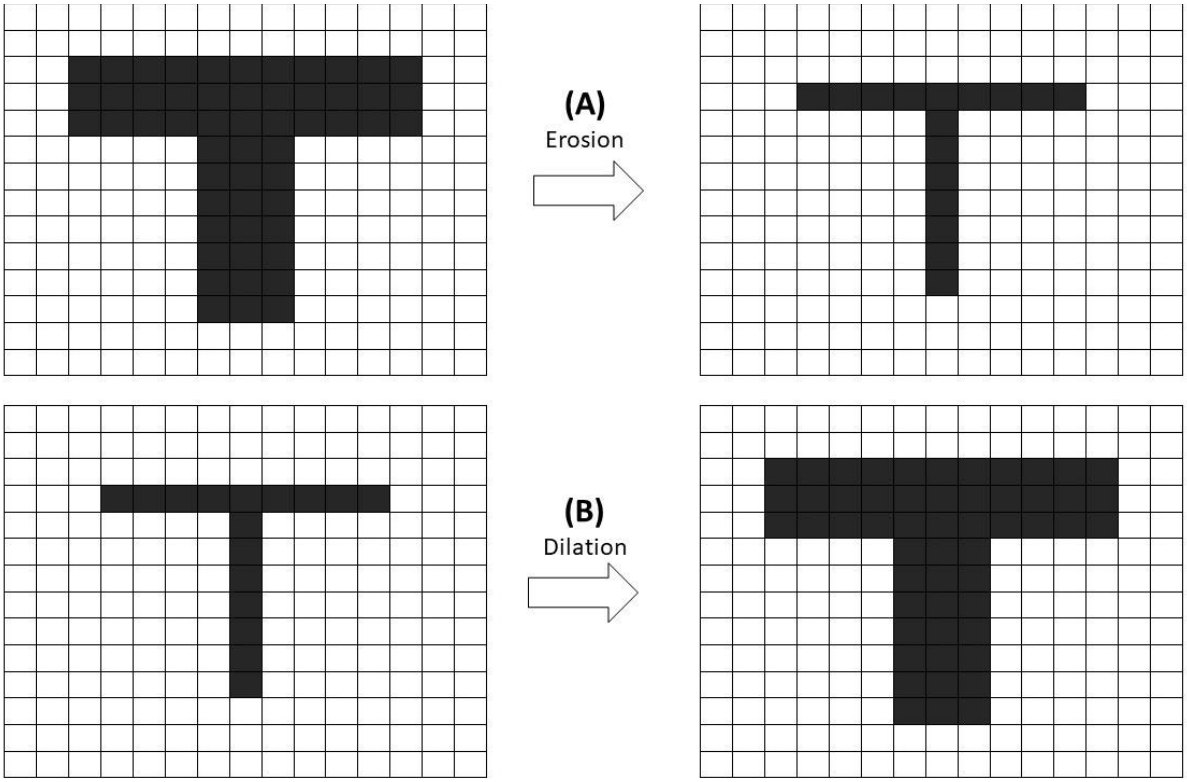

Figure 2.7. Basic morphological operations. Erosion (A) shrinks the foreground object while dilation (B) enlarges it.

2.3.4 Labelling

Connected-component labelling or simply labelling is an operation that scan a binary image and groups its pixels into components based on their connectivity. Pixels that are connected to each other are part of the same group and are labelled or tagged with the same identity number. Figure 2.9 helps to explain this operation. As it will be discussed in Chapter 3, labelling will be used to identify individual vascular structures and osteocyte lacunae within the cortical bone and provide them with an identity number, which is a prerequisite for quantification of these objects and other derived measurements.

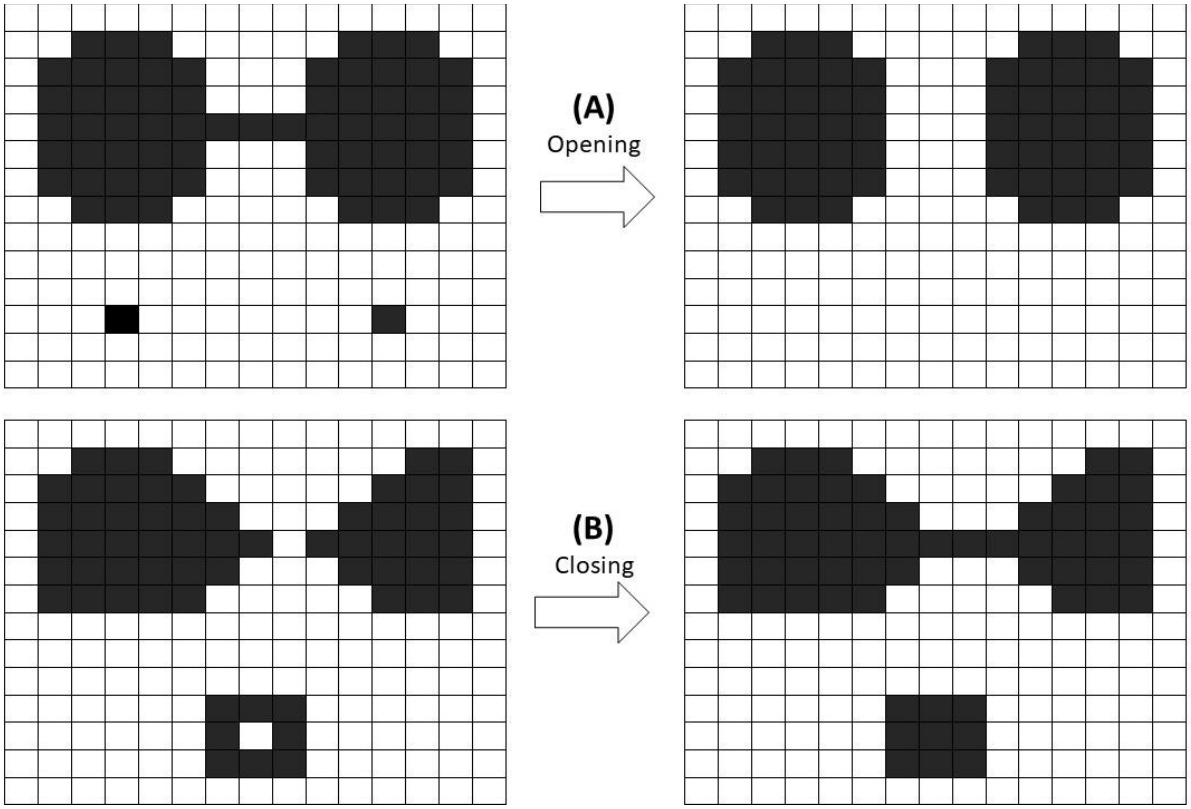

Figure 2.8. Combined morphological operations. Opening (A) can be used to separated objects and remove small spots while closing (B) can be used to merge objects and fill small holes.

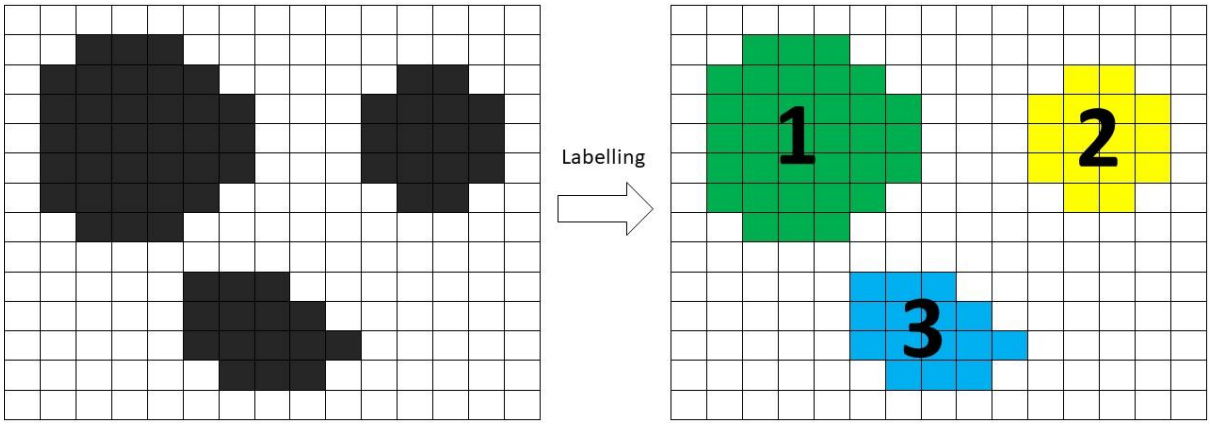

Figure 2.9. Labelling operation groups connected pixels and provide them with group identity number.

2.3.5 Sieve analysis

Sieving is the process of extracting a subset of objects from a binary image, after they have been labelled, based on one of their properties such as size. Sieving will be useful to separate vascular canal objects from osteocyte lacunae as it will be explained in Chapter 3.

2.3.6 "AND" and "INV" logical operations

Logical operators are derived from Boolean algebra, which is a way to manipulate binary values. Only "AND" and "INV" operations will be discussed here since they are the only two logical operations that will be used in Chapter 3. There are other logical operations such as OR, NOR and NAND not name a few. The "AND" operation combine two binary images to produce a third binary image whose objects are the intersection of the objects in the combined images. The two input images need to have the same dimensions. Figure 2.10 helps to explain this concept. "INV" operation generates the inverted image of a given binary image, which means that it transforms the object into the background and the background into the object (black pixels become white and white pixels become black). Figure 2.11 shows the "INV" image of an example binary image.

2.3.7 Arithmetical operations

Arithmetical operations are also possible on images. Addition, subtraction, multiplication and division can be performed combining an image and a factor or more than one image. The arithmetic operations are carried out at the pixel level and in the case of combining images these need to have the same number of pixels and dimensions. Arithmetical operations will be helpful to quantify spatial relationships between the porosity objects of the CT images as it will be shown in Chapter 3.

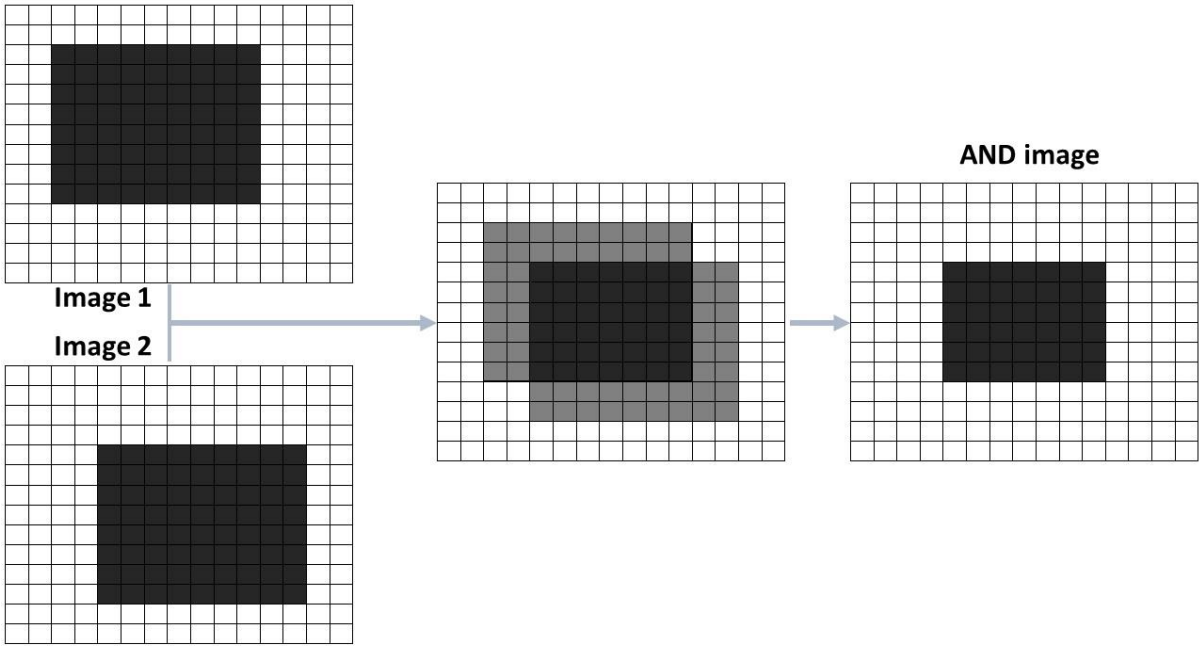

Figure 2.10. “AND” operation combines two binary images to generate a third binary image whose objects are the intersection of the objects in the input images.

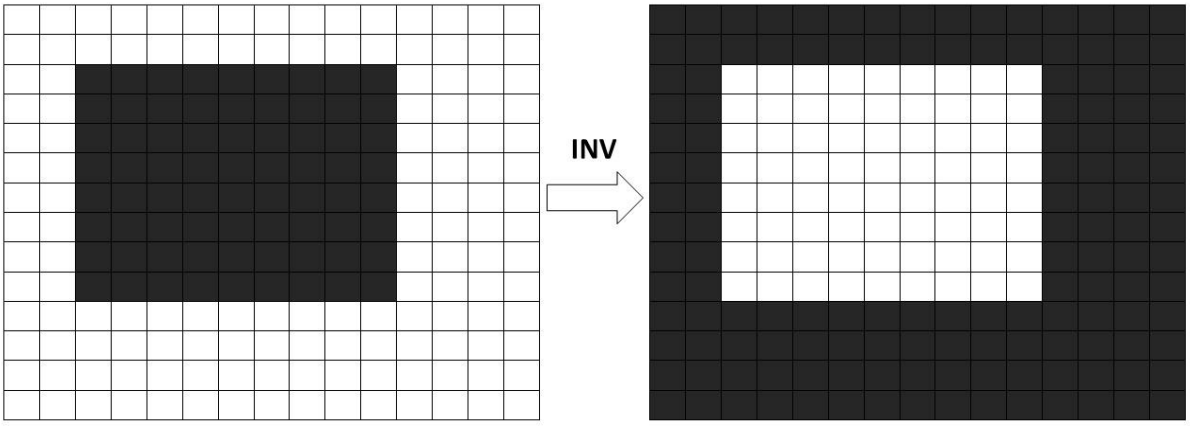

Figure 2.11. “INV” operation changes white pixels to back and black pixels to white to generated an inverted image of the original binary input.

2.3.8 Distance transform

The distance transform (also known as distance map) is an operator that computes distance to the closer boundary for every pixel in the foreground of a binary image. This operation provides an indication for depth. Figure 2.12 illustrate the concept. The distance maps will be used in Chapter 3 to compute distances between vascular structures and osteocyte lacunae which will provide an indicator for bone tissue vascularisation.

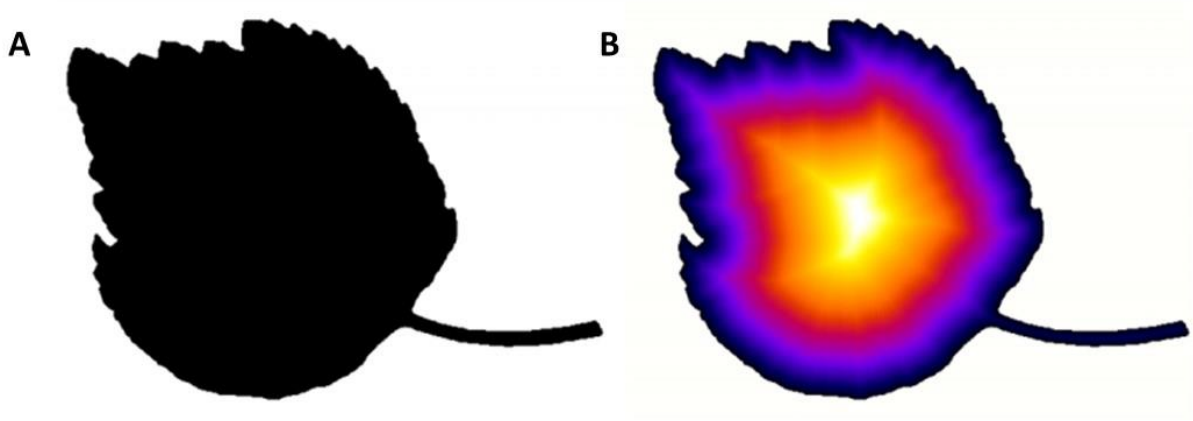

Figure 2.12. Distance transform. Binary image (A) and its distance transform (B). Distance map shows proximity to the boindary for every pixel within the object.

2.3.9 3D images vs 2D images

The output of a CT scan is a 3D image. A 3D image is composed by a stack of 2D images. A 3D image consists in a 3D grid of volume elements or voxels which are an extension of the 2D pixel in the third dimension. The height of the voxel is controlled by the spacing between the 2D images in the stack. Figure 2.13 helps to explain these concepts. All the introduced image operations for 2D images are also applicable to 3D images.

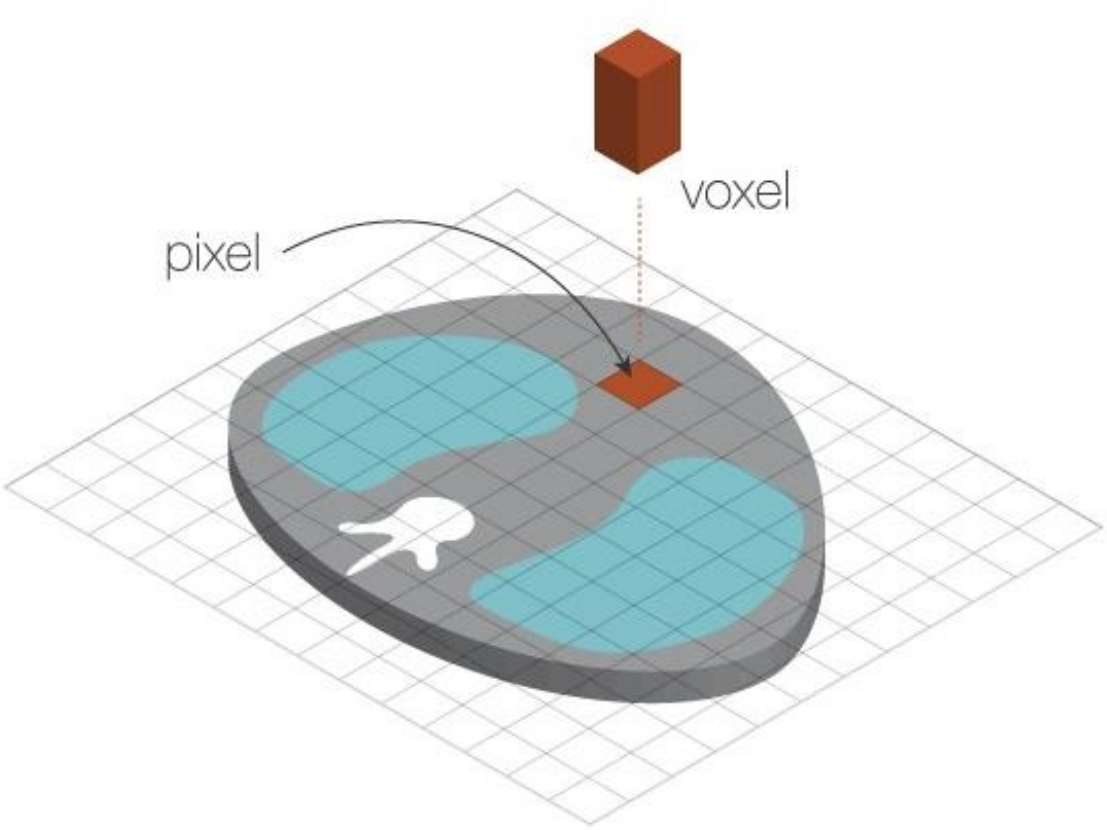

Figure 2.13. Relationships between pixel and voxel. Voxel is a pixel with a third dimension, the depth. The depth is controlled by the spacing of the 2D images in the stack.

Chapter 3: Results I – Development of a methodology for the extraction, classification and quantification of cortical bone features

3.1 Introduction

The approach presented in this thesis for the study of cortical bone vascularisation required 1) the detection of the mineralised tissue comprising the cortical bone at a sufficient spatial resolution to visualise microstructure and porosity 2) the extraction of cortical bone porosity, 3) classification of vascular canals and osteocyte lacunae and 4) the evaluation of 3D spatial relationships between canals and lacunae. This chapter focuses on the development of an imaging and analysis framework that allowed the quantification of the distribution of vascular canals and osteocyte lacunae in the murine cortical bone. It stablishes the resolution for the X-ray μCT imaging and the image operations to be carried out for feature extraction and quantification. The chapter finishes with the selection of a site in the murine skeleton where the effect of the vasculature can be further investigated.

3.2 Methodology

3.2.1 The effect of X-ray μCT imaging resolution in porosity detection and extraction

The spatial resolution is a crucial parameter in an imaging system. It defines the smallest structural details that can be captured and its determination is linked to the problem under consideration. Characterisation of the pores and cavities within the mineralised tissue depends on the spatial resolution. The voxel size influences the partial volume effect, which is defined as the loss of small details because of the limited resolution of the imaging system. The partial volume effect occurs when an object partially occupies the sensitive volume of the imaging instrument. However, defining the adequate image resolution is not a trivial aspect and understanding the correlation between scan parameters like voxel size and the structural properties is crucial for comprehensive bone characterisation using μCT. Therefore, an initial investigation was carried out to evaluate the influence of the spatial image resolution on the detection of bone porosity using two voxel sizes: 1.7 and 0.85 μm (ZEISS Xradia Versa desktop scanner; voltage = 80 kV, power =

7 W; tibia of 15 weeks C57BL6 female mouse). Figure 3.1 shows the two reconstructed cross-sectional images at the two different resolutions.

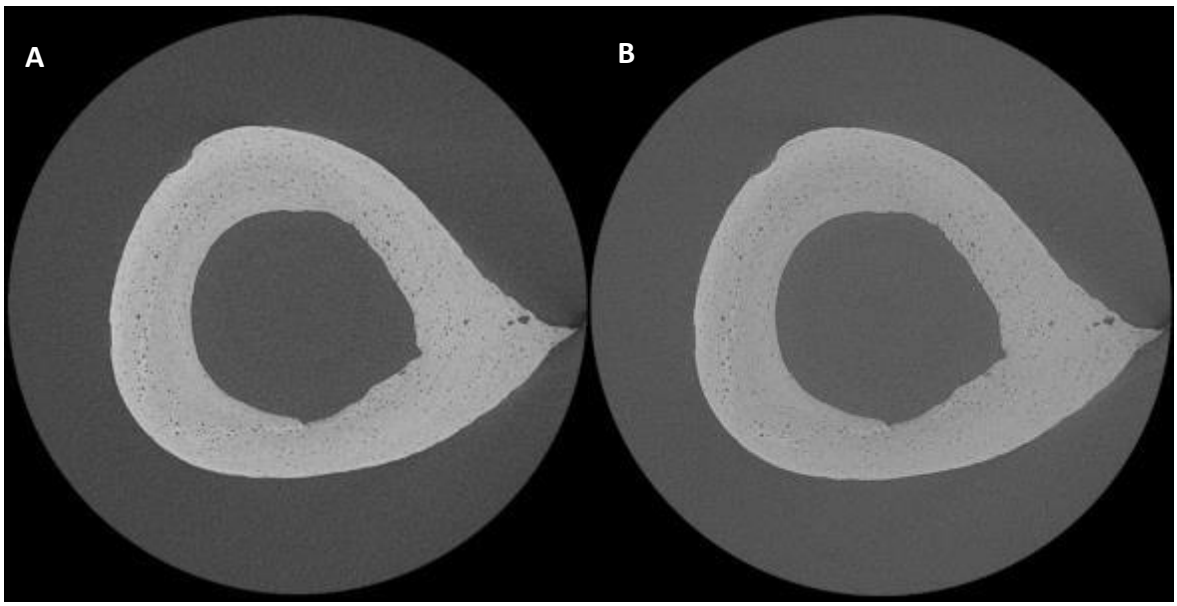

Figure 3.1. Reconstructed slices from a tibia of a 15 week old C57BL6 female mouse. Data assessed at 1.7 µm (A) and 0.85 µm (B) voxel sizes.

Figure 3.2 shows the histograms of the images in Figure 3.1. The two peaks associated to the distributions of background and mineralised pixels are better defined for the dataset with lower resolution. Figure 3.3 shows the binarised images after global thresholding (using the midpoint between the two peaks as threshold) of the datasets shown in Figure 3.1, with cortical porosity evident for both resolutions.

Figure 3.4 shows the 3D rendering of the porosity objects for the same small region of interest at the two different resolutions. The dataset with higher resolution performed better at capturing the shape and volume of the objects. However, very small particles consisting in few voxels are presents in the high resolution dataset. These particles were noise and not osteocytes lacunae and must be removed before the porosity analysis. On the other hand, the volume and shape of the particles is underestimated on the dataset with lower resolution.

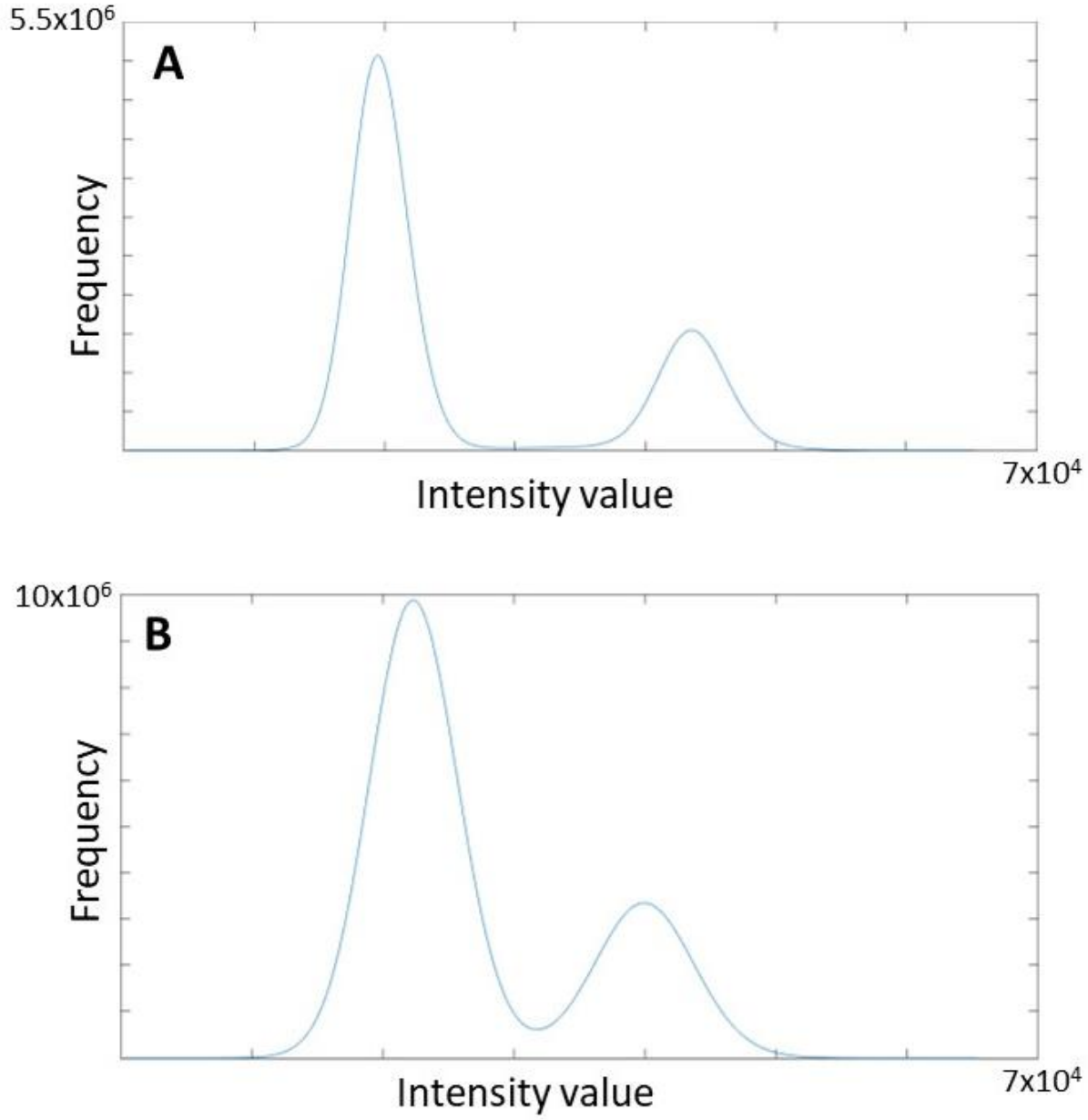

Figure 3.2. Histograms of the slices in Figure 3.1. Data assessed at 1.7 µm (A) and 0.85 µm (B) voxel sizes.

Figure 3.5 shows a very small and random picked region of 767625.625 μm^3 where 8 osteocyte lacunae were identified at both resolutions. Although the shape and volume of lacunae are more accurate at higher resolution, the low resolution image can be used to

locate lacunae within the mineralised tissue since the number of objects and their positions were validated visually and none of the osteocytes detected in the high resolution image was missed (with the small spots present at higher resolution identified as errors).

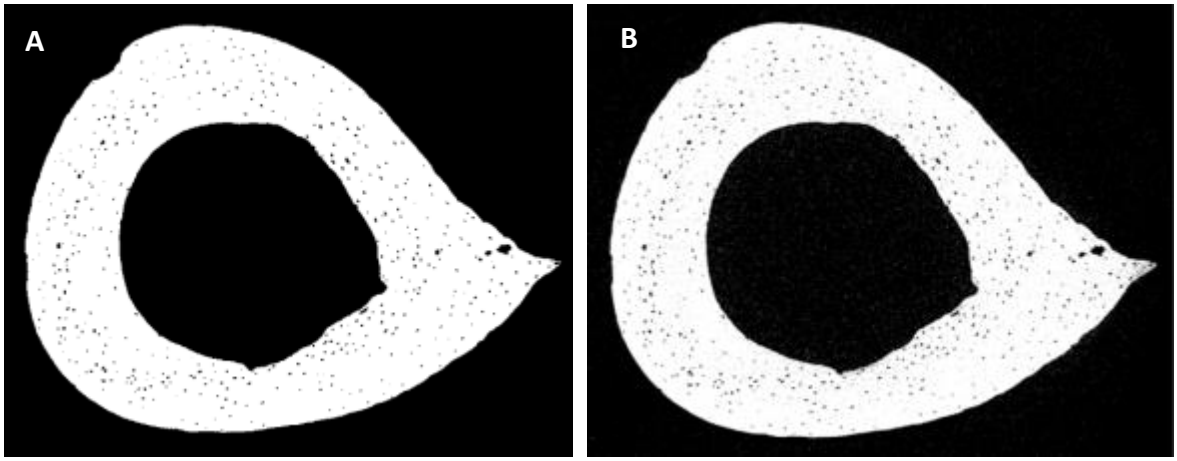

Figure 3.3. Binarised images as a result of the application of the global thresholding to the datasets in Figure 3.1. Data assessed at 1.7 µm (A) and 0.85 µm (B) voxel sizes.

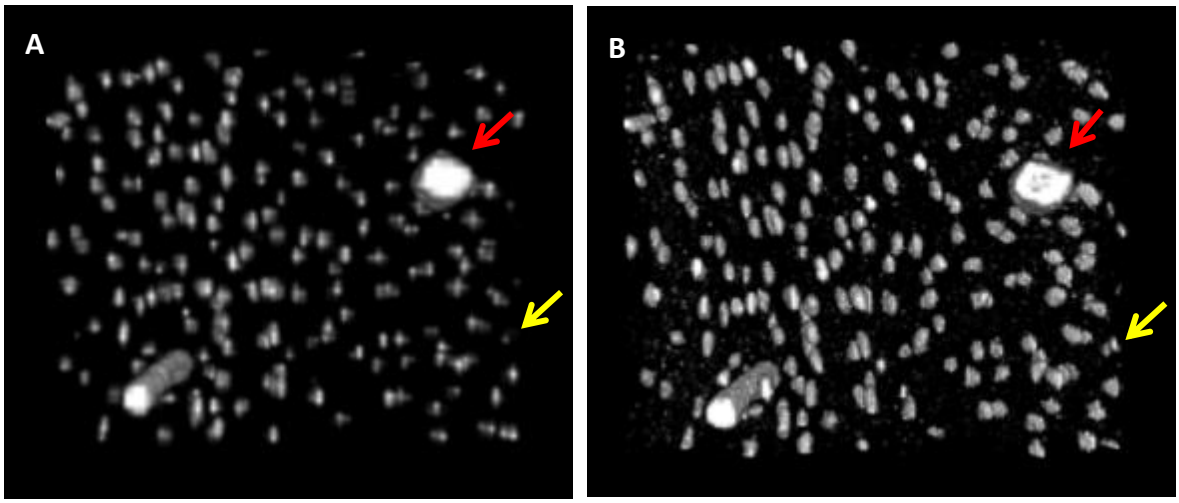

Figure 3.4. 3D rendering of the porosity objects in a small region of the datasets shown in Figure 3.1. Data assessed at 1.7 µm (A) and 0.85 µm (B) voxel sizes. Red arrow pointing to vascular canals and yellow arrow pointing at osteocyte lacunae.

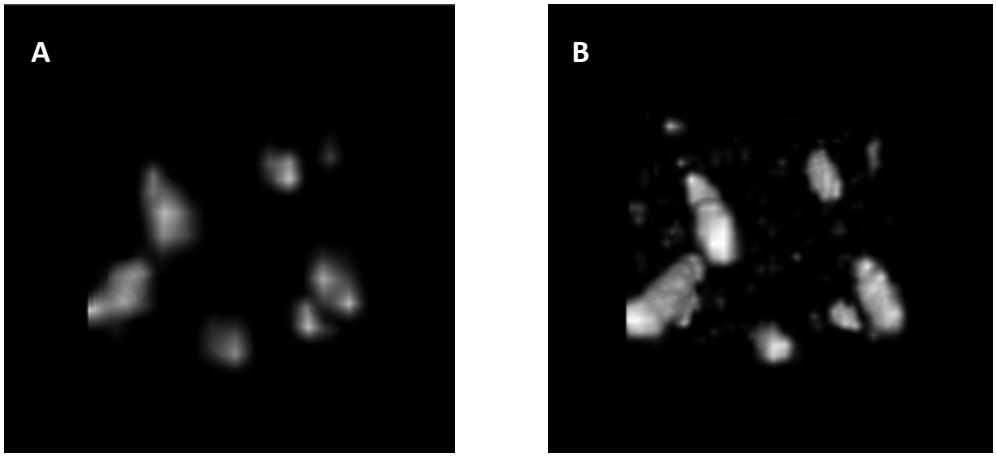

Figure 3.5. 3D rendering of the porosity objects in a very small region (76765.625 μm^3) of the datasets shown in Figure 3.1. Data assessed at 1.7 µm (A) and 0.85 µm (B) voxel sizes.

Additionally, 5 larger regions of 4913000 μm^3 where randomly selected for a more exhaustive analysis and the porosity objects labelled and counted using Avizo software for 3D image processing. The results are shown in Table 3.1 for the counting of porosity objects within the 5 regions at the two different resolutions. Differences in the counting measure detection errors.

3.2.2 Image processing operations for porosity extraction and classification

Once the effect of the resolution was explored and it was clear that the presence of vascular canals and osteocyte lacunae can be detected even at the lowest of the two proposed resolutions, the type and order of the image operations to perform on the CT images to extract porosity features and separate them into canals and lacunae needed to be defined. Figure 3.6 summarises the steps in the processing of the images.

	Dataset A (1.7 µm)	**Dataset B (0.85 µm)**	**Difference (%)**
Region 1	290	290	0
Region 2	254	255	0.39
Region 3	238	240	0.83
Region 4	227	230	1.30
Region 5	260	263	1.14

Table 3.1. Counting of porosity objects in 5 randomly selected regions to assess errors in the detection of lacunae.

The first step in the extraction and classification of the cortical porosity was the binarisation of the CT images. CT readouts consist in a stack of grayscale 2D images. To generate the binary image and segment the mineralised tissue from air, liquid and soft tissue; a global thresholding operation was applied. The intensity values of the two peaks of the bimodal histogram (in Figure 3.6) were identified (i and j) and the threshold T to be used defined as:

$$T = \frac{i+j}{2} \quad (3.1)$$

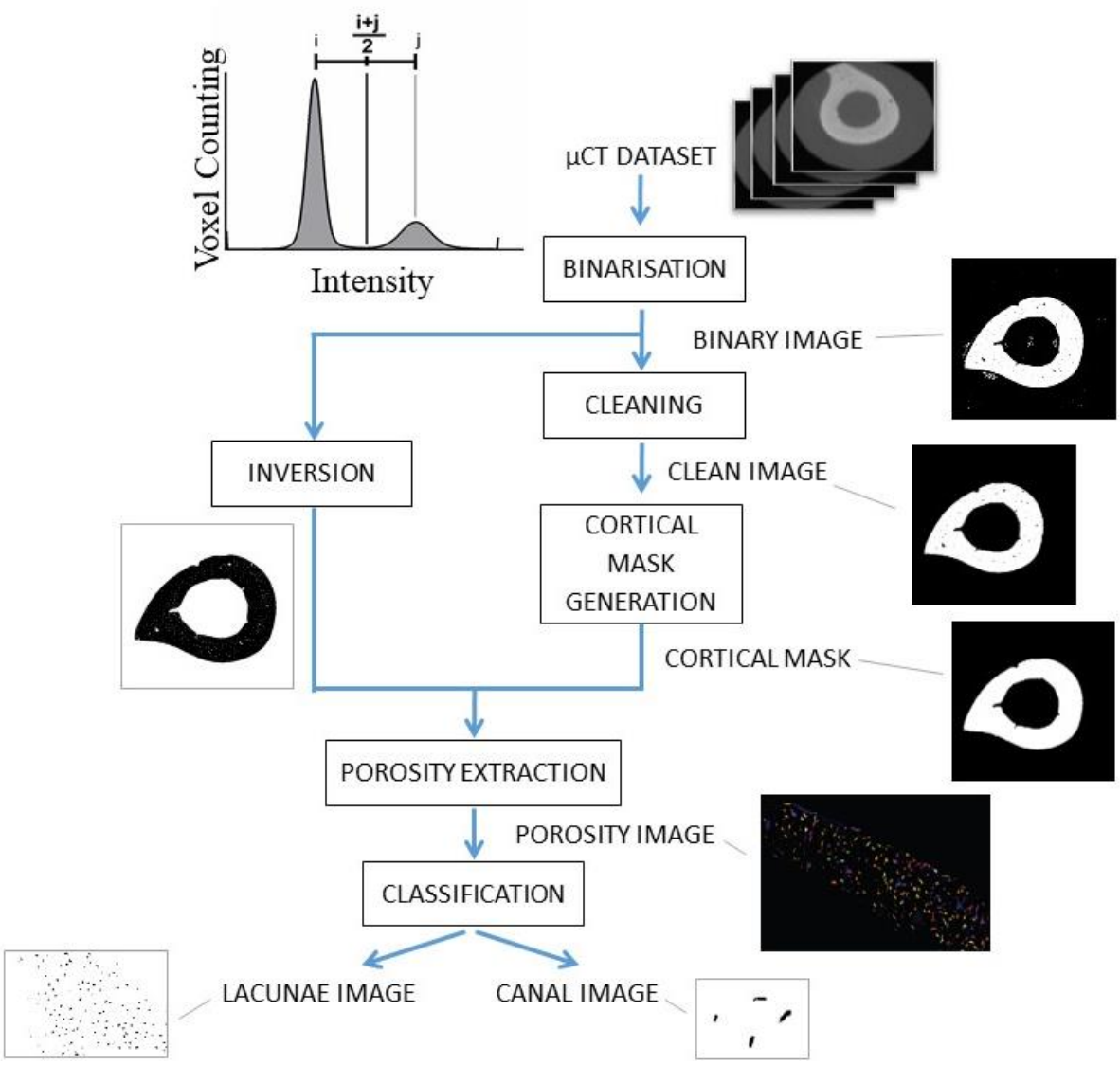

Figure 3.6. Cortical porosity detection, extraction and classification workflow. Datasets are binarised to detect mineralised tissue and cleaned to remove small sports in the background, a cortical mask is created and used to extract the porosity. Porosity objects are then classified into canals and lacunae.

This method for the selection of the threshold as the arithmetic mean (of midpoint) of the values of the two histogram peaks is known as intermodes and it is ideal for images with two components and peaks clearly detectable in the image histogram (as it is the case of bone, where only two objects are detected, namely mineralised and not mineralised segments). This operation is carried out using ImageJ freeware (M.D. Abràmoff; P.J. Magalhães; S.J. Ram, 2004) on the histogram of the 3D image (stack of 2D images). The

output of this process is a binary image with two components: object or mineralised tissue and background or non-mineralised tissue.

Once the binary image has been generated, the following process had the objective to remove small clusters of pixels in the background that were incorrectly detected as mineralised tissue due to image noise. This second step, namely cleaning, starts with a 3D opening operation followed by a component labelling with individual components detected sorted by volume in Avizo. The labelled image is then sieved to keep only the largest component (cortical bone) in Avizo and all the cluster of pixels that were incorrectly included as mineralised tissue removed.

The purpose of the following series of operation was to generate an image of the solid cortex (mask, without pores) that will be used for the extraction of the cortical porosity. A 3D closing operation (Avizo) incorporates the osteocyte lacunae that have been detected as part of the background because of their proximity to the bone surfaces. Subsequently, cortical pores are removed with an operation that fills all the holes smaller than a fixed value (determined by the size of the medullary cavity) in Avizo. A 3D erosion operation (Avizo) thins the solid cortical image to ensure that the final mask image is within the actual mineralised cortex.

In order to extract cortical porosity, the thresholded binary image produced in the first step of the process is inverted and combined with the cortical mask image in an “AND” logical operation (Avizo) resulting in a dataset containing the pores. A 3D opening operation was then applied (Avizo) to separate clusters of pores and remove the smallest spots.

The separated pores are sorted via component labelling and a bounding box is computed for each pore (Figure 3.7). The maximum dimension of each bounding box (max[a,b,c]) was then used to classify the particles into noise, osteocyte lacunae and canals using maximum dimension criteria.

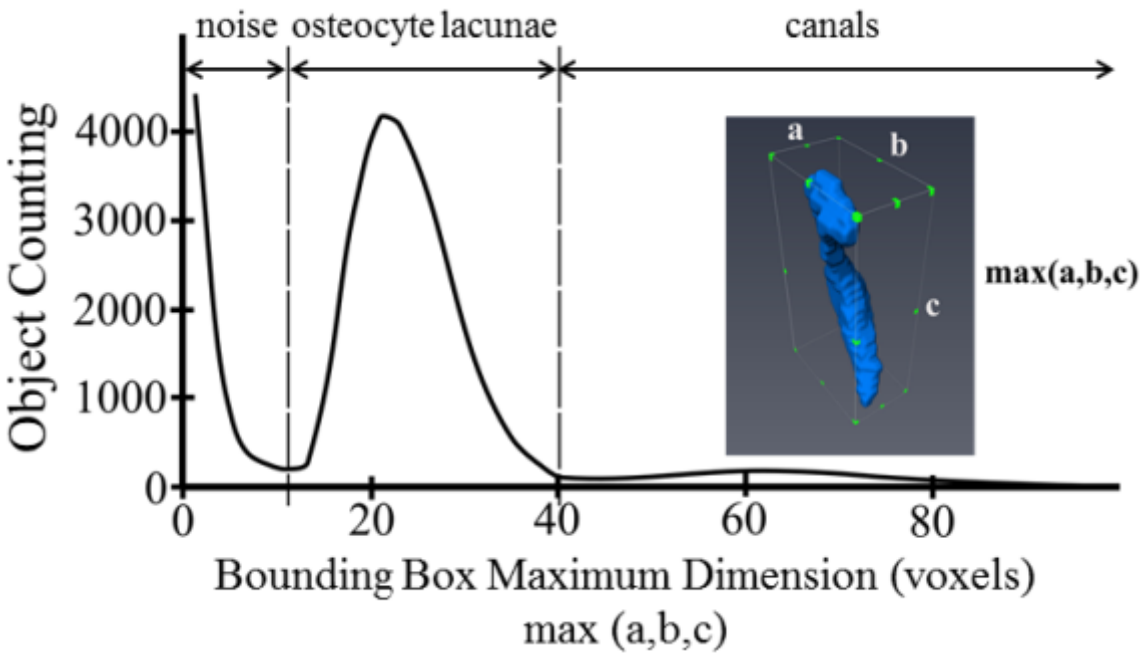

Figure 3.7. Classification of the porosity objects into noise, lacunae and canals based on the maximum dimension of the bounding box of each object (with a, b and c being the values for the three dimensions of the box).

Figure 3.8 shows a 3D rendering of the vascular canals and osteocyte lacunae after the classification operation.

3.2.3 Computation of 3D distances between osteocyte lacunae and vascular canals

Proximity to a blood vessel is a requirement for tissue maintenance and cell survival. Determination of this proximity could be used as an indicator for bone tissue perfusion and to assess changes in the distribution of vascular structures. Figure 3.9 summarises the image processing workflow that was develop within this PhD project for the computation of 3D distances between osteocyte and the vasculature.

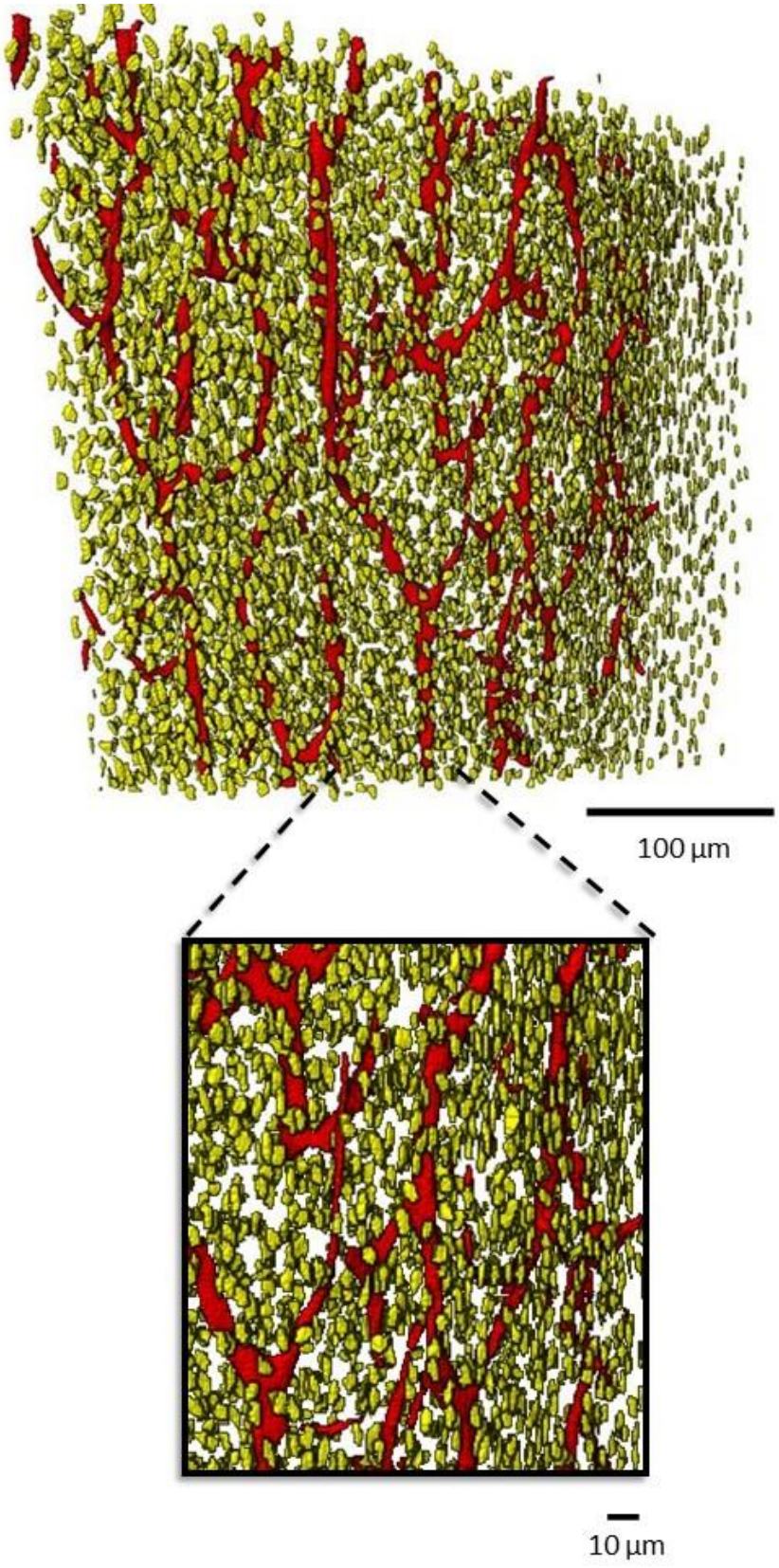

Figure 3.8. 3D rendering of intracortical vascular canals (red) and osteocyte lacunae (yellow).

The cortical mask image from section 3.2.2 generated for the extraction of porosity was combined with the canals image in a subtraction operation (Avizo) to produce a cortical mask perforated by canals. The 3D distance transformation in ImageJ (Ollion et al., 2013) was performed on this perforated mask to compute proximity to a bone surface (where the blood vessels can be found) for every voxel within the image. Figure 3.10 illustrates de concept of distances computation and Figure 3.11 shows the colour mapping of the computed distances on sectioned cortical tissue. This tissue distance image was then used with the location of the osteocytes defined by their centroids to generate osteocyte distance to closest surface images with a multiplication operation (ImageJ). The spatial coordinates (X,Y,Z) of the centroids were computed in Avizo by running a component labelling on the osteocyte lacunae image. The centroids spatial coordinates were processed in Matlab (in-house script) to generate the 3D centroids image.

3.2.4 Quantification: Definition of parameters

Once the cortical porosity features had been extracted from the CT datasets and its spatial relationships computed, the next step was the definition of parameters for quantification. Following quantitative morphometric measures introduced for osteocyte lacunae and the canal network (Schneider et al., 2007), which correspond to standard nomenclature for bone morphometry (Bouxsein et al., 2010; Parfitt et al., 1987), canal volume density (Ca.V/Ct.TV) was computed by calculating the canal volume (Ca.V) divided by the cortical total volume (Ct.TV). Mean canal diameter (⟨Ca.Dm⟩) was calculated with the Thickness command of the ImageJ plugin BoneJ (Doube et al., 2015) (which defines the thickness at a point as the diameter of the greatest sphere that fits within the structure and which contains the point). Canal connectedness (Ca.Co) was defined as the inverse of the number of the biggest canal structures accounting for 80% of the canal volume (Ca.V), which is one for a simply connected vascular network and decreases for an increasing number of disconnected canals that make up the bulk of the canal volume. This measure is

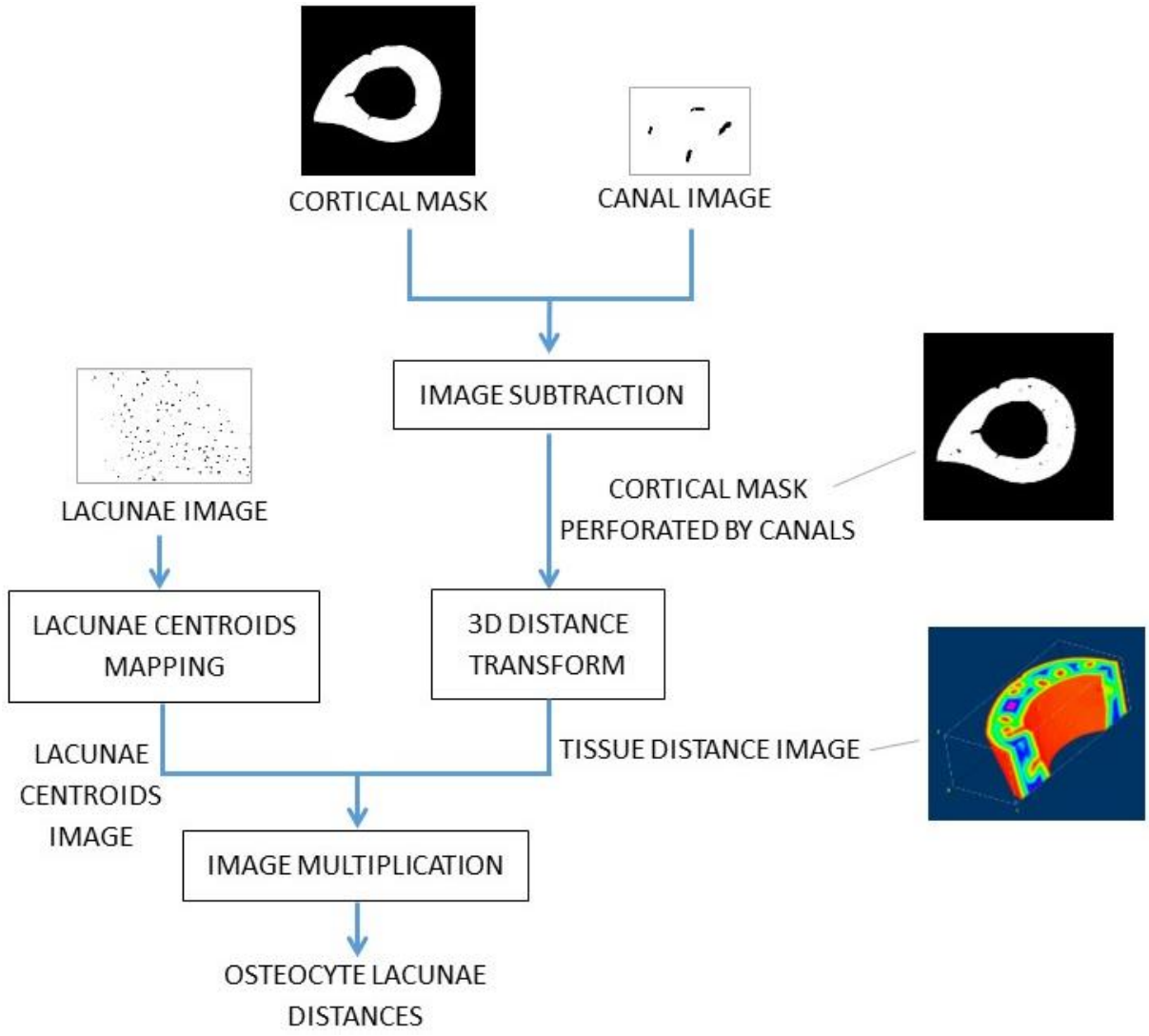

Figure 3.9. Image processing workflow for the computation of osteocyte lacunae distances. The 3D distance transformation generates distances on a cortex perforated by canals. Distances at the locations of the osteocytes are then extracted.

not sensitive to the influence of small canals and characterises the connectedness of the bulk of the canal network (only). It is an indicator for characterisation of the dysconnectivity of the intracortical canals based on the number of individual disconnected structures comprising the canal volume.

Lacuna number density (N.Lc/Ct.BV) was computed by dividing the number of osteocyte lacunae (N.Lc) by the cortical bone volume (Ct.BV).

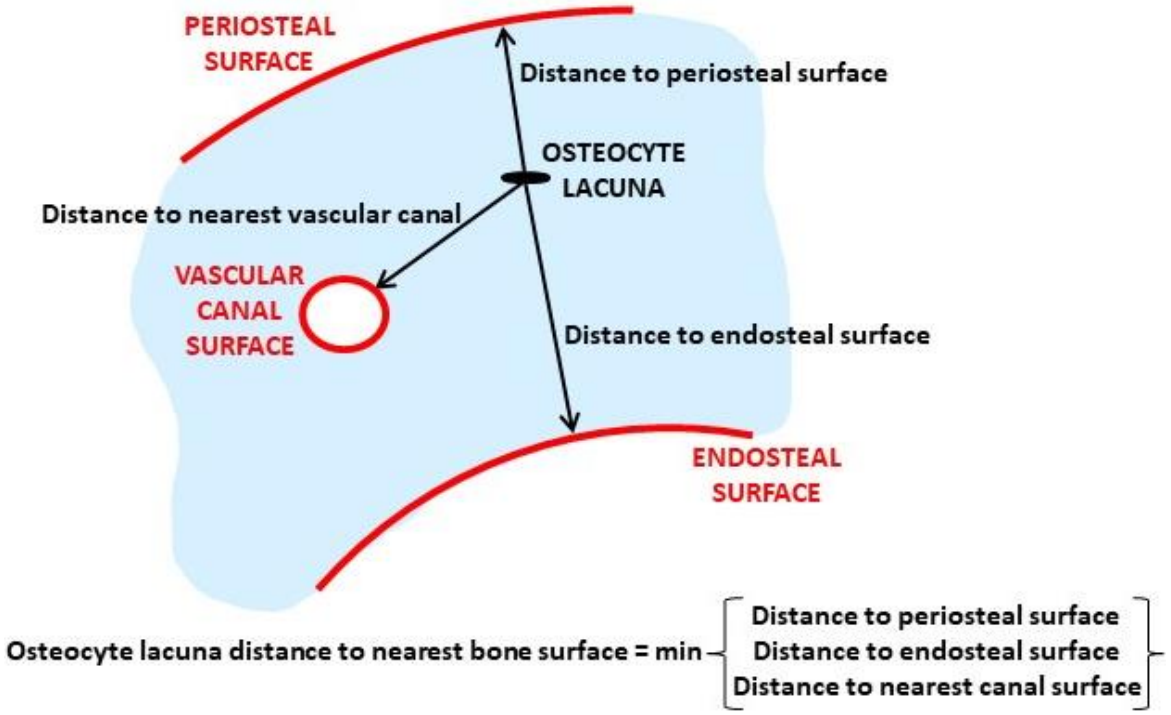

Figure 3.10. Definition of bone surfaces and distances. The 3D distance transform provides the minimum distance to nearest bone surface (endosteal, periosteal or canal) for every voxel within the foreground.

The computed distances for the osteocyte lacunae to nearest bone surfaces (periosteal, endosteal or intracortical vascular canal; Figure 3.11) were converted into distributions (Figure 3.12). Mean (⟨Lc.S.Sp⟩) and 95th percentile (Lc.S.Sp$_{95}$) of the osteocyte lacunae distance distributions were used as indicators for the 3D spatial relationships between vasculature and osteocyte lacunae.

Table 3.2 includes the parameters that were quantified and used as indicators in the following chapters.

Parameter	**Definition**
Ca.V/Ct.TV (%)	Canal volume density
⟨Ca.Dm⟩ (microns)	Mean canal diameter
Ca.Co (arbitrary units)	Canal connectedness
N.Lc/Ct.BV (per 100 cubic microns)	Lacuna number density
⟨Lc.S.Sp⟩ (microns)	Osteocyte lacunae distance distribution mean
$Lc.S.Sp_{95}$ (microns)	Osteocyte lacunae distance distribution 95^{th} percentile

Table 3.2. Parameters used for the quantification and characterisation of cortical porosity.

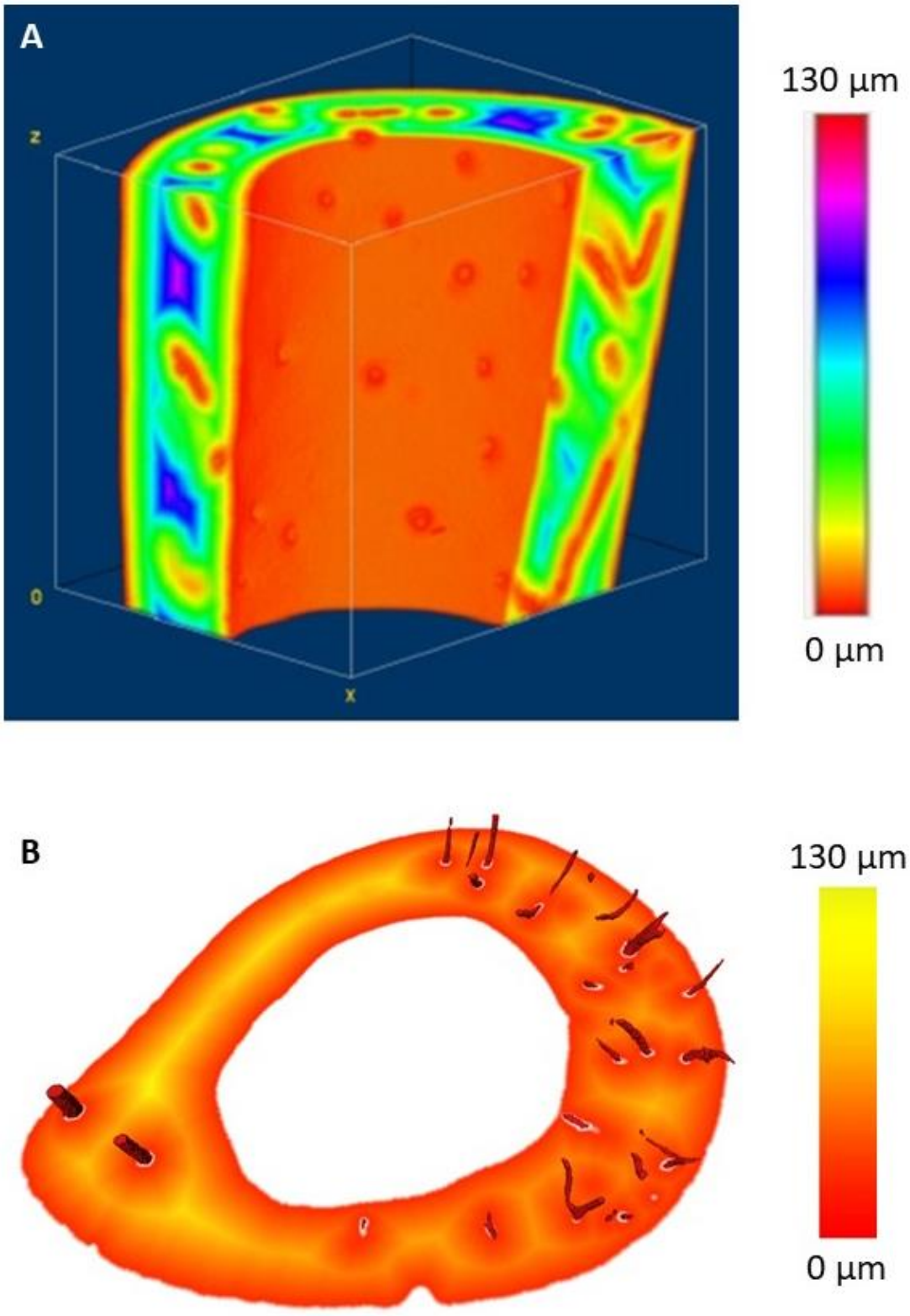

Figure 3.11. 3D tissue distance image as a result of a 3D distance transformation on cortical bone. Different colours stand for different values of proximity to the nearest bone surface (endosteal, periosteal or canal). (A) Segment of the murine tibia longitudinally sectioned and (B) cross-section of the murine tibia with segments of intracortical canals in red.

3.2.5 Selection of the murine skeletal site

High resolution microscopic techniques generally have one inherent disadvantage: the relative small amount of specimen that can be assessed. Magnification and Field of View (FOV) are generally inversely related and, in the case of detecting murine bone microstructure using µCT (at the spatial resolutions explored in section 3.2.1.), this translates into a FOV of a few millimetres, which makes it impossible to capture entire bones within a dataset for most of the murine skeleton (in average only ≈ 10% of the bone could be assessed). Only small portions of the bone specimens could be analysed at once and a decision for the skeletal sites to analyse had to be made. µCT scans for the assessment of the murine bone microstructure can be long and high-priced when using a desktop scanner and require access and displacement of the workforce to a dedicated facility for the case of synchrotron sources. The selection of the suitable skeletal site(s) to look at in these studies was then a prerequisite affecting number of acquisitions, times, costs and analytical efforts. The study of the wrong number of bone regions or looking at the wrong skeletal site could make the project inviable and a careful experimental planning became necessary.

Different bones, and even skeletal sites within the same bone, have different compositions of trabecular and cortical tissue. Since the focus of this thesis was on the cortical bone the presence of cortical tissue was one of the criteria that a suitable skeletal site had to meet. Different bones of the skeleton have different functions: the skull and the ribs, for example have protective function, while the vertebra, femur and tibia are weight bearing structural elements that play a crucial role in whole body support and locomotion. Osteoporotic bone loss and fractures have a preference for weight bearing bones so these were the bones that were pre-selected for the studies. A preliminary investigation was then conducted to explore a vertebra, the femur and the tibia as candidates.

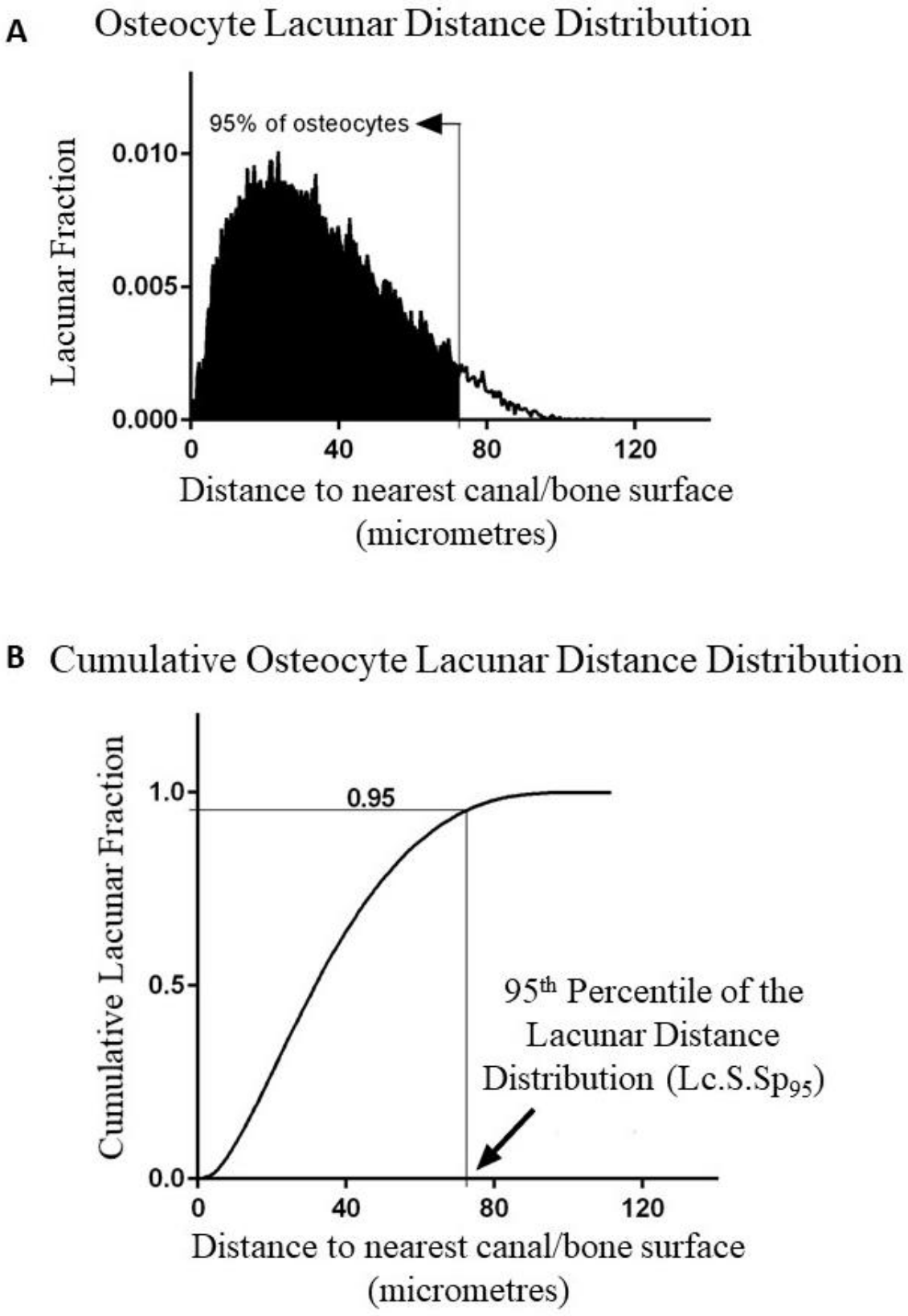

Figure 3.12. Osteocyte lacunar distance distribution (A) and cumulative distribution (B) with definition of 95th percentile.

The L4 vertebra, right femur and right tibia from the skeleton of 1 C57BL/6 15-week old female mouse were scanned using a ZEISS Xradia 510 Versa CT desktop scanner (1.7 µm voxel size). Figure 3.13 shows the references and regions used to locally scan the three bone specimens. For the femur, the reference for scans was taken at the 56% of the whole femur length (calculated from the greater trochanter) as defined by previous investigations (Schneider et al., 2007; Thurner et al., 2010). For the tibia, the small region for local tomography was centred at the tibiofibular junction based on the extensive use of this skeletal site in the literature (Berman et al., 2015; Brommage et al., 2014; Campbell and Sophocleous, 2014; Holguin et al., 2016; Javaheri et al., 2015; Pereira et al., 2015; Warner et al., 2006). In the case of the vertebra, due to its irregular geometry, the region of interest was chosen in a way that most of the bone tissue was captured.

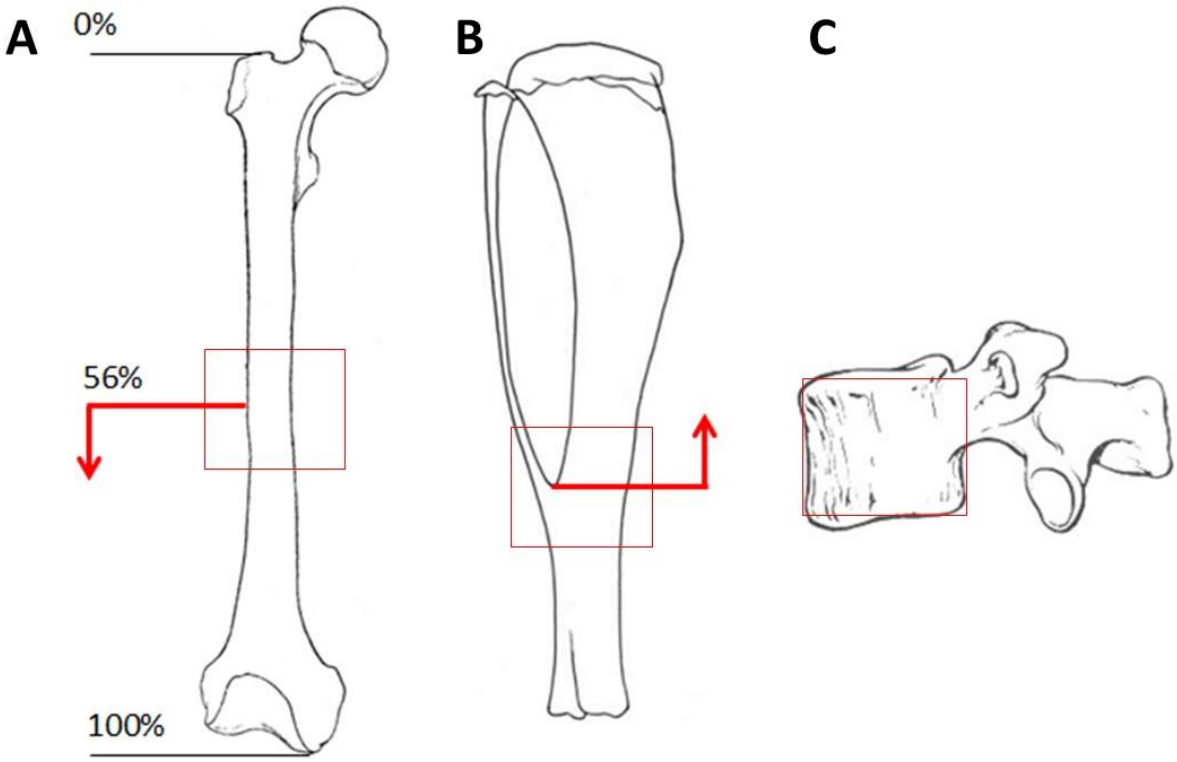

Figure 3.13. Weight bearing bones selected for the initial exploration and scanned areas with references in red colour. Femur (A), tibia (B) and L4 vertebra (C).

It was found that the high geometrical irregularity of the vertebra made the positioning and centring of the specimen difficult and time consuming when setting-up the scans. Additionally, it was found that the diameter of the specimen could not fit in the established FOV linked to the required spatial resolution. Positioning and centring of the midshaft of the femur was found to be less complicated; once the coordinates of the bone ends were found, the reference for scans was calculated and the sample positioned in few minutes. The tibia was the most convenient bone to set-up. The intersection between tibia and fibula provided a highly visible and easily identifiable reference that allowed the quickest set-up.

Trabecular tissue was highly present in the vertebra dataset. In the case of the femur, trabecular tissue could also be observed but to a lesser extent, whereas the tibiofibular junction provided a CT dataset that was purely cortical.

Mineralised geometry with cortical microstructure was detected and cortical porosity extracted and classified into vascular canals and osteocyte lacunae for the three datasets following the methodology described in section 3.2.2. Figure 3.14 shows the three scanned volumes and Figure 3.15 the extracted canals and lacunae in red and yellow respectively. Canal volume and osteocyte lacunar number densities were computed for the three datasets and the results are shown in Figure 3.16.

Vascular canals were evident in the three skeletal sites with a high heterogeneity in the vascular canal density across the three skeletal sites and a more homogenous distribution of osteocyte lacunae. The scanned region of the tibia was the less vascularised whereas the midshaft of the femur was found to have the highest vascular canal density. Vascular canals seemed evenly distributed within the femoral midshaft whereas the tibiofibular junction presented regions of very low canal density and regions where canals were more concentrated.

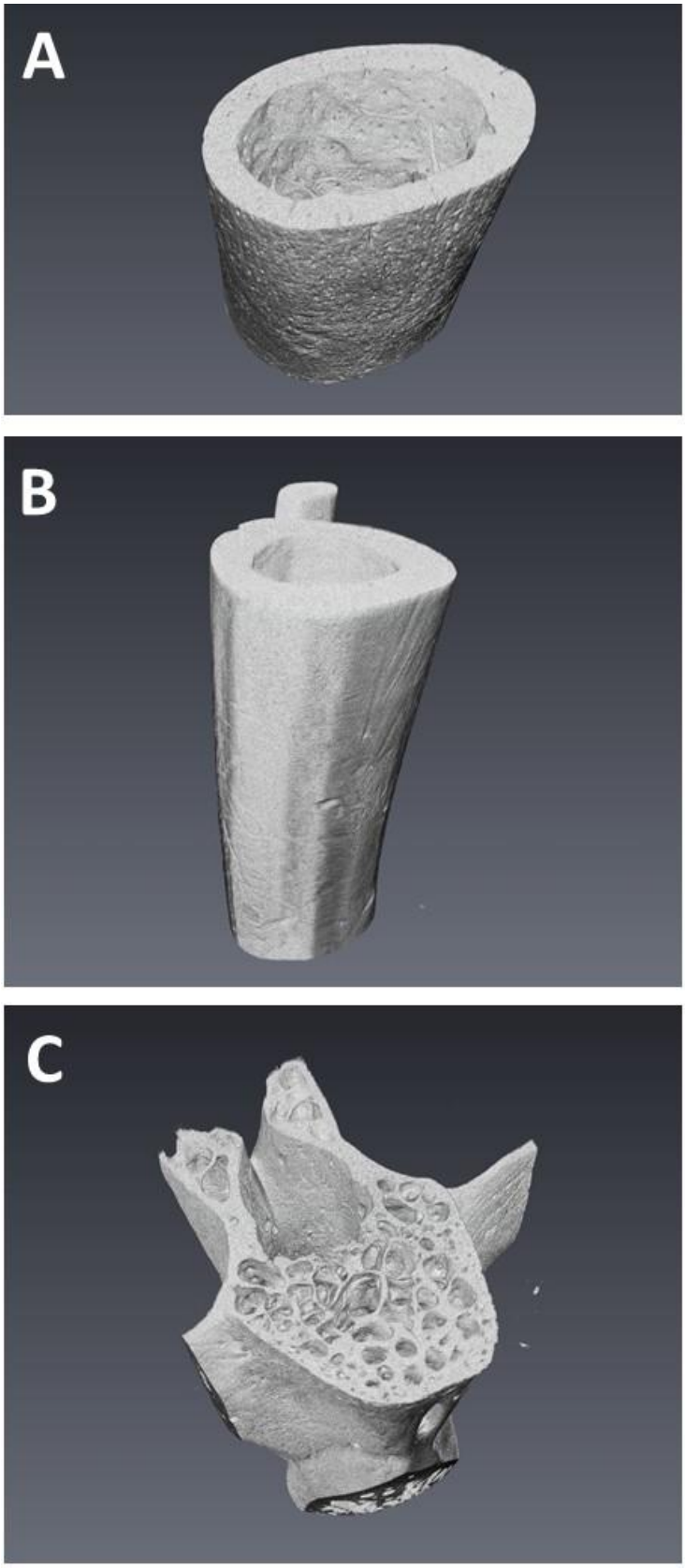

Figure 3.14. 3D rendering for the three scanned skeletal sites. Femoral midshaft (A), tibiofibular junction (B) and L4 vertebra (C). Voxel size 1.7 microns.

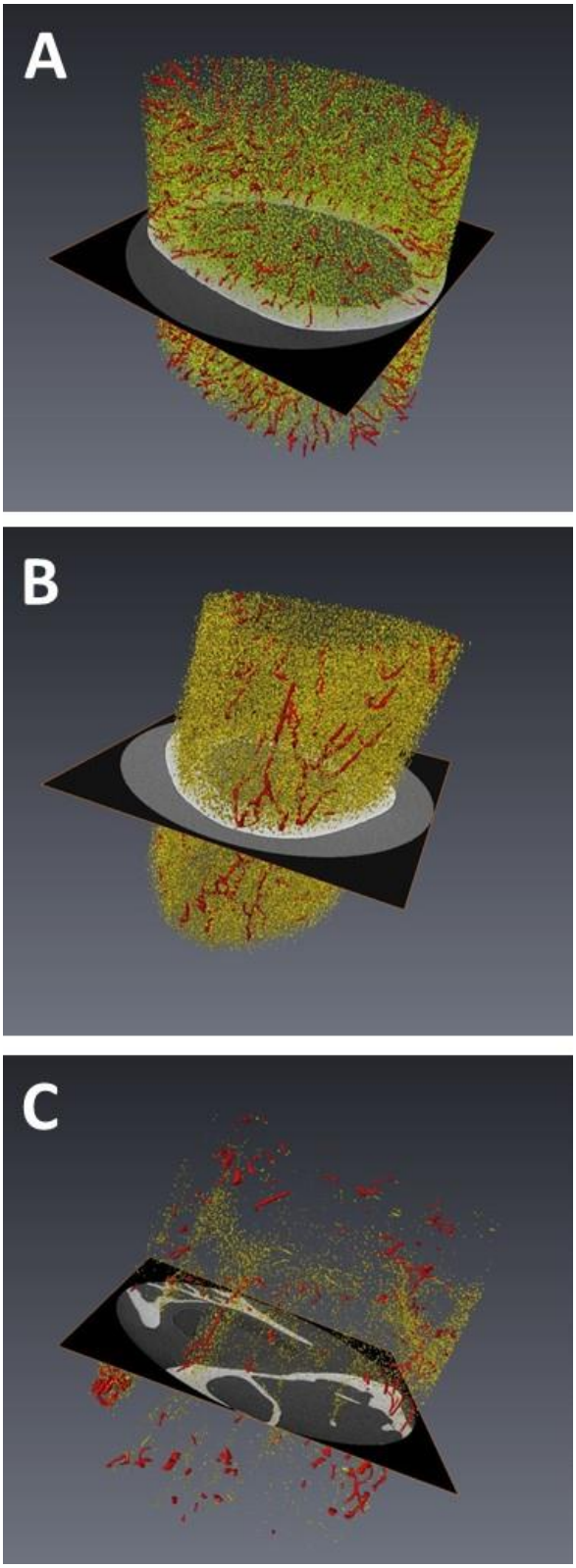

Figure 3.15. 3D rendering of vascular canals (red) and osteocyte lacunae (yellow) for the datasets in Figure 3.14 with cross-sectional CT slice showing the mineralised tissue. Femoral midshaft (A), tibiofibular junction (B) and L4 vertebra (C).

Table 3.3 summarises the findings of this exploratory analysis and highlight advantages and disadvantages related to the three skeletal sites.

	Reference for scans	Scan set-up	Fits in FOV	Trabecular bone
Femur	Requires calculations	Easy but not fast	Yes	Some trabecular structures
Tibia	Very clear reference	Very easy and fast	Yes	Rarely
Vertebra	Irregular shape	Difficult and long	No	High presence

Table 3.3. Summary of advantages and disadvantages presented by the three skeletal sites included in the exploratory analysis: femur, tibia and vertebra. Colour codes are: green=desirable attribute, red=not desirable attribute and orange=intermediate. (FOV=field of view).

Based on these results, it was concluded that the tibiofibular junction was the most convenient candidate according to the established criteria. Scans of the tibiofibular junction were easy and fast to set-up, the specimen diameter fitted in the FOV and the junction provided a clear landmark that could be used as a reference and would allow systematic scans of exactly the same bone region providing consistency across biological replicates in further experiments. Bone tissue was purely cortical for the junction and the presence of regions of high and low vascular densities combined within the same site opened the door to additional biological questions. The vertebra was found to be the most problematic specimen: its highly irregular shape and dimensions made extremely hard to define a region of interest, the diameter could not be fitted into the FOV and most of the captured tissue was trabecular. The femoral midshaft lay somewhere in between the tibia and the vertebra with a defined reference for scans that needed calculations and low

presence of trabecular bone. For these reasons, the tibia was identified as the best candidate for further evaluation and additional scans and analyses were carried out at the junction to characterise this skeletal site.

3.2.6 Synchrotron radiation based µCT

All the bone scans used for the development and optimisation of this methodology were performed using the ZEISS Xradia Versa desktop scanner available in the facilities of the Faculty of Engineering of the University of Southampton. However, the PhD candidate was awarded with synchrotron radiation beamtime in the facilities of the Swiss Light Source (SLS) in two occasions, which allowed the reduction of scanning costs and acquisition times while improving image quality. As an example, a typical acquisition with the desktop scanner takes 8 hours approximately (0.85 µm voxel size) whereas scanning of a sample in the SLS facilities only takes 6 minutes approximately (0.65 µm voxel size). In order to explore differences in image quality datasets from desktop and synchrotron scans were compared.

Figure 3.17 shows two reconstructed slices from desktop and synchrotron scans, assessed with 0.85 and 0.65 µm voxel sizes respectively with the objective to compare the two alternatives. Figure 3.18 shows the histograms of the two reconstructed slices in Figure 3.18. The background and mineralised tissue distributions of pixels are better defined on the synchrotron scan. The standard deviation of the broader peak in the desktop scan was 4513 whereas the standard deviation of the broader peak in the synchrotron scan was 1996. This translated into better segmentation results for synchrotron scans.

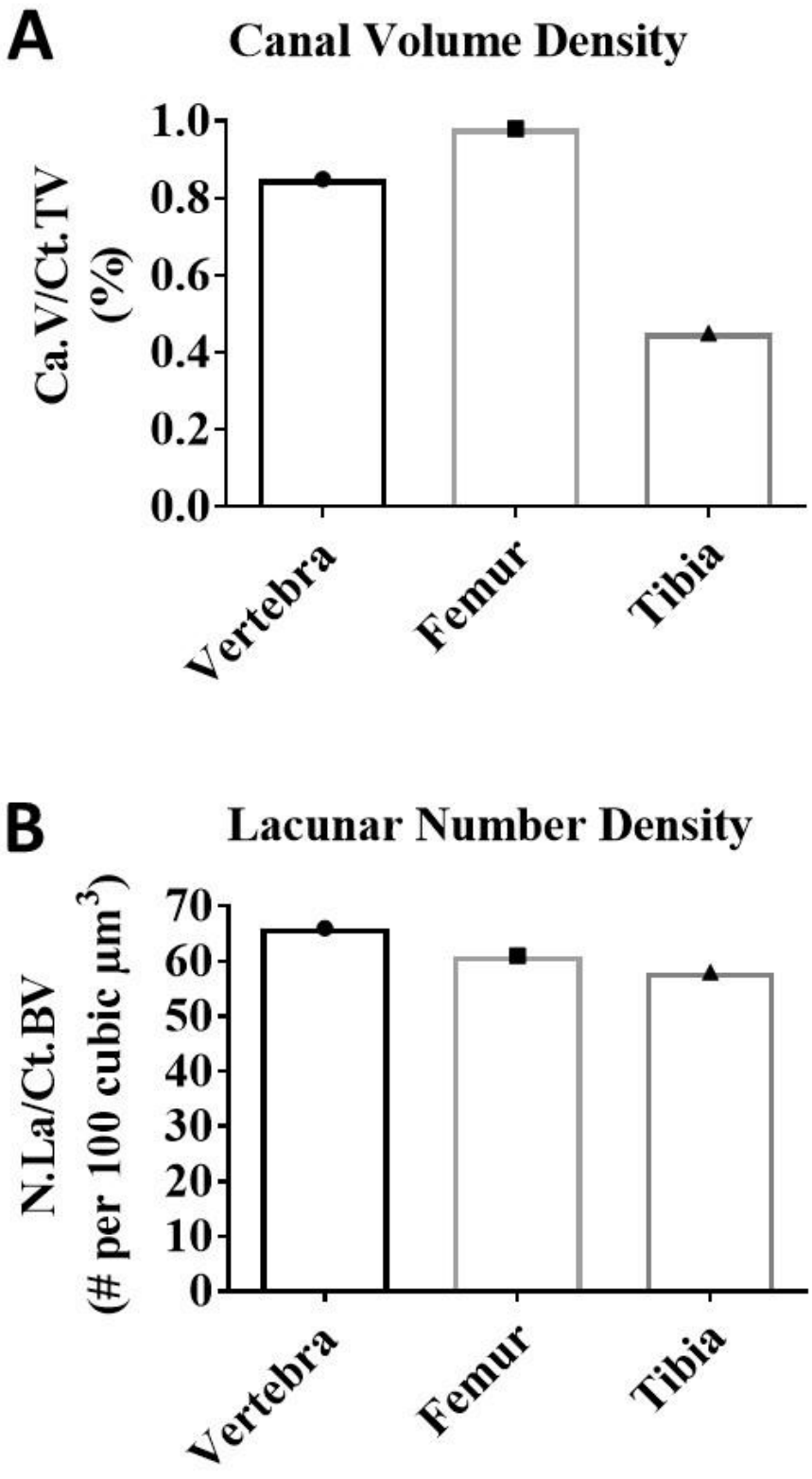

Figure 3.16. Vascular canal density (A) and osteocyte lacunar number density (B) for three selected skeletal sites. Data for 1 vertebra, 1 femur and 1 tibia in the initial exploratory analysis.

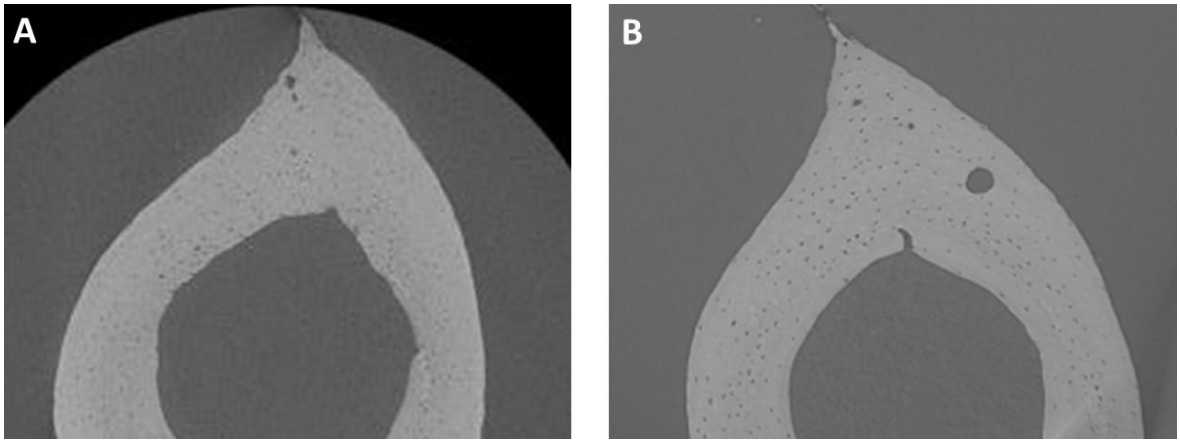

Figure 3.17. Reconstructed slices from (A) desktop scan and (B) synchrotron scans – Data assessed at 0.85 and 0.65 µm voxel sizes respectively – Tibiae from 2 C57BL6 female mice, 15 weeks old.

Figure 3.19 shows regions of the binarised images after thresholding. It is important to note that this is not comparing the same bone sample. Figure 3.20 shows the 3D rendering of osteocyte lacunae extracted from the binarised images shown in Figure 3.19. It is clear that the synchrotron image had less noise with a better defined shape for the lacunae.

Taking into account scanning costs, times and image quality, synchrotron was the best option to scan the bones required to answer the biological questions. For this reason, the results shown in the following chapters are derived from measurements carried out at the SLS.

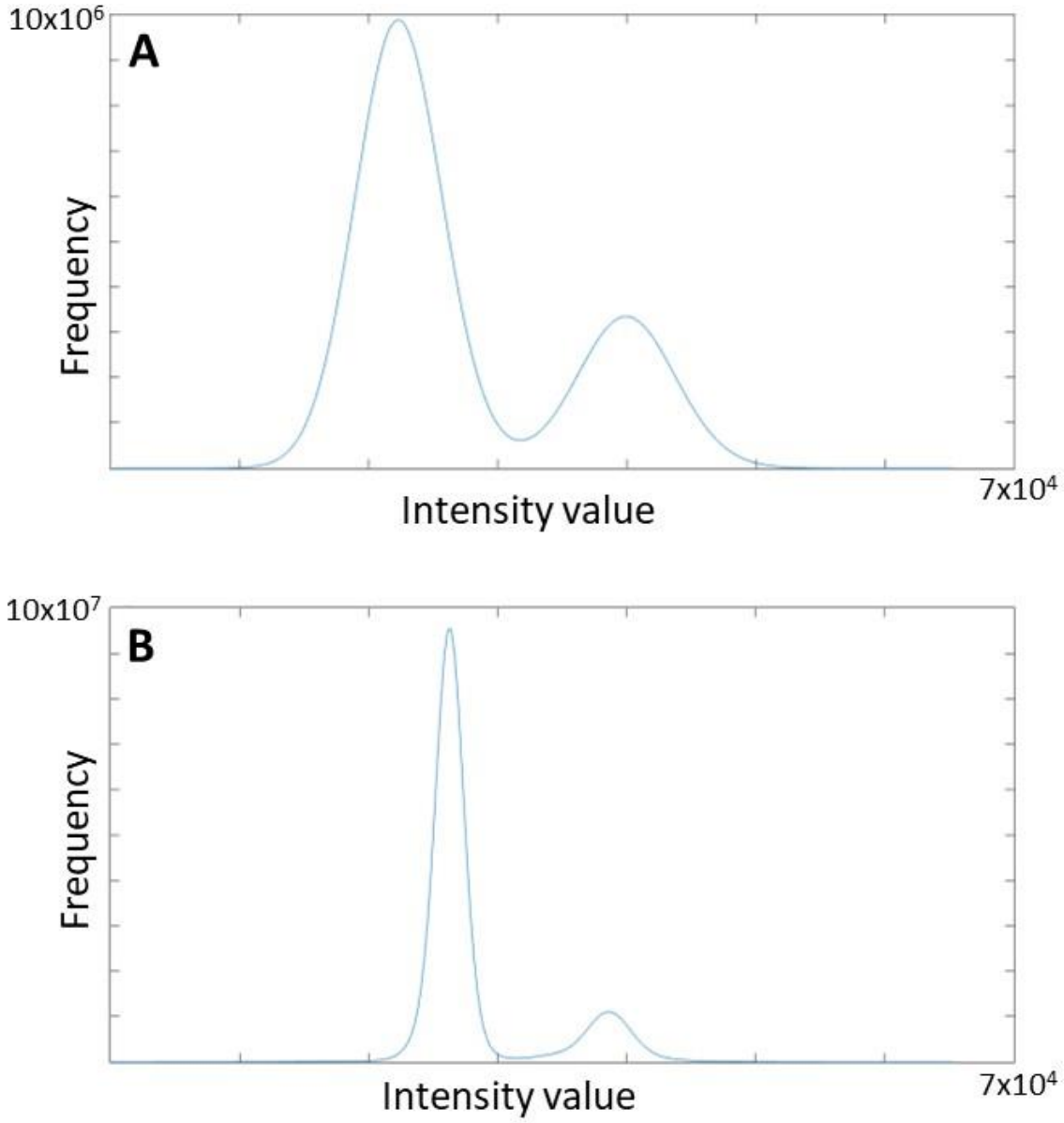

Figure 3.18. Histograms of the reconstructed slices shown in Figure 3.17. (A) Desktop scan and (B) synchrotron scan.

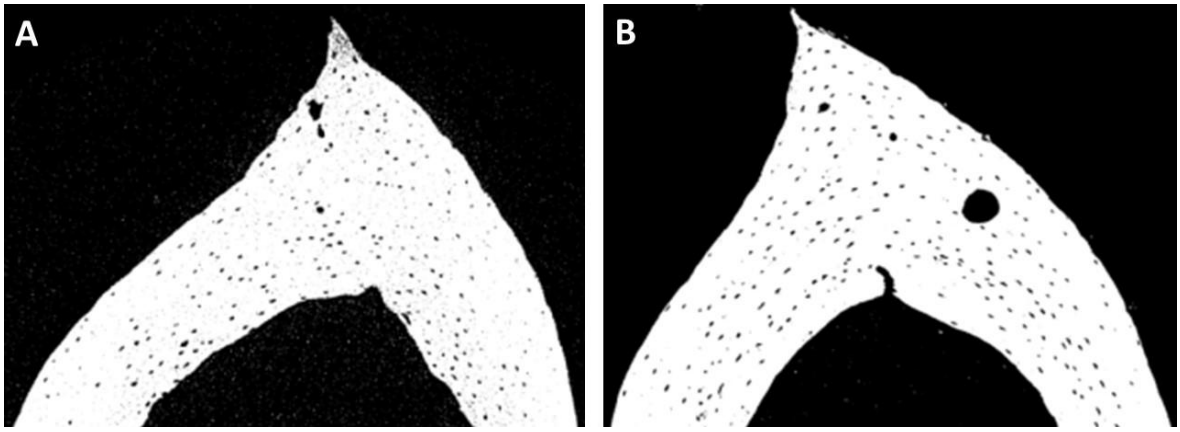

Figure 3.19. Thresholded images of the datasets in Figure 3.17. (A) Desktop scan and (B) synchrotron scan.

3.3 Discussion

This chapter has explored the effect of the spatial resolution on the detection and extraction of cortical porosity. For the investigation of bone vascularisation within this thesis, the finest structures were the osteocyte lacunae. The average murine osteocyte lacunae can be idealised as an ellipsoid of dimensions 14:7:4 µm. It has been proved now that that resolutions close to and above the micrometre are enough to accurately detect osteocyte number. Although other osteocyte parameters such as volume, shape and orientation cannot be correctly estimated at those resolutions; this is acceptable as long as lacunae are not missing. In the end, osteocyte lacunae will be treated as points defined by the location of their centroids and the detection of their presence is sufficient for the purpose of this investigation. Furthermore, studies such as Copper et al. (Cooper et al., 2007b) have already shown, with working resolutions much poorer than the ones presented here, that µCT is a reliable and accurate tool. The accuracy and reliability of µCT technology is largely due to the fact that these systems have been highly developed, validated and commercialised over the last 20 years. They have been widely used in many fields including geology, material science and biomedicine as well as input for modelling in design and manufacturing. In particular, in the field of bone research the accuracy and

repeatability of µCT imaging have become evident with the ability to detect differences between diseased and healthy bones.

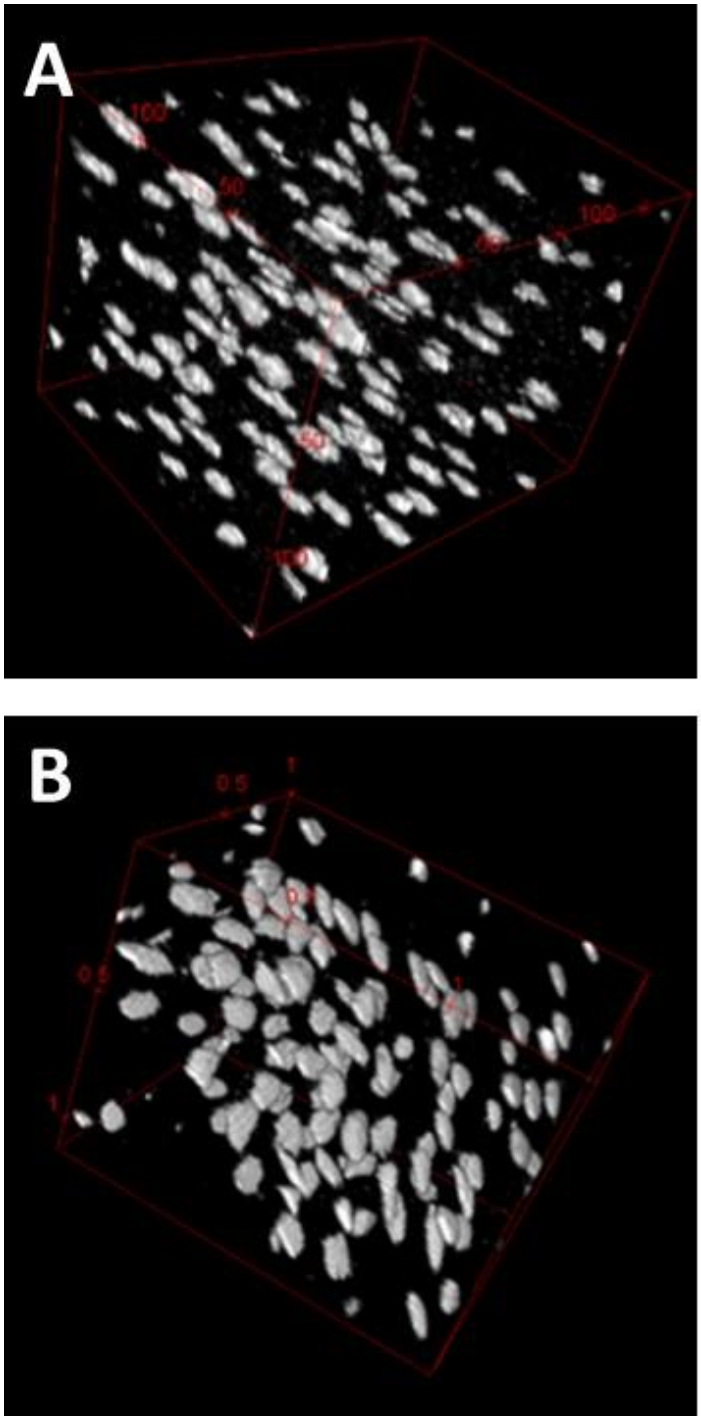

Figure 3.20. 3D rendering of osteocyte lacunae extracted from the datasets in Figure 3.17. (A) Desktop and (B) synchrotron.

Osteocyte survival requires proximity to nutrient vessels and the computation of distances that has been developed within this thesis allows the 3D quantification of this proximity. In particular, distances to the nearest bone surface (endosteal, periosteal and canal) where the bone vasculature can be found have been computed.

Parameters for the quantification of cortical bone vasculature have been defined and will be used to test differences due to age and the lack of the proangiogenic factor VEGF in the following chapters.

The exploratory analysis of the three weight bearing bones identified the murine tibia as the best candidate to study the intracortical vasculature for the following reasons: 1) the entire cortical ring can be fitted into the field of view when scanning at the required resolution (this was not the case for the vertebra); 2) the tibiofibular junction provides a clear landmark that can be used as a reference to set the scans and make sure that the same skeletal site is being scanned and compared across biological replicates, which provides a systematic approach for the scanning and the analysis as well as consistency when comparing different experimental groups. The presence of this landmark made the scan set-up quicker (that was not the case for the femur, since dimensional calculations needed to be carried out to work out the reference and region to be scanned, and this was not the case for the vertebra, where the irregular geometry made very complicated to keep a regional consistency); 3) bone tissue is purely cortical at the tibiofibular junction (this was not the case for the vertebra and some trabecular structures were found at the midshaft of the femur) and the focus of these studies were on the intracortical vasculature; 4) visual inspection of the distribution of intracortical canals revealed presence of areas of high and low canal densities (in opposition to the femoral midshaft where vascular canals were evenly distributed within the cortex), this opened the door to the study of these different types of regions within the same skeletal site. On top of all this, the tibia was identified in the literature as one of the most well characterised bones to be studied and used as animal models for osteoporosis (Brommage et al., 2014; Campbell and Sophocleous, 2014; Holguin et al., 2016; Javaheri et al., 2015; De Souza et al., 2005; Warner et al., 2006). For all these

reasons, a decision was made and the tibiofibular junction was selected as the region to study and use to evaluate differences due to age and disease.

Chapter 4: Results II – Age-related changes in the intracortical vascular canal network of the murine tibiofibular junction

4.1 Introduction

Age-related bone loss and fragility are a growing problem and today little is understood about the onset of degenerative bone diseases such as osteoporosis. There are evidences for a decline in oxygen consumption in bone with a decreased vascular conductance and reduced vasculature in the bone marrow with age (Alagiakrishnan et al., 2003; Burkhardt et al., 1987; Dinenno et al., 1999; Reeve et al., 1988). Also, we know that the expression of blood vessel attracting signals, in particular VEGF, is reduced with age in multiple cell types (Efimenko et al., 2011; Jiang et al., 2008; Pola et al., 2004; Rivard et al., 1999; Wilson et al., 2010) and reduced levels of circulating VEGF have been found in postmenopausal osteoporotic women (Senel et al., 2013). All this indicating that the bone vasculature could be altered with ageing and disease. Despite cortical bone being the most important contributor to skeletal mass (Burr, 2016), age-related bone loss (Zebaze and Seeman, 2015) and – at many anatomical sites – to bone strength (Ferretti et al., 1995; Holzer et al., 2009; Mazess, 1990), it remains unclear whether alterations in the intracortical vasculature occur with age, if they can influence age-related bone changes and consequently to what extent preservation of the cortical vasculature could prevent bone fractures. The aim of the studies described within this chapter was to assess early alterations of the intracortical vasculature with age using the murine tibiofibular junction. In order to do so, the skeletal site selected in Chapter 3 was first further evaluated and characterised in the young-adult mice. Tibiofibular junction from animals at two different ages were imaged and analysed to detect mineralised tissue, extract and separate porosity and compute distances between canals and lacunae. Results revealed age-related changes in the distribution of vascular canals and distances to osteocyte lacunae.

4.2 Methodology

4.2.1 Animals

Mice and surgical procedures using for the studies within this thesis were handled according to the guidelines of the Animals (Scientific Procedures) Act 1986. The murine bones required for the studies included in this thesis were obtained in compliance with EU Directive 2010/63/EU and have been approved by the Animal Welfare and Ethical Review Board of the University of Southampton, United Kingdom. C57BL/6 female mice (Charles River Laboratories, Wilmington, Massachusetts, USA) were euthanised by cervical dislocation. C57BL/6 is the most widely used inbred strain of laboratory mouse with a permissive background for maximal expression of most mutations. The left and right tibiae were harvested, cleaned of soft tissue, fixed in 4% paraformaldehyde (pH 7.4) for 48 hours on a tube roller at 4°C and preserved thereafter in 70% ethanol prior to µC imaging and histology. Right tibiae were used for µCT imaging and contralateral left tibiae for histological analysis. Right tibiae were embedded in histological paraffin wax to prevent sample movement during µCT.

The tibiofibular junctions of 15-week-old (n=6) and 10-month-old (n=6) C57BL/6 female mice were scanned using SR CT at the TOMCAT beamline of the SLS at a voxel size of 0.65 µm and datasets analysed as described in Chapter 3. 15 weeks old mice were chosen as they considered to be adults with mineral and organic content of the bone reaching a steady state (Somerville et al., 2004) and were compared with 10 month old animals which have been shown to present age-related skeletal changes (Halloran et al., 2002).

4.2.2 Histological examination

The tibiae of 15-week-old (n=3) and 10-month-old (n=3) C57BL/6 were dehydrated by immersing the tissue in a series of ethanol solutions of increasing concentrations until 100% was reached and the tissue could be infiltrated with the embedding material. Bone cutters (Fine Science Tools, California, USA) were used to section just above the tibiofibular

junction and cut the upper region of the tibia off. Following dehydration, bones were soaked for 24 hours in polymethylmethacrylate (PMMA) at 4ºC (undecalcified tissue). PMMA blocks were ground down using a grinder-polisher (MetaServ 250, Buehler, Illinois, USA) so that the cut surface was flat. 10-µm sections were cut out from the proximal end to trim the bone using a microtome (Leica Biosystems, Wetzlar, Germany) until the tibiofibular junction was reached. 5-µm sections were cut and one drop of 80% isopropanol solution added to each section to prevent folding. Sections were pressed in an incubator at 37ºC overnight to dry the tissue and stained with either Pentachrome or Giemsa to visualise endothelial cells. 3 stained sections per subject were analysed (3 subjects per age group). Quantification of canal occupancy was carried out in the undivided cortical ring manually by detecting the total number of canals and the number of canals filled with blood vessels.

4.2.3 Statistical analysis

To analyse difference between groups of animals in the case of one factor, non-parametric Mann-Whitney tests were used to provide for more robust analysis given the relative small sample sizes. For the analysis of two factors, statistical significance the hypothesis was evaluated by a two-way ANOVA (due to the lack of a reasonable non-parametric alternative) combined with non-parametric post-hoc tests for a more conservative analysis. To preserve statistical power, the number of comparisons between groups were limited, differences evaluated via Mann-Whitney tests or Wilcoxon matched-pairs signed rank tests when applicable. All statistics were performed using GraphPad Prism version 6.0 for Windows (GraphPad Software, La Jolla, CA, USA). Data included in this thesis are always expressed as mean ± standard deviation.

4.3 Results

4.3.1 Characterisation of the young-adult tibiofibular junction

Figure 4.1 shows one of the scanned tibiofibular junctions and the extracted vascular canals. Table 4.1 shows the results of the analysis for the 6 animals. Vascular canals were found not evenly distributed within the cortical ring. In particular, canals seemed concentrated in some areas of the cortex and not present in others, which means that some regions of the bone tissue where not relying on the intracortical vascularisation for nutrition. In order to further explore this, intracortical canals were digitally removed to evaluate their effect on the distances to endosteal and periosteal surfaces. Figure 4.2 summarises the results of this analysis. While the anterior and the posterior regions of the cortex where highly perforated by canals, the presence of canal structures in the lateral and medial quadrants was rare. In the presence of intracortical canals, the majority of osteocyte lacunae were found positioned within ≈40 μm from the nearest bone surface (source of blood) in young cortical bone, with ≈120 μm being the largest distance measured (Figure 4.2A/C). In the hypothetical situation of a lack of intracortical vascularisation (when intracortical canals were excluded from the analysis of distances) (Figure 4.2A/B) the maximum distance to the nearest bone surface increased by 63% (p=0.031, Figure 4.2A/C). The region of the cortical tissue where this increase in distances was taking place was identified (red area in Figure 4.2D) indicating that the posterior region of the tibiofibular junction was more sensitive to the presence of intracortical canals.

The cortex was then divided in 4 quadrants and the analysis carried out locally. Figure 4.3 shows the results of this local analysis. The local analysis confirmed that anterior and posterior regions of the tibiofibular cortex were highly vascularised when compared with the lateral and medial quadrants, with very low presence of canals. No regional differences were found in mean canal diameter (p=0.495). Lacunar number density was similar in the four regions (p= 0.194). Differences in the vascular networks in anterior and posterior regions were observed. The posterior region was found to be more vascularised than the anterior (2.276 times higher, p=0.031). The structure of these two networks were also different, in particular the posterior arrangement of vascular canals was found to be more interconnected than the anterior (p=0.031, Figure 4.3D/4.4). The canal structures also

seemed to be orientated differently, with canals in the posterior region orientated longitudinally (Figure 4.3C). Together these data suggest that intracortical vasculature is heterogeneously distributed within the tibiofibular cortex, with differences in density and structure.

The local analyses of distances revealed that osteocyte lacunae can be found closer to the bone surfaces in the anterior region than other regions of the cortex (p=0.031; Figure 4.5A/B).

Histological examination was carried out to validate the presence of vascular structures within the cortical canals. Figure 4.6 presents details of cortical canals stained with either Pentachrome or Giemsa. % of canals occupied by blood vessels were computed and the results showed that 79.226 % (± 6.080) of the cortical canals were filled with capillaries.

4.3.2 Age-related changes in the intracortical vasculature

When the undivided cortices were analysed, results showed that 10-month-old mice have significantly thinner cortices compared to 15-week-old animals at scanned region (-13.04%, p=0.002; Figure 4.7B). No significant changes were found for the canal volume density (p=0.056; Figure 4.7C/D/E) or canal diameter (p=0.898; Figure 4.7F). In addition, no significant differences between age groups were identified in measurements of lacunar number density (p=0.898; Figure 4.7G) or mean lacunar distance distribution (p=0.093; Figure 4.8) when the undivided tibiofibular junction region was analysed but 95th percentile of the lacunar distance distribution was found to increase in older animals (7.35%, p=0.002; Fig. 4.7H) which meant that osteocyte lacunae were getting farther from the bone surface (source of blood and more deeply embedded in the mineralised matrix) and motivated the local analysis of the tibiofibular cortex.

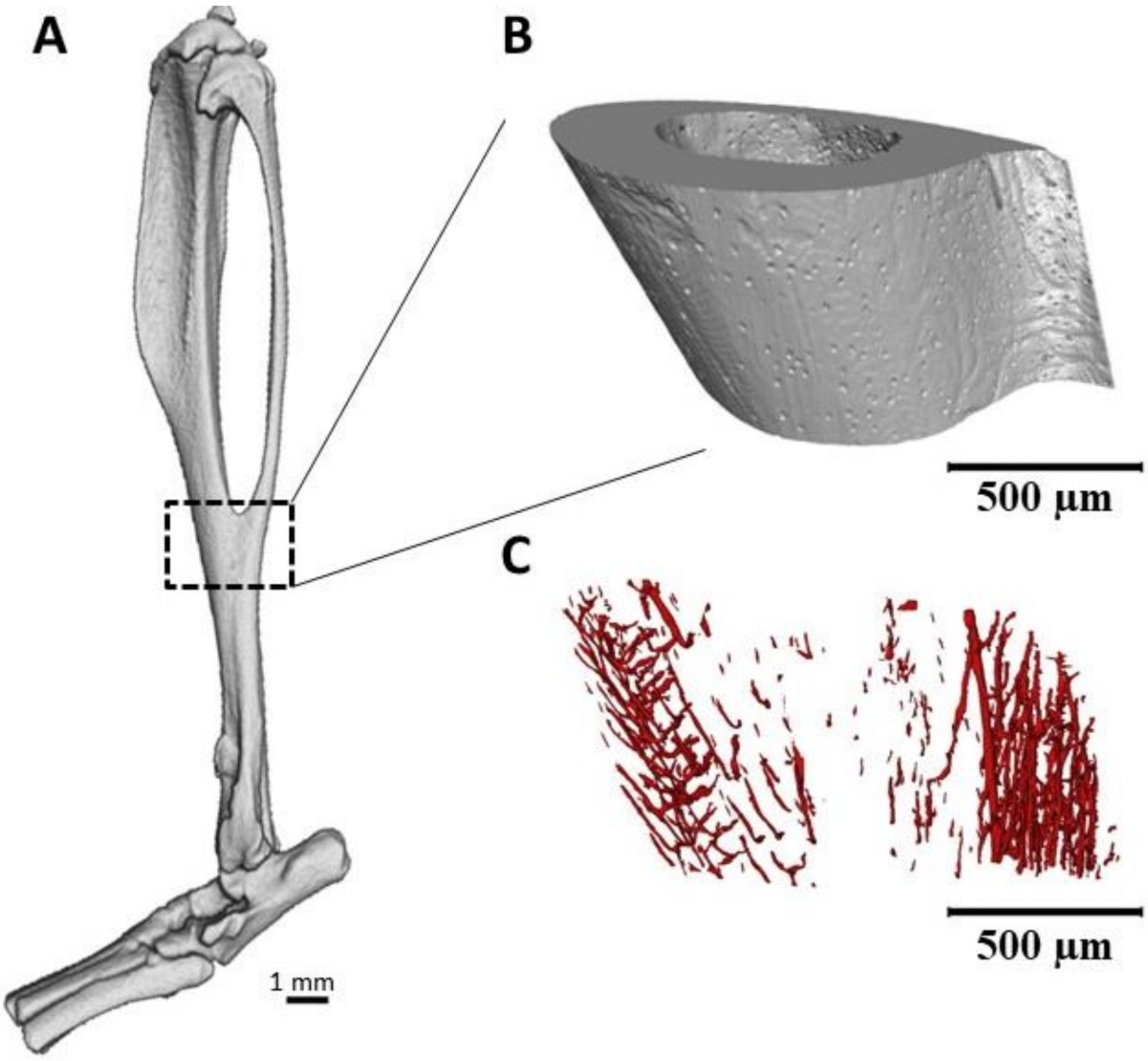

Figure 4.1. Murine tibia, scanned region and distribution of vascular canals assessed by SR CT. CT image of entire murine tibia and location of the tibiofibular junction (A) with magnified scanned region (B) using SR CT. 3D rendering of intracortical vascular structures within the scanned region (C). 0.65 microns voxel size.

Parameter	15-week-old
Ct.Th (micrometres)	221.380 ± 5.956
Ca.V/Ct.TV (%)	0.585 ± 0.111
<Ca.Dm> (micrometres)	7.103 ± 0.621
N.La/Ct.BV (per 100 cubic micrometres)	61.566 ± 1.011
La.S.Sp$_{95}$ (micrometres)	71.025 ± 1.857
<La.S.Sp> (micrometres)	34.264 ± 0.866

Table 4.1. Indices for the tibiofibular junction. Data is mean ± SD, n=6 mice.

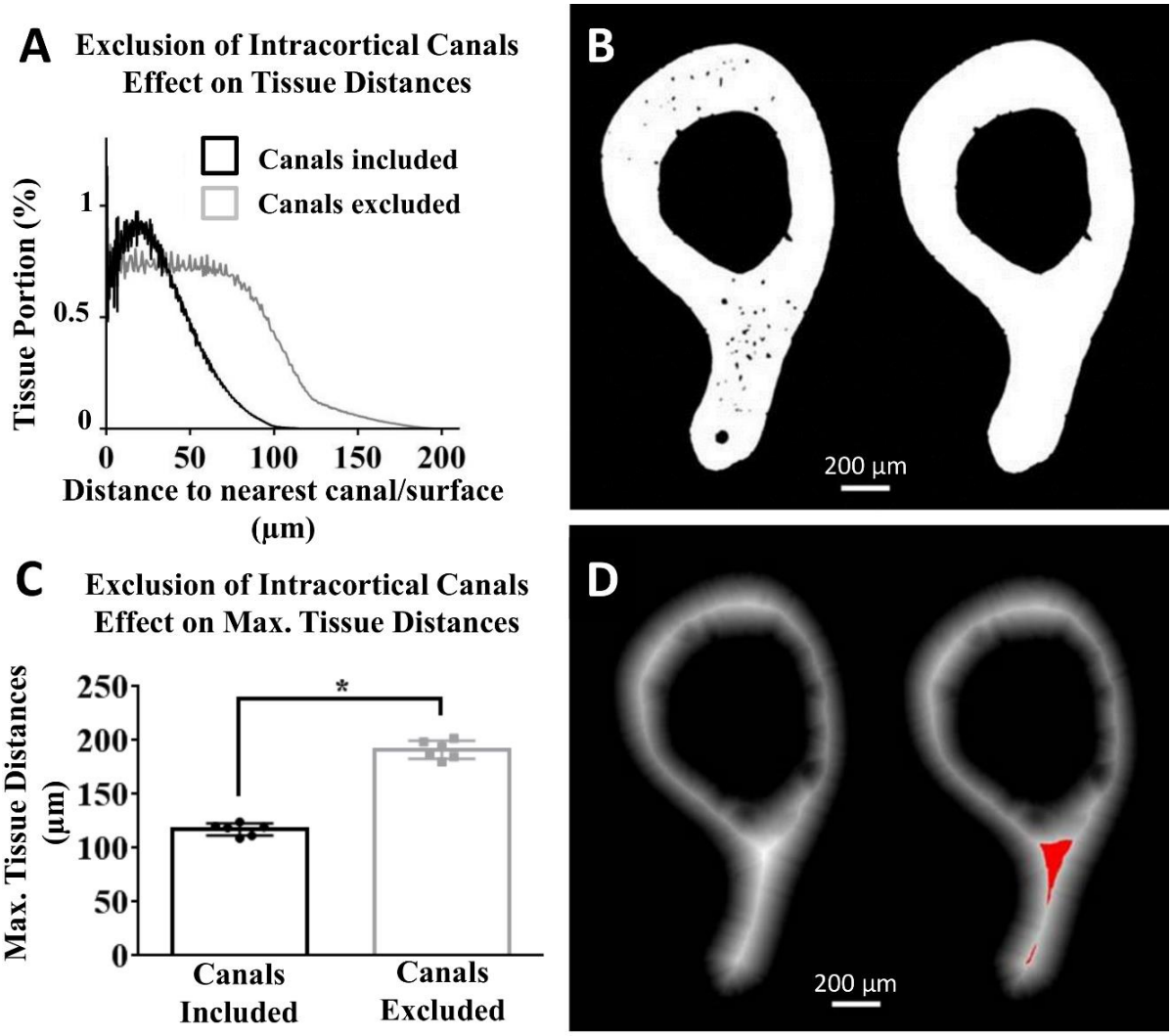

Figure 4.2. Effect of the exclusion of intracortical canals in the distance analysis for young subjects. Tissue distance distribution to nearest bone surface in the presence and absence of intracortical canals (A). Binarised cross-section with intracortical canals (left) and excluded canals (right) (B). Comparison of distance distribution maximums (C). 2D slice of 3D distance transform on mask (left) and identification of altered distance in the posterior region in red colour (right) (D). Error bars indicate mean value ± standard deviation, n=6 mice.*$p<0.05$.

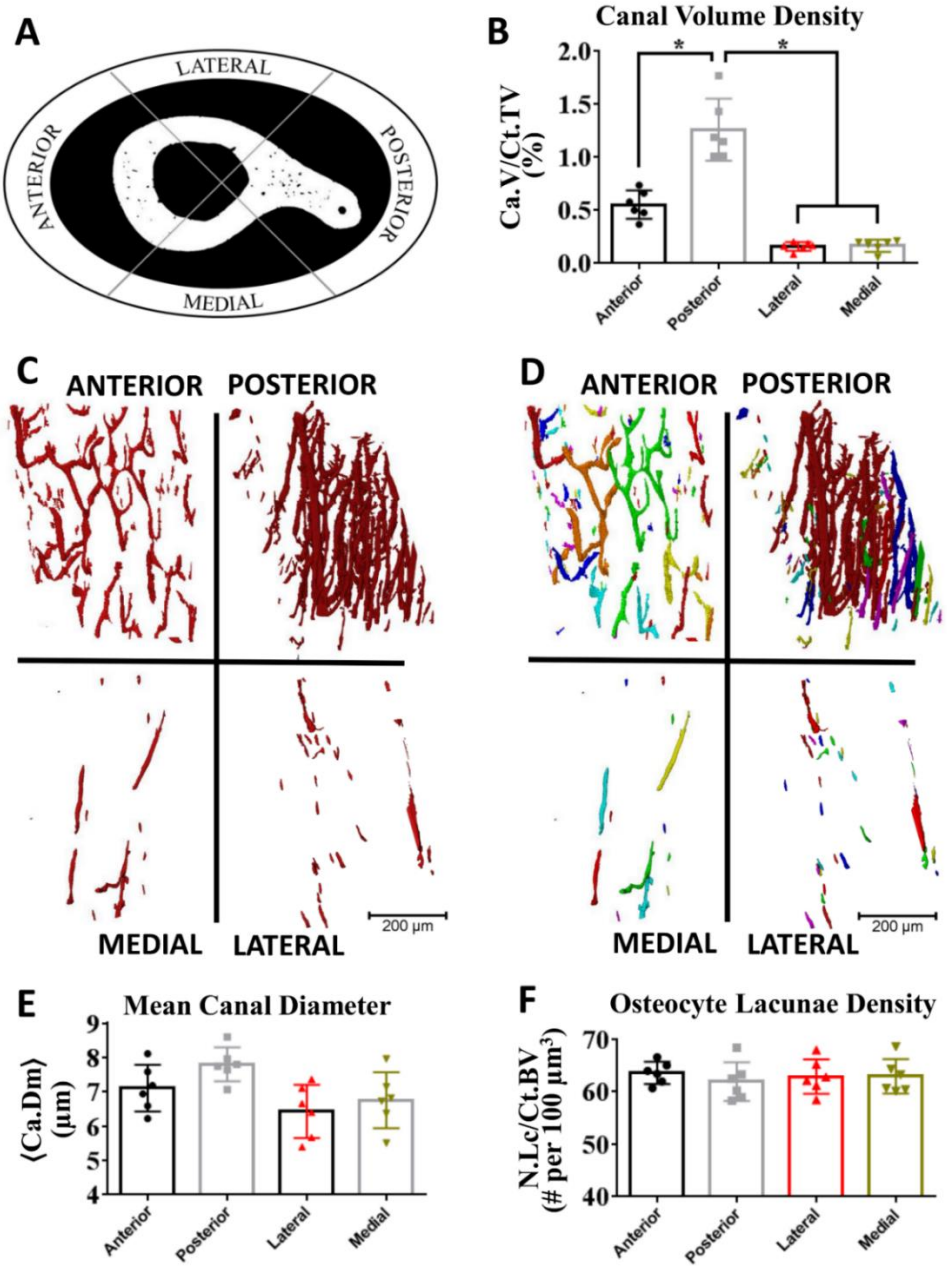

Figure 4.3. Results of the local analysis of microstructure on the young group. Intracortical canals in binarised slice and identification of anterior, posterior, lateral and medial quadrants on tibiofibular junction cross-section (A). Canal volume density (B), 3D rendering of intracortical canals in anterior, posterior, lateral and medial regions of a young subject (C), 3D rendering of the labelling of the canal structures in anterior, posterior, lateral and medial regions of a young subject where different colours stand for different canal structures (D). Mean canal diameter (E) and osteocyte lacunae density (F) in the 4 regions. Error bars indicate mean value ± standard deviation, n=6 mice. *p<0.05.

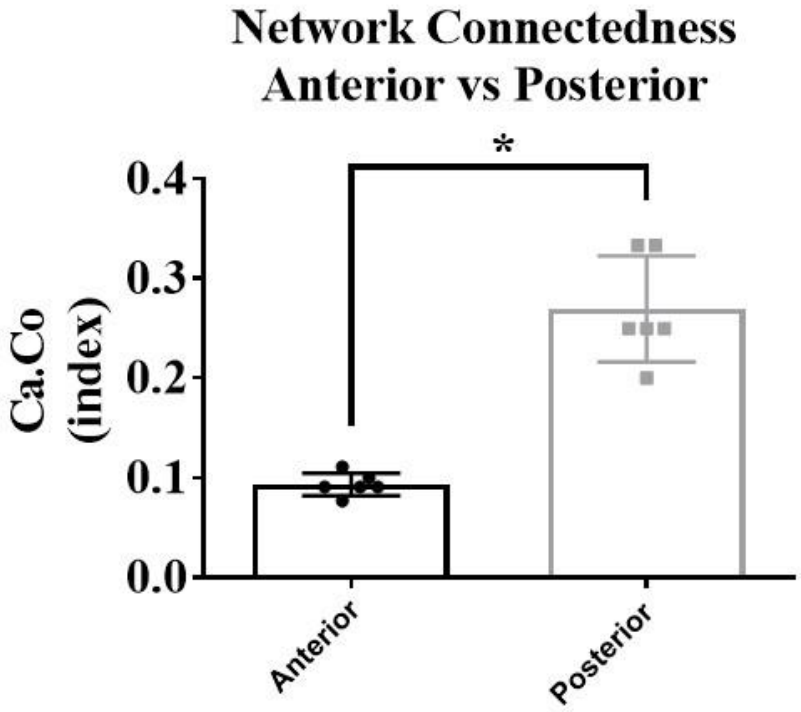

Figure 4.4. Results of network connectedness analysis in anterior and posterior regions of the tibiofibular junction. Error bars indicate mean value ± standard deviation, n=6 mice. *p<0.05.

To evaluate whether age exerts differential effects on the local distribution of intracortical vascular canals, analyses were undertaken specifically in the in the four cortical quadrants and compared. This revealed that there was no significant age-related variation in canal volume density in the anterior, lateral and medial regions whereas the posterior region exhibited a significant reduction in 10 month-old mice (p=0.002; Fig. 4.9A/B/C). No

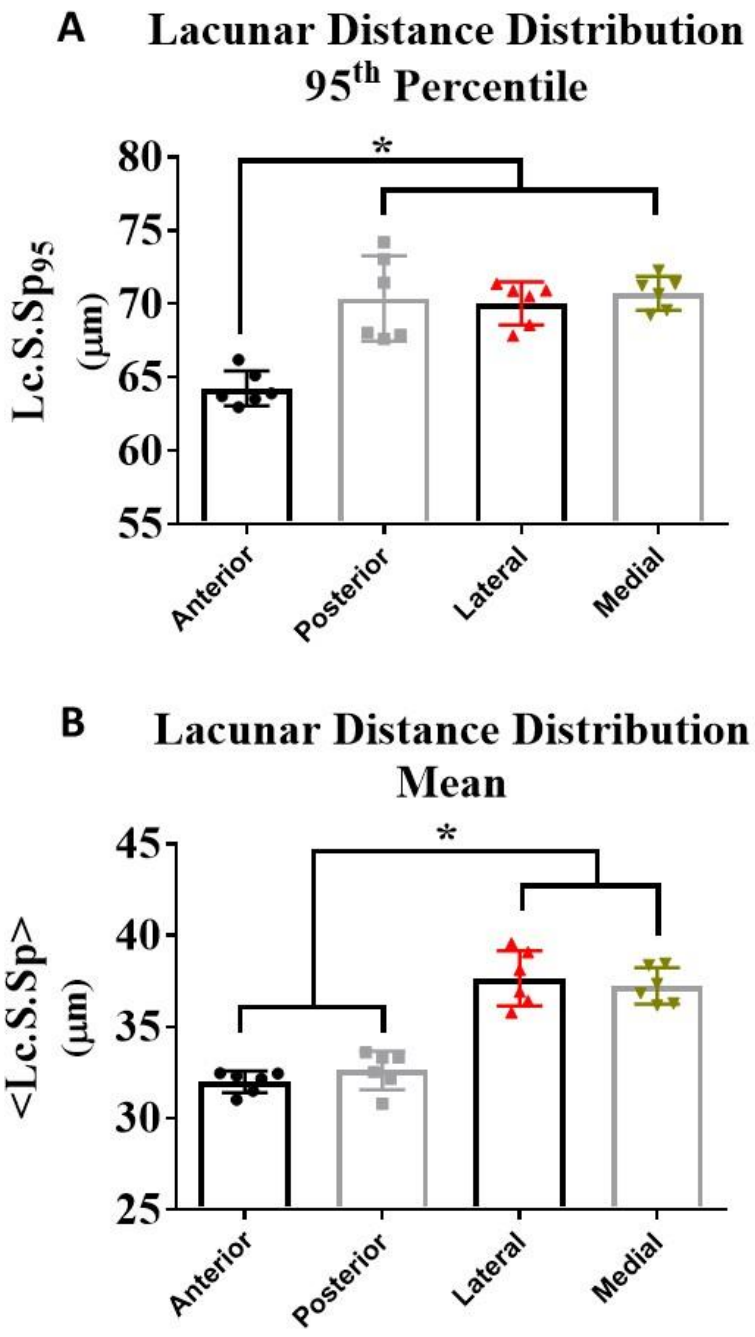

Figure 4.5. Results of the local distance analysis. 95th percentile of lacunar distance distribution (A) and mean value (B).

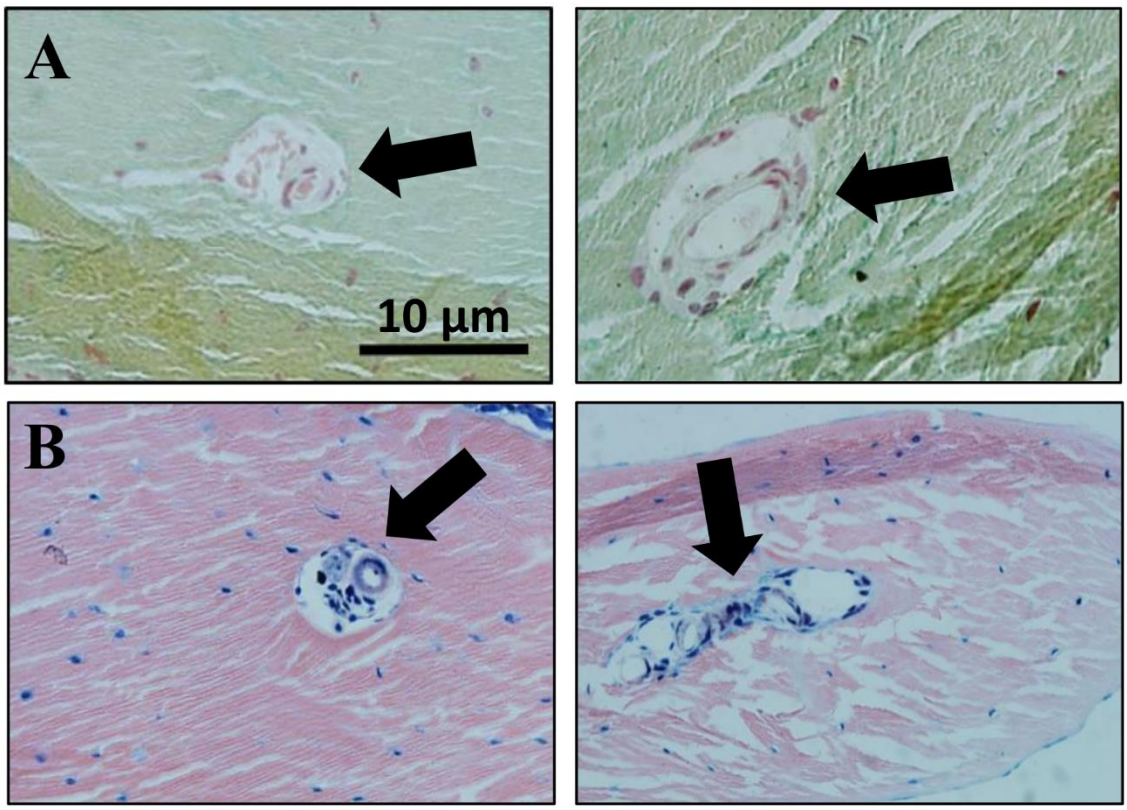

Figure 4.6. Histological examination of the calcified tibiofibular junctions. Pentachrome (A) and Giemsa (B) stainings. Arrows indicating blood vessels. n=9 (3 subjects, 3 sections analysed per subject).

significant changes in mean canal diameter were found in any regions with age (p=0.495; Figure 4.10A). Lacunar number density was not significantly different in either regions (p=0.340; Figure 4.10B) with age. Analysis of lacunar distances from bone surfaces showed that osteocytes are embedded significantly further into the mineralised tissue and getting significantly more distant from the vasculature in the posterior region for older 10 month-old mice (+13.99%, p=0.002 for distance mean, Fig. 4.10C; and +15.05%, p=0.004 for 95th percentile of distances, Fig. 4.10D). The opposite effect is observed in the other three quadrants, where lacunae were found to be located closer to bone surfaces and blood vessels in average (Fig. 4.10C/D due to the thinning of the cortex).

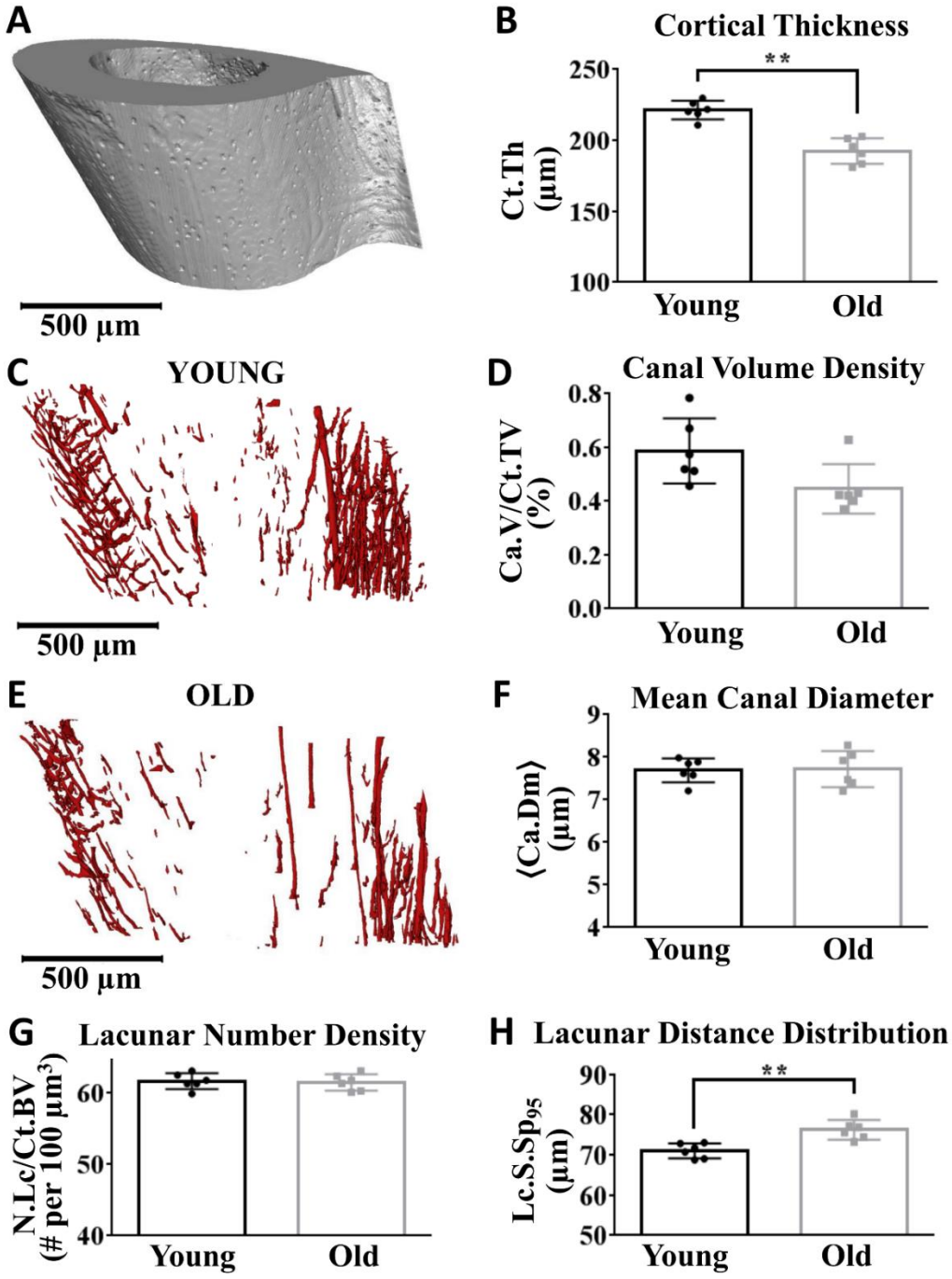

Figure 4.7. Results of the analysis of the undivided tibiofibular junction on the young and old groups. 3D rendering of the analysed region (A), average cortical thickness (B), 3D renderings of the intracortical vascular canals in a young (C) and old (E) mouse, canal volume density (D), mean canal diameter (F), osteocyte lacunar number density (G) and 95th percentile of lacunar distance distribution (H) to nearest intracortical canal or bone surface. Error bars indicate mean value ± standard deviation, n=6 mice for both age groups. **p<0.01.

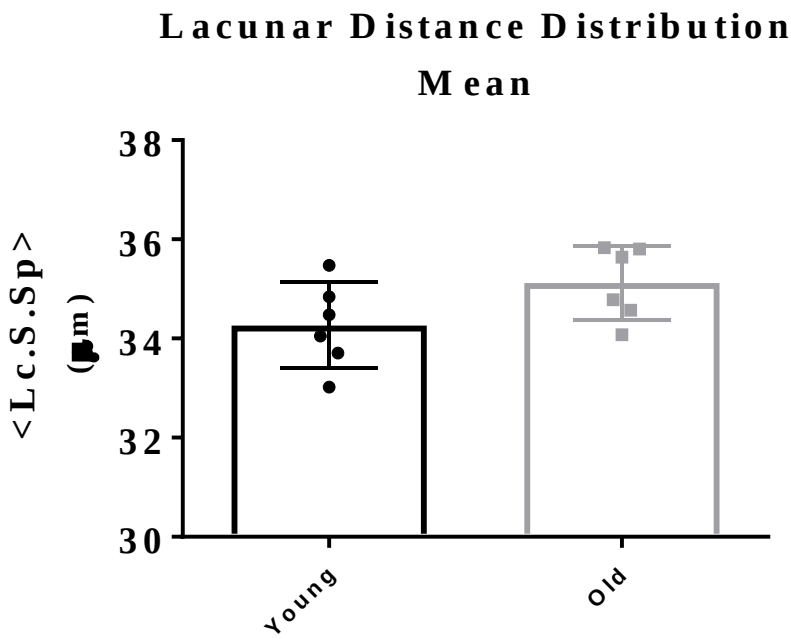

Figure 4.8. Osteocyte lacunar distance distribution to nearest intracortical canal or bone surface. Error bars indicate mean value ± standard deviation, n=6 mice for both age groups.

Microscopic analysis of calcified bone sections stained with either Pentachrome or Giemsa revealed the presence of blood vessels demonstrating that canals identified by SR CT in both age groups contained vascular channels. Upon further analysis, % canal occupancy was not altered with age (Figure 4.11) with values between 80 and 100% counted.

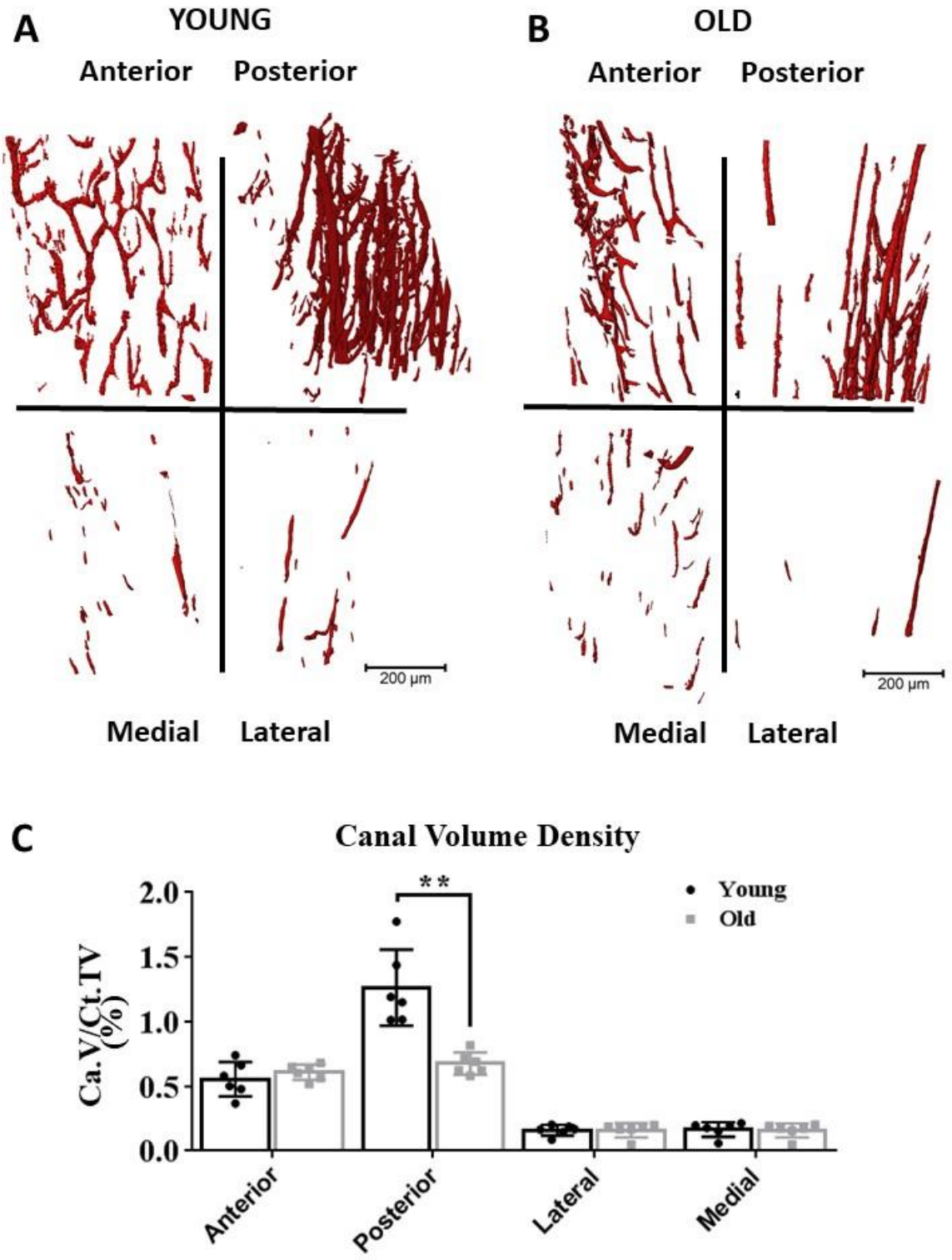

Figure 4.9. Results of the local analysis on the young and old groups. 3D rendering of intracortical vascular canals in a young (A) and old (B) subject. Results (C) are canal volume density for anterior, posterior, lateral and medial regions of the young and old groups. Error bars indicate mean value ± standard deviation, n=6 mice for both age groups. **p<0.01.

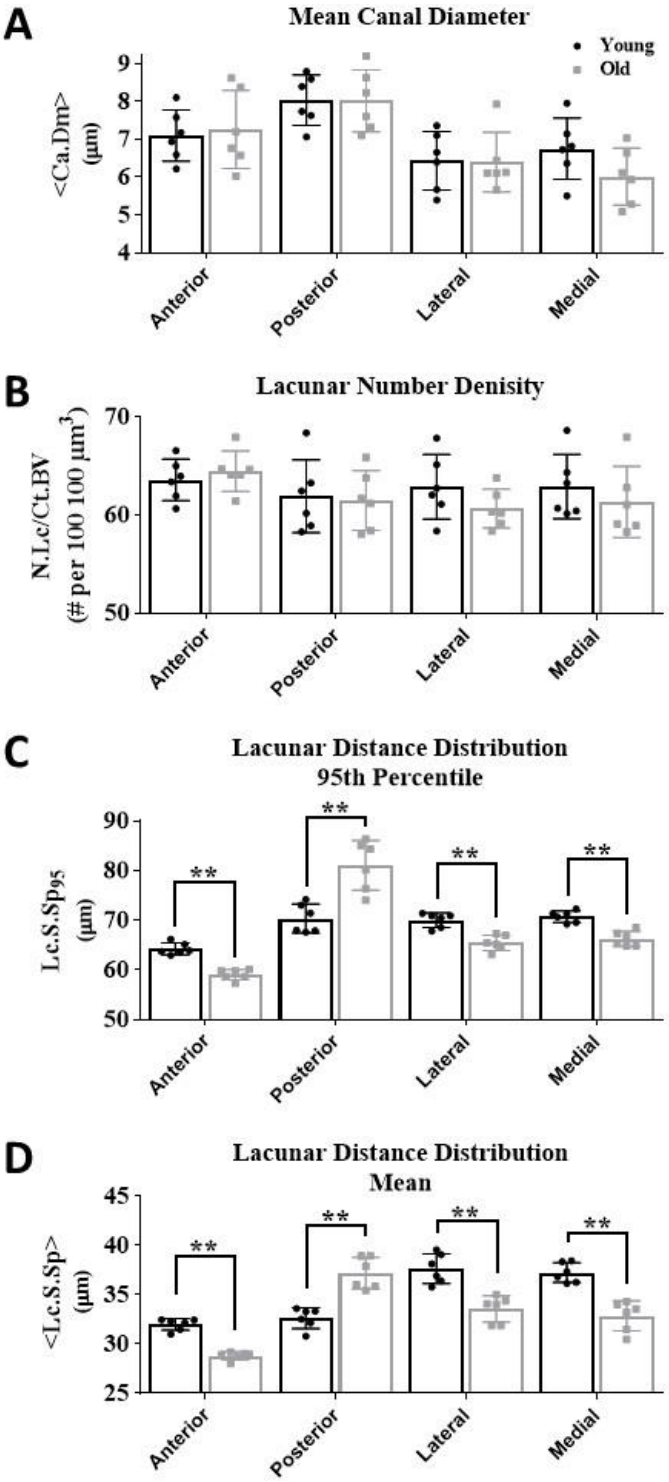

Figure 4.10. Results of the local analysis on the young and old groups. Mean canal diameter (A), osteocyte lacunar number density (B), osteocyte lacunar distance distributions to nearest bone surface, 95th percentile (C) and mean value (D) for anterior, posterior, lateral and medial regions of the young and old groups. Error bars indicate mean value ± standard deviation, n=6 mice for both age groups. **p<0.01.

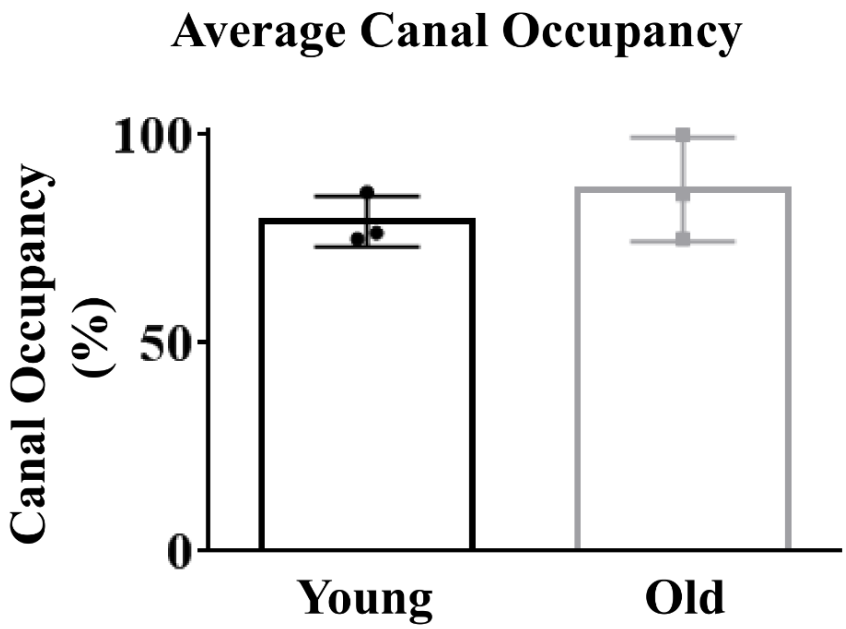

Figure 4.11. Histological examination of the tibiofibular junction. Quantification of canal occupancy for young and old groups. Error bars indicate mean value ± standard deviation, n=9 (3 biological replicates x 3 histological sections analysed per subject for both age groups).

4.4 Discussion

Results in this chapter report heterogeneity in the distribution of vascular structures within the murine tibiofibular junction. In particular, it was observed that the lateral and medial quadrants were lowly vascularised, which could have a biomechanical explanation. Indeed it has been shown by Prasad and colleagues (Prasad et al., 2010) that the strain environment of the murine tibia arises primarily due to bending with peak tensile and compressive strain values located at the anterior and posterior regions during locomotion, respectively. The lateral and medial regions of the cortex experience minimal strain magnitude due to their proximity to the neutral axis of bending during habitual use. This could therefore explain why the anterior quadrant is more vascularised compared to the lateral and medial compartments, even though the three regions present similar local

cortical thicknesses (~ 200 µm) and thus, osteocyte cells in these locations are equally close to endosteal and periosteal surfaces.

It was also evident that the posterior region of the tibiofibular junction was more highly vascularised than the anterior compartment. The analysis of the connectedness of the two vascular networks also revealed that they were topological differences in the arrangement of blood vessels. In particular, the posterior network had more numbers of connections and was orientated longitudinally. The analysis of distances highlighted the differences between vascular networks in anterior and posterior compartments. In particular, the analysis with the exclusions of canals showed that distances to the nearest bone surface (source of blood) increased dramatically in the posterior region when intracortical canals were removed from the analysis while the canals in the anterior region seemed to not to have an impact in these distances. It could be speculated that the clear structural differences in the vascular canal network which appear specific to their locality are suggestive of vascular heterogeneity.

A clear structural difference between the human and murine skeleton is that mice lack obvious osteonal or Haversian vascular canals, in cortical bone. In mice the function of the intracortical canals is therefore less clear. A secondary idea arises from the similarities between the osteocyte distance distributions presented here for the murine tibiofibular junction and results found in humans (Hannah et al., 2010). This finding suggests that the osteocyte distribution and proximity survival threshold could be common for mouse and human. Furthermore, previous histological observations of the diameter of osteonal structures (Ham, 1952; Ham, 1953; Joseph P. Weinmann, 1955) have established the maximum transport distance for nutrients to be 100 µm in humans. Since the bones of mice and humans are made of the same basic material, the proximity survival threshold of around the 100 µm may be strictly defined by the physics of the diffusion processes. Thus, this spacing would assure a sufficient transport of oxygen, nutrients and waste products to support and maintain viable tissue. This could lead to hypothesise that there is no need of intracortical vessels for osteocyte cell nutrition when the cortical thickness is thin (< 200 µm) and guarantees sufficient tissue diffusion. This could explain why Haversian canals are rare in mice. In larger cortices, there is a need of an intracortical supply to facilitate diffusion and longitudinal irrigation system is the optimal solution to reduce distances

between endosteal and periosteal surfaces explaining the existence of Haversian canals in bigger animals. Figure 4.12 illustrates this idea. However, the study described in this chapter has reported that there are areas deep inside the mineralised tissue of the thicker posterior compartment of the tibia that could be dramatically affected without the intracortical vessels, in terms of osteocyte proximity to blood supply and survival. Interestingly, the majority of these posterior vessels also run longitudinally in the bone (in contrast to the anterior region) and thus appear to have potential similarities in structure to Haversian canals in larger mammals (Figure 4.13). This may mean that there are regions of the mouse skeleton, deep inside the mineralised tissue, were nutrition would be poor without the existence of intracortical canals. The observed longitudinal canal in the thicker posterior region could function as Haversian canals and it could be speculated that there are different types of blood vessels within bone tissue. In fact, recent findings on a landmark publication supported the notion of different types of vessels in bone demonstrating that capillaries in bone are functionally specialised and heterogeneous (Kusumbe et al., 2014). Taken together, all this could suggest that: 1) The longitudinal vessels in the thicker posterior region function as irrigation system that perfuses the tissue between endosteal and periosteal surfaces to maintain tissue nutrition and viability; and 2) the vasculature within the thinner, anterior region may not be required for tissue nutrition but may have an alternative function for example in providing a mechanism for repair within this mechanically active region of the cortex prone to fatigue damage.

Due to the impossibility to visualise soft tissue structures with CT, histological examination was necessary to confirm that canal structures perforating the cortex are indeed, the living space of the vasculature. Although only 80% of the canal structures were found to be filled with blood vessel, the reliability of this quantification could be questioned due the 2D nature of histology and the distortion, tearing and folding that the tissue usually experiences. Recurring to a truly 3D method for the visualisation of the soft tissue comprising the cortical vasculature could make this quantification more accurate as it will be discussed in Chapter 6.

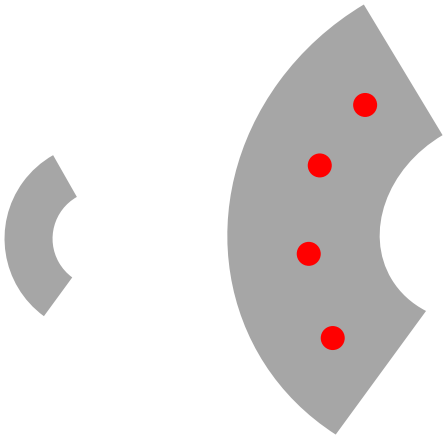

Thin cortex (e.g. mouse)

Thick cortex (e.g. human)

Figure 4.12. Thin cortices in small animals do not need intracortical nutrition whereas thick cortices in larger animals need a longitudinal irrigation system (red circles) to reduce distances between endosteal and periosteal surfaces.

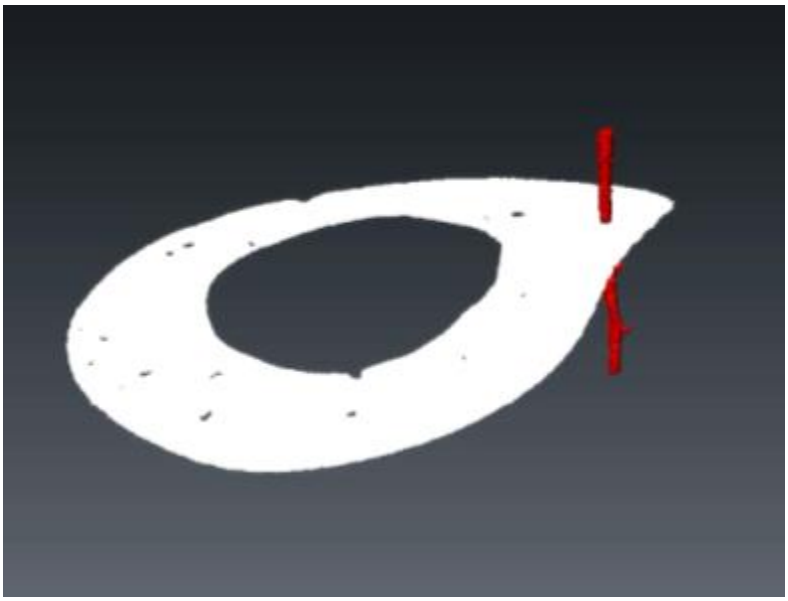

Figure 4.13. Identification of longitudinal canal (red) in the thick posterior region of the cortex.

The study described in this chapter evaluated the effect of age on the 3D distribution of intracortical vascular canals and osteocyte lacunae in the murine tibiofibular junction using non-invasive high resolution imaging. Specifically, it has been now shown that 1) there is an age-related thinning of the cortex that seems not to be accompanied by an reduction in vascular density when the undivided cortices where analysed; 2) the posterior region, which is highly vascularised at 15 weeks of age, exhibits a reduction in vascular canal density with age that makes osteocyte lacunae within this region to be farther located from the nearest bone surface (source of blood); 3) vascular canals are equally filled with blood vessels at 15 weeks and 10 months of age.

It is important to highlight that the presented measurements of reduced cortical porosity in the posterior region with age only account for the volume of vascular canals and not osteocyte lacunae. In contrast, previous studies have actually reported increase in porosity with ageing in various mouse strains (Courtland et al., 2013; Ferguson et al., 2003; Javaheri et al., 2015; Silbermann et al., 1987; Weiss et al., 1991) when the cortex was divided for analysis. It should also be noted that the 10-month-old animals were younger than the mice use in other studies, thus, severe signs of advanced bone deterioration have not been observed. What it is important to highlight is that early and clear reductions in the intracortical vasculature have been observed at this early stage and it could be speculated that such early vascular alterations may initiate later bone changes. The findings of reductions in vascular density with age are consistent with previous investigations using rodents (Dinenno et al., 1999) where it was showed that that limb blood flow and vascular conductance are reduced with age. Furthermore, other studies have reported a reduced vascularisation of the bone marrow in the tibial metaphysis of rats (Mekraldi et al., 2003) and mice (Ding et al., 2011; Roche et al., 2012) using ovariectomy as a model for postmenopausal osteoporosis.

The observations of the lack of mean difference in canal diameter between age groups combined with the reduction in canal volume density in the posterior region suggests a reduction in canals with age. Mice do not undergo secondary remodelling, therefore in contrast with ageing in humans it could be predicted that at this particular site

the blood vessels may regress with age and the canal spaces fill with mineral. The composition of such filled canals has never been studied in mice, but future analyses of the intracortical microstructure in the posterior region with age in conjunction with measurements of bone mechanics could provide new insights around the bone quality at this site.

Recently, in a landmark publication, it has been demonstrated that blood vessels associated with trabecular bone are functionally specialised and heterogeneous (Kusumbe et al., 2014). Specifically, the authors of this study were able to subdivide capillaries in bone into two subtypes termed type H and type L dependent upon CD31 or endomucin expression, location and interaction with osteogenic cells. Interestingly, while the total number of endothelial cells associated with the bone marrow cavity was not significantly different in juvenile, in adult and aged mice type H declines after adolescence which the authors suggested could contribute to the well-known loss of osteogenic capacity and bone mass with ageing. This alteration in the vasculature is consistent with our observations of a reduction in vascular canals only in the posterior region with age. Kusumbe et al (Kusumbe et al., 2014) reported that this reduction could be rescued by the activation of Notch signalling by the vasculature in their experiments. Whether these vessel subtypes or indeed Notch are regulated in a similar manner in the cortical vasculature of mice has not yet been investigated, but is an exciting area for future research. It is well established that the vascular endothelium is metabolically active and plays a critical role in many physiological processes and it is also recognised that the endothelium is involved in most, if not all, disease states. However, there exists a wide bench-to-bedside gap in endothelial biomedicine and an even wider void in targeting the vasculature clinically for treatment of degenerative bone disease or fracture repair. Site-specific endothelial phenotypes are thought to be initiated and maintained by signals residing in the extracellular environment, which can be biochemical or biomechanical. Osteoblasts and osteocytes undoubtedly communicate with the endothelium and a potential role for them in driving endothelial cell heterogeneity warrants further investigation. Furthermore, recent articles have now linked the role of the vasculature to osteoporosis (Clarkin and Gerstenfeld, 2013; Liu et al., 2012).

It is important to highlight however, that the observed structural changes in the posterior region of the murine tibiofibular cortex could be accompanied by regional

differences in the milieu making up the four quadrants. Environmental differences exist between the regions of the cortex including mechanical strain and fluid flow which could directly impact the cells of the vasculature and contribute to the different blood vessel structures identified in this study. Indeed, osteoblasts are known to release mitogens to communicate directly with blood vessels including VEGF. The mechanical environment has been show to influence VEGF release by osteoblasts in vitro (Clarkin and Gerstenfeld, 2013) and it could be speculated that osteoblasts present within different regions of the tibiofibular junction may alter their production of VEGF in response to environmental factors which could result in distinct blood vessel structures being present dependant on their location.

In summary, the studies described within this chapter identify a site of the murine skeleton where the connection between vasculature and cortical bone can be specifically interrogated. Using this skeletal site, an age-related recession in the intracortical vasculature was found. Chapter 5 will make used of the methodology developed in Chapter 3 to explore cortical microstructure in a transgenic animal lacking the proangiogenic signal VEGF.

Chapter 5: Effect of the osteoblast-specific VEGF deletion on the cortical microstructure of the tibiofibular junction

5.1 Introduction

The results from several studies have shown that reduced VEGF expression can be linked to the ageing of multiple cell types (Efimenko et al., 2011; Jiang et al., 2008; Pola et al., 2004; Rivard et al., 1999; Wilson et al., 2010) and reduced levels of circulating VEGF have been found in postmenopausal women (Senel et al., 2013). Thus, the age-related changes in the intracortical vasculature observed in Chapter 4 could be driven by decreased expression of proangiogenic signals. Mice with conditional VEGF deficiency in osteoblastic precursor cells have been reported to exhibit an osteoporosis-like phenotype characterized by reduced bone mass and increased bone marrow fat (Liu et al., 2012). However, cortical microstructure in bone lacking VEGF has not been assessed to date. The aim of this chapter was to extend the use of the previously developed methodology and apply it to explore changes in the cortical microstructure, in bone where VEGF has been deleted from osteoblasts. Transgenic animals with bones lacking VEGF were imaged and analysed to detect the mineralised tissue and extract cortical porosity. Comparison with WT animals revealed microstructural changes in cortical bone.

5.2 Methodology

5.2.1 Osteoblast-specific deletion of VEGF

Conventional gene deletions (gene inactivated in all tissues) can lead to embryonic lethality when the gene is crucial during development. This is the case of VEGF. Conditional knockout models allow tissue-specific and inducible gene deletions that can circumvent lethality. The Cre-lox system, derived from P1 bacteriophage, is a potent and specific system for controlling gene expression and generate conditional knockouts. When cells that have loxP sites in their genome express Cre, a recombination event can occur between the loxP sites. LoxP stands for locus of X(cross)-over in P1 bacteriophage and are 34 bp sites with directionality. Cre stands for cyclisation recombinase in P1 bacteriophage and it is a

protein that can catalyse the recombination of DNA between loxP sites. The location and orientation of the loxP sites determines how the genetic material will be rearranged. Gene deletion takes place if the loxP sites face in the same direction. Floxed genes (flanked by loxP; notation: [gene]^{fl}) are a pre-requisite for recombination in the presence of Cre (Zhang et al., 2007). Cre-lox breeding was used to generate VEGF conditional knockout mice for the experiments included in this chapter.

Second generation VEGF knockout mice (referred to here as VEGF Ocn Cre KO) were bred and used to investigate the effect of VEGF deletion on the cortical microstructure of the tibiofibular junction. For VEGF deletion in mature osteoblasts, mice carrying floxed alleles of VEGF (VEGF$^{fl/fl}$, obtained from Genentech, courtesy of Napoleone Ferrara and Bjorn Olsen) and expressing Cre recombinase under the control of the Osteocalcin promoter (Ocn Cre, purchased from The Jackson Laboratory, US) were used. Primarily, a hemizygous OCN Cre mouse was mated with a homozygous VEGF$^{fl/fl}$. The first generation mice produced by this breeding pair have a singular allele of Ocn Cre, enabling the production of transgenic offspring. Second generation mice are produced by breeding first generation mice back to VEGF $^{fl/fl}$ mice as showed in Figure 5.1. The second generation offspring was then left to develop, until reaching one year of age.

5.2.2 Genotyping

After culling the animals using schedule 1 cervical dislocation, a small extract of tail from each animal was snap frozen and stored at -80 degrees until required. This tissue, containing a small fragment of bone within it, was used for the genotyping for all animals. The tail fragments were digested and genomic DNA was extracted, using the Qiagen DNeasy Blood and Tissue Kit, according to the protocol provided by the manufacturers.

Cre forwards (5'-CAAATAGCCCTGGCAGATTC-3') and Cre reverse (5'-TGATACAAGGGACATCTTCC-3') primers were used in the PCR mix to determine which samples were Cre positive and which samples were Cre negative. A 18 ul volume of PCR mix and 2 ul volume of extracted DNA was combined. A negative control was run for each gel, where the 2ul volume of DNA was replaced with 2 ul water. If the sample was Cre

positive, a band was present at 411bp on the 1.5% agarose gel (Figure 5.2). Any samples without a visible white band are considered Cre negative and are not tested further.

The samples which were Cre positive were separated and underwent a second round of genotyping to determine whether they heterozygous or homozygous VEGF Ocn Cre strains. The forwards and reverse oligonucleotide VEGF primers muVEGF 419.F (5'-CCTGGCCCTCAAGTACACCTT-3') and muVEGF 567.R (5'-TCCGTACGACGCATTTCTAG-3') were used in a PCR reaction with DNA extracted from tail tips to determine the presence of the floxed VEGF gene. The PCR product was ran on a 2% agarose gel. Mutant homozygous mice have one band only, visible at 148 bp (Figure 5.3). Heterozygote shows one band at 100 bp and one band at 124 bp below.

5.2.3 Synchrotron-based micro-CT of transgenic bones

The tibiofibular junctions of 1 year old (n=5) VEGF Ocn KO and 1 year old (n=5) WT C57BL/6 female mice were scanned using SR CT at the TOMCAT beamline of the Swiss Light Source at a voxel size of 0.65 µm and datasets analysed to extract porosity as described in Chapter 3. The parameter cortical porosity is defined as cortical tissue volume dived by volume of cortical porosity.

5.2.4 Mechanical testing of murine femora

Right femoral bones from 1-year old (n=5) VEGF Ocn KO and 1-year old (n=5) WT C57BL/6 female mice (animals whose tibiofibular junctions were imaged) were mechanically loaded until fracture using the three-point-bending configuration to measure stiffness. To do this, bone samples were collected free from soft tissue and stored at -80 °C in the facilities of Southampton General Hospital. Bone samples were then shipped to Vienna University of Technology in dry ice for mechanical tests. Femoral bones were defrosted and notched using a Buehler IsoMet low speed saw and notch sharpened with a

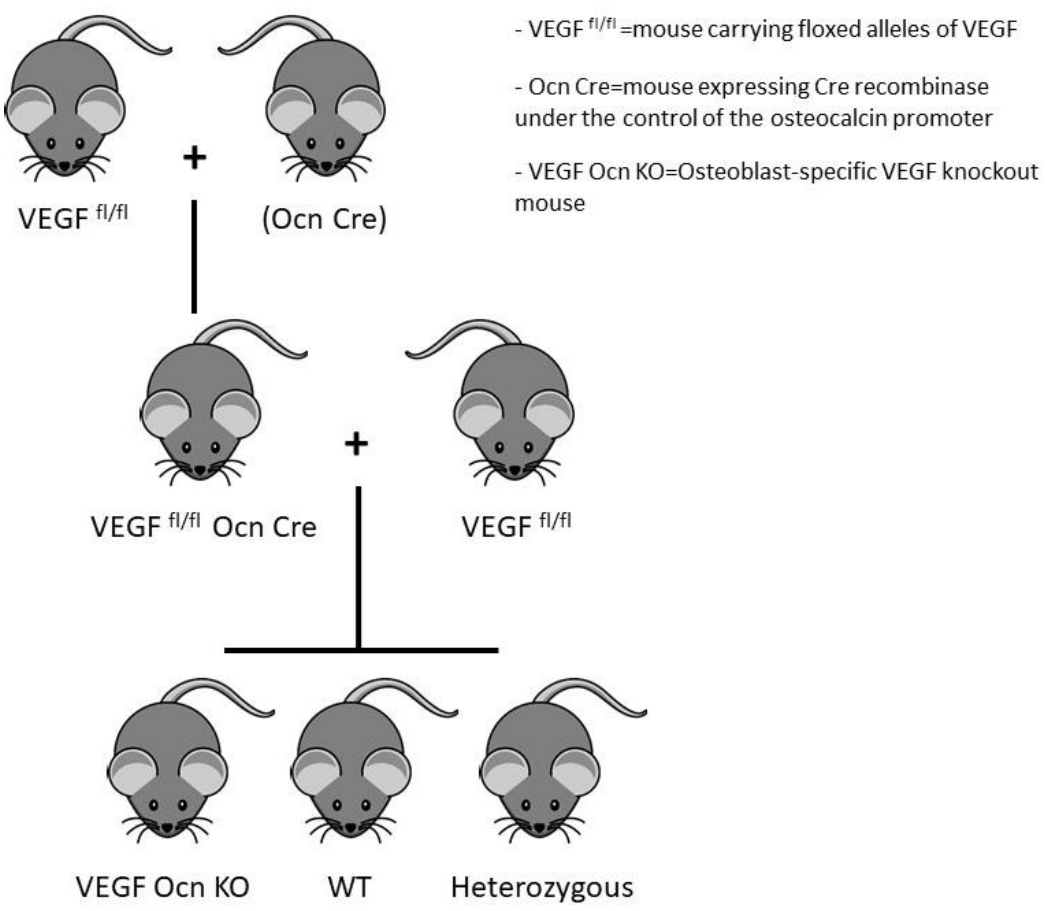

Figure 5.1. Generation of osteoblast-specific VEGF knockout mice.

Figure 5.2. First round of genotyping: Identification of Cre positive and wild type samples. Bands present at 411 bp are Cre positive. The wild type samples have no band visible. Tail tip tissue. [Generated by Alice Goring, University of Southampton].

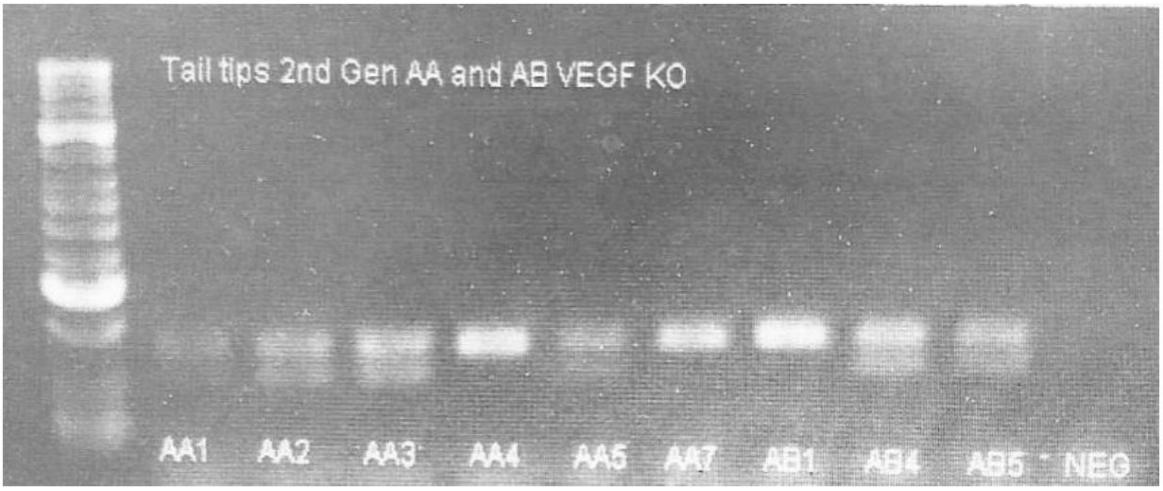

Figure 5.3. Second round of genotyping: Identification of mutants and heterozygotes. Subjects with one band are classified as VEGF Ocn Cre mice, in which VEGF has been knocked out specifically in osteoblast cells. Subjects with a double band are classified as heterozygotes, with the second band denoting the presence or absence of VEGF. Tail tip tissue. [Generated by Alice Goring, University of Southampton].

scalpel and 1-micrometre Buehler diamond suspension. Notched and sharpened femoral bones were mounted onto a Thelkin servo-electric load frame with a 10 Newtons load cell for testing. Three-point-bending tests were performed at a constant rate displacement on the notched femoral bones immersed in a bath of phosphate-buffered saline. Applied external force and caused bending displacement were recorded during the experiment. Stiffness (K) was computed as the ratio applied force/displacement during the elastic behaviour. Figure 5.4 shows the three-point bending set-up and images of the femoral bone at the beginning and end of the test.

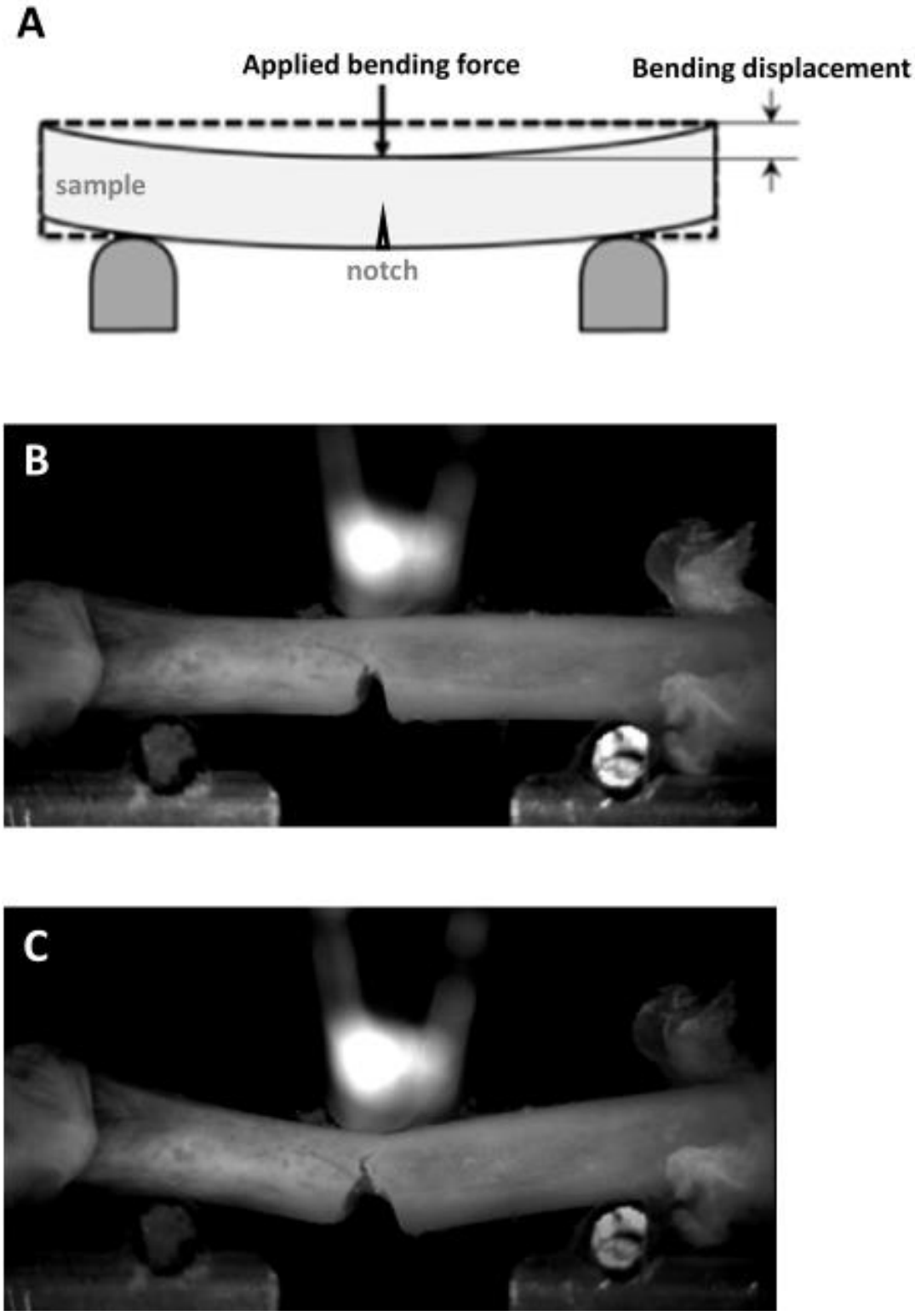

Figure 5.4. Three-point bending set-up for mechanical testing of murine femoral bones. Three-point bending set-up diagram (A), image of a notched murine femur at the beginning of the test (B) and image of a notched and broken murine femur at the end of the test (C).

5.3 Results

Figure 5.5 shows the CT images for a WT and a VEGF Ocn KO mouse. It was found that the 5 animals lacking VEGF presented areas of low mineralisation within the cortical bone.

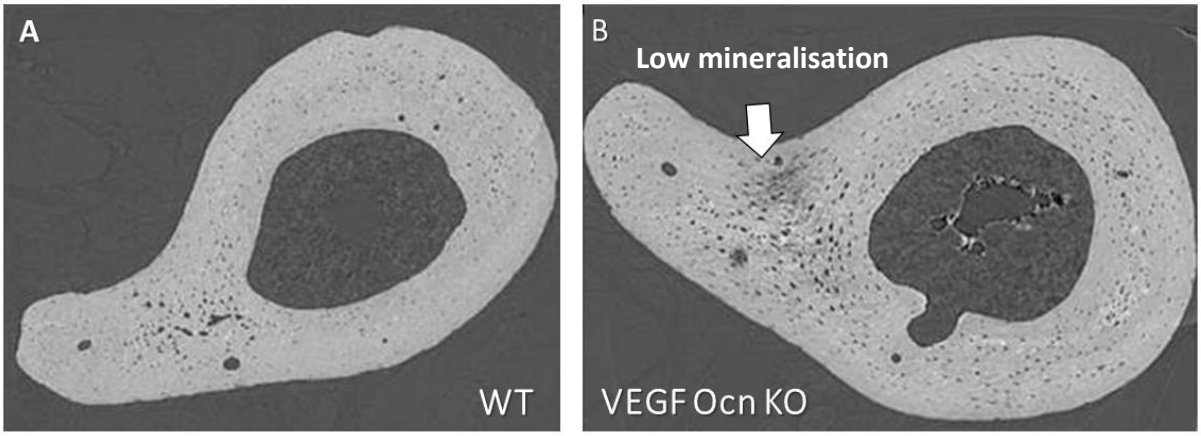

Figure 5.5. CT reconstructed slices for a WT (A) and a VEGF Ocn KO (B) 1 year old, second generation female mouse. Area with low mineralisation evident on the animal lacking VEGF and indicated with an arrow.

Cortical porosity was extracted from the 10 datasets as described in Chapter 3. However, vascular canals and osteocyte lacunae could not be separated for the VEGF Ocn KO. Figure 5.6 shows examples of 3D rendering of porosity objects in KO and WT animals. The disruption in the mineralisation of the matrix in transgenic animals made the detection of the cortical porosity complicated, providing porosity objects with altered shapes and sizes due to the regions of low mineralisation. As a result, osteocyte lacunae and vascular canals were misclassified due to the fact that lacunae seem enlarged and connected to each other and to vascular canals in the animals lacking VEGF. The impossibility to separate canal from lacunae forbade the computation of distances, vascular density, lacunae number density and canal diameter.

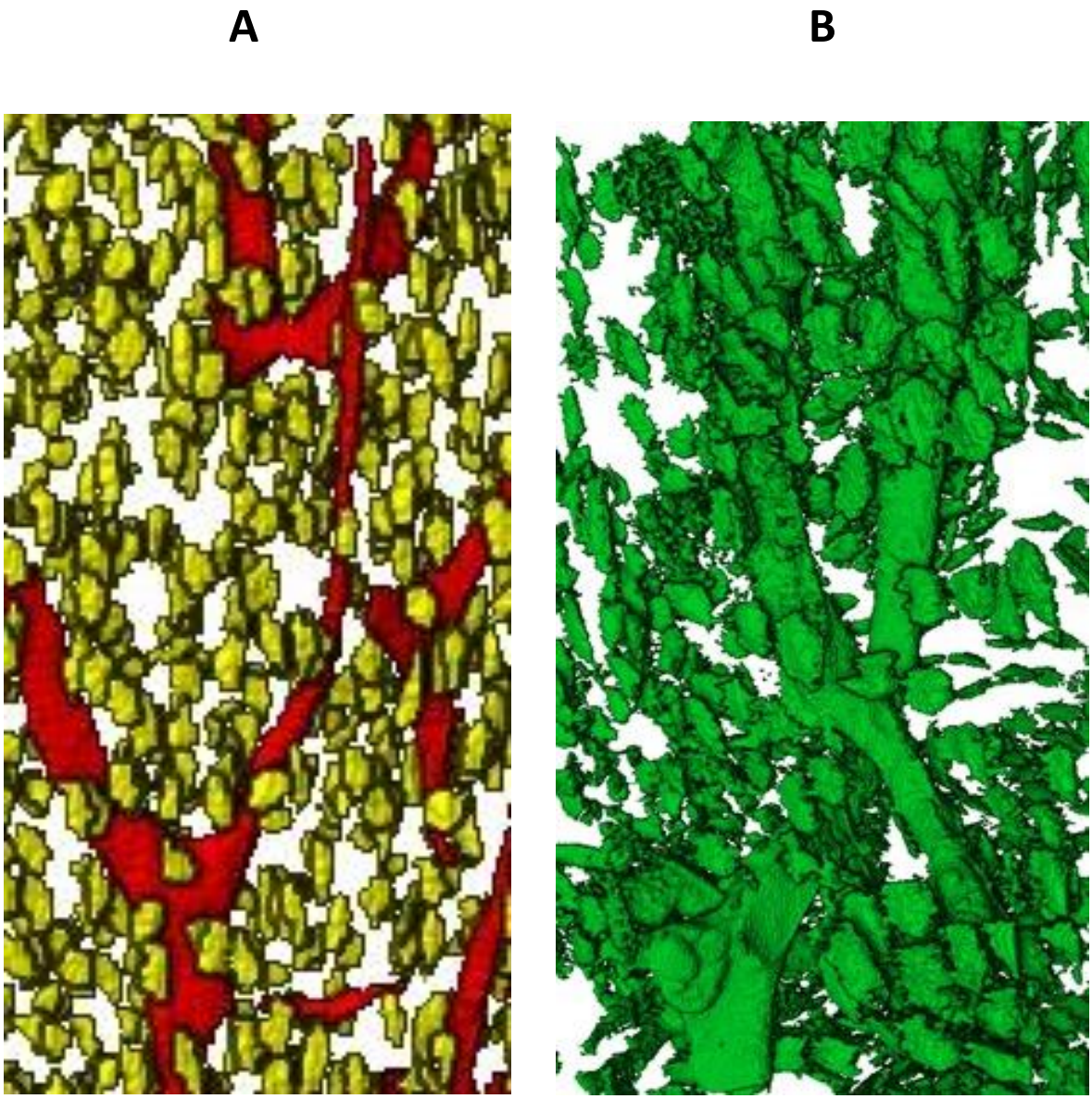

Figure 5.6. Separation of cortical porosity in WT and VEGF KO animals. Osteocyte lacunae (yellow) and cortical canals (red) can be separated in WT animals after porosity extraction following approach described in Chapter 3 (A). Cortical porosity is misclassified into one category (green) with canals and lacunae combined when the developed methodology is applied (B), this is due to areas of low mineralisation affecting pore shape and size.

Cortical porosity (including lacunae and canals) was quantified for WT and VEGF Ocn KO female animals. The results for the undivided cortex of the tibiofibular junction are showed in Figure 5.7. Porosity was increased for the animals lacking VEGF when compared

with WT (+39.917 %, *p*=0.008). The cortices were then divided into quadrants to analyse the local effect of the lack of VEGF on cortical microstructure. Figure 5.8 shows the results of this analysis. Anterior and posterior region suffered from an increase in cortical porosity in the KO mice (+41.235 % and +52.188 % respectively; *p*=0.008 for both regions). Increases in porosity were not statistically significant for lateral and medial quadrants (*p*=0.063 and *p*=0.095 respectively).

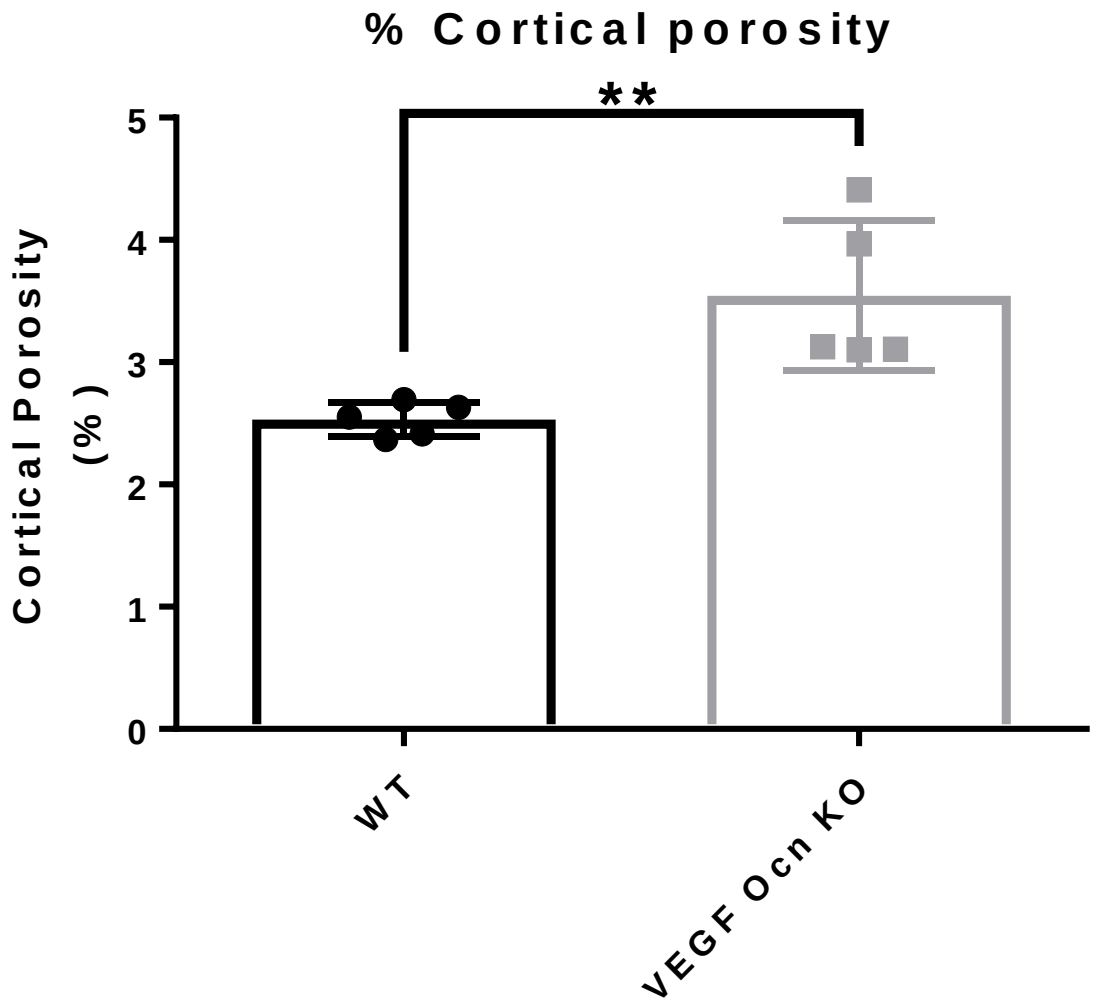

Figure 5.7. Cortical porosity in the tibiofibular junction of WT and VEGF Ocn KO mice. Error bars indicate mean value ± standard deviation, n=5 mice for WT and VEGF Ocn KO animals. **p<0.01.

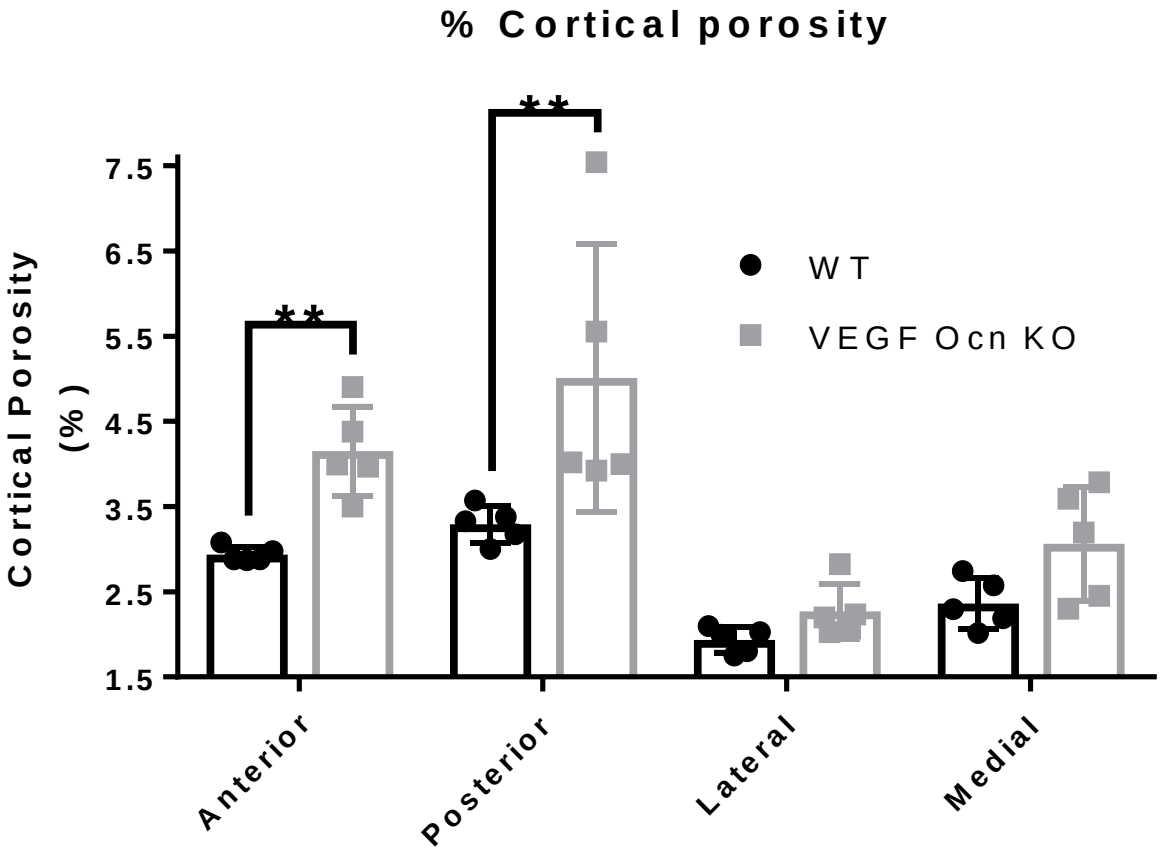

Figure 5.8. Cortical porosity in the anterior, posterior, lateral and medial quadrants of the tibiofibular junction for WT and VEGF Ocn KO mice. Error bars indicate mean value ± standard deviation, n=5 mice for WT and VEGF Ocn KO mice for each quadrant. **p<0.01.

Stiffness results from three-point-bending tests in WT and VEGF Ocn KO female animals are showed in Figure 5.9. Results were below the statistical significant level (p>0.05 but verging on), showing that femoral bones from mutant mice could have reduced stiffness when compared with WT animals (-26.406 %, p=0.056).

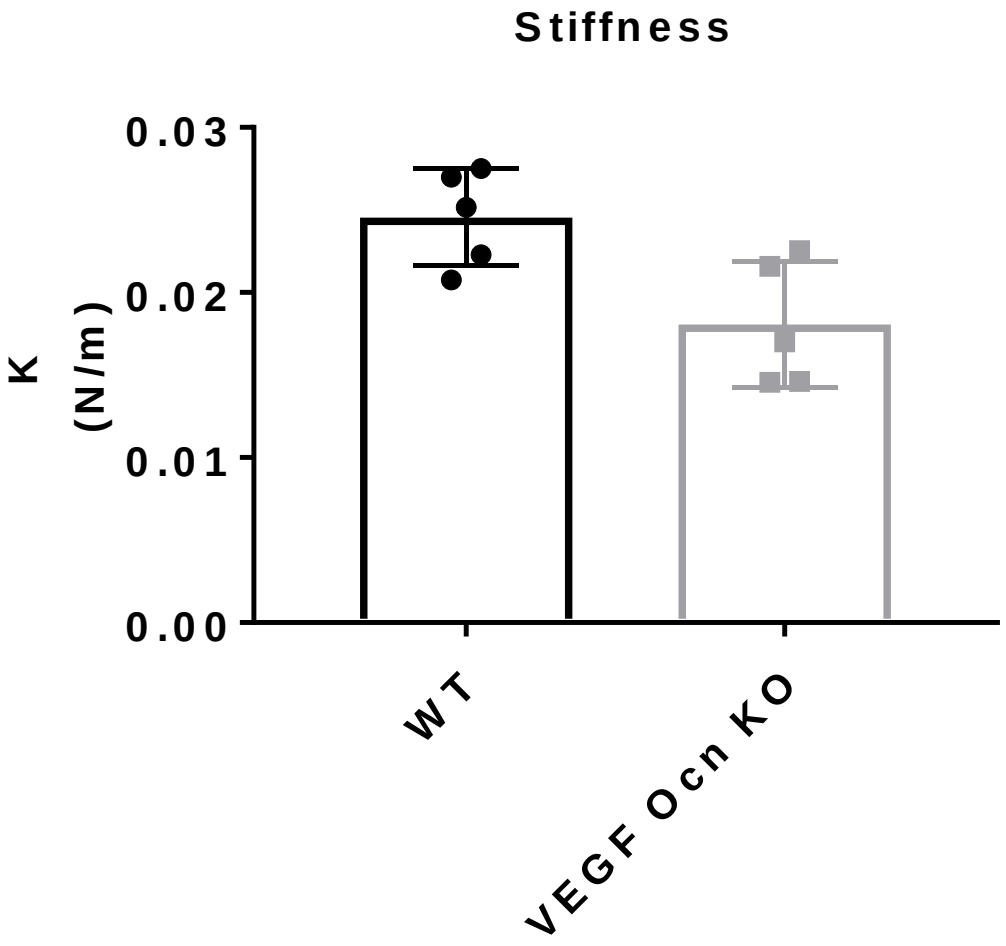

Figure 5.9. Stiffness in three-point bending for WT and VEGF Ocn KO femoral bones. Error bars indicate mean value ± standard deviation, n=5 mice for WT and VEGF Ocn KO animals (p=0.056).

5.4 Discussion

The results of this chapter show that the lack of VEGF resulted in increased cortical porosity measurements. These changes were taking place in the anterior and posterior regions where the vascular canals were found to be localised in Chapter 4. However, the transgenic animals presented a disrupted matrix with regions of low mineralisation. As a result, areas that have been identified as pores or cavities could also be non-mineralised

osteoid. The methodology developed in Chapter 3 for the extraction of cortical porosity and the assessment of age-related changes was optimised to deal with mineralised matrices and, for this reason, it failed to identify vascular canals and osteocyte lacunae in the transgenic mice. Standard (absorption based) CT itself can only detect the hard mineralised tissue and struggles to distinguish between osteoid and pores or cavities. As a result, the extracted porosity objects could have the wrong shape and size.

Results from mechanical testing (at the edge of statistical significance) suggest that mechanical properties of bone lacking VEGF could be different from WT. Increasing biological replicate number in future experiments could help to support this hypothesis.

To date, no other mechanics data nor intracortical porosity information on bone lacking VEGF are available in the scientific literature. Studies with animals lacking VEGF in bone are limited. Experiments with mice where VEGF was deleted in osterix (Osx) expressing cells (osteoblastic lineage) have been carried out (Hu and Olsen, 2016a; Liu et al., 2012). VEGF Osx KO animals in the literature presented reduced bone mass and thinner bones and delayed/impaired fracture healing when bones were imaged at a resolution that was insufficient to reveal information about the bone microstructure (porosity not evident). Osx is an osteoblast lineage-specific transcription factor required for bone formation and osteoblast differentiation that is expressed in hypertrophic chondrocytes and osteoblast precursors (Hu and Olsen, 2016b). VEGF deletion in osteoblast precursor cells could affect differentiation which is the reason why the VEGF Osx KO model has not been used for the investigations included in this thesis. Ocn is expressed in mature osteoblast only, being VEGF deletion in the VEGF Ocn KO model more specific for the study of osteoblast-derived VEGF (aim of this study). Osteoblasts seem to be a predominant source of VEGF in bone (Clarkin et al., 2008). VEGF's actions in adult bone appear to be complex and VEGF receptors and sensitivity to VEGF have been reported by both osteoblasts and osteoclasts (Clarkin and Gerstenfeld, 2013) with reciprocal paracrine relationship between osteoblasts and endothelial cells reported (Hu and Olsen, 2016a).

The mechanisms driving the changes in the intracortical microstructure presented in this chapter remain to be elucidated. A possible explanation is that osteocyte cells can respond to the lack of VEGF by inhibiting bone formation or activating osteolysis.

Alternatively, the lack of VEGF could produce a response in the endothelial cells impacting on bone formation mechanisms. Without further evaluation, it is hard to tell whether the extracted pores and cavities are the living spaces for the blood vessels and osteocyte or if there is non-calcified osteoid due to a disruption in the mineralisation mechanisms. Histological examination could help to shed light on this and to detect abnormal blood vessels. Thus, one of the limitations of this study is the lack of histological information. Regarding mechanical testing, measurements were performed on femoral bones while imaging and assessment of microstructure was carried out on the tibiofibular junction, which can be considered as another limitation in this study. Mechanical testing is a destructive technique and X-ray imaging it is known to affect mechanical properties of bone. Thus, three-point bending tests on X-ray imaged tissue was not a possibility.

In Chapter 6, a tool for the detection of soft tissues in bone will be presented which could be used in the future to better understand microstructural changes due to VEGF withdrawal.

Chapter 6: Results III - Visualisation of the soft tissue comprising the intracortical vasculature using synchrotron X-ray phase contrast-enhanced tomography

6.1 Introduction

Vascular dysfunction has been linked to the pathogenesis of a broad spectrum of devastating diseases. Today, a solid body of scientific literature surrounds vascular dysfunction in the progression of atherosclerosis, cancer (both tumour growth and metastasis), infectious diseases, stroke, heart disease, diabetes, kidney failure, Alzheimer's and other age-associated diseases (Le Couteur and Lakatta, 2010; Rajendran et al., 2013). As a result, the vasculature has proved to be a reliable tool for the diagnosis and treatment of many of these conditions.

Despite cortical bone being the most important contributor to skeletal mass (Burr, 2016), age-related bone loss (Zebaze and Seeman, 2015) and – at many anatomical sites – to bone strength (Ferretti et al., 1995; Holzer et al., 2009; Mazess, 1990), it remains unclear whether an abnormal intracortical vasculature accompanies skeletal diseases. Therefore, imaging and characterisation of the bone vascular network *in situ* and hence in 3D is a promising approach to better understand bone health.

While canals in cortical bone can readily be identified and characterised in standard X-ray computed tomographic data in 3D using the negative imaging approach (Schneider et al., 2004), the soft tissue comprising blood vessels that are putatively contained within the canal networks do not provide the sufficient image contrast necessary for image segmentation. Thus, to date it has not been possible to determine whether blood vessels are present within these canals without the use of a contrast agent or histological examination.

Recently, the advantages of phase-contrast SR CT to study the soft tissue in a non-destructive, 3D fashion without the addition of contrast agents has been highlighted (Fratini et al., 2015) using the murine neurovascular network. Phase-contrast SR CT, or more specifically propagation-based phase-contrast imaging, has proved to be a simple yet powerful approach to exploit the sample-induced phase shift and to increase image contrast for low-absorbing samples when using synchrotron light sources, or more

generally coherent X-ray sources. This year alone phase-contrast SR CT has been successfully applied to visualise the microstructure of a broad range of soft tissues including spindles and nerves in murine skeletal muscle (Zeller-Plumhoff et al., 2017a), myocyte orientation in cardiac tissue (Varray et al., 2017), the vasculature of a whole heart (Gonzalez-Tendero et al., 2017), murine spinal cord (Hu et al., 2017), and 3D printed hybrid cartilage constructs (Olubamiji et al., 2017).

The aim of the study described within this chapter was to apply this methodology to the visualise soft tissues in bone, specifically the cortical bone of the tibiofibular junction of adult mice in attempts to detect the presence and size of blood vessels within the canal networks, in the absence of any contrast agent. As it is shown within this chapter, propagation-base phase contrast-enhanced tomography can indeed resolve soft tissue comprising blood vessel details in undecalficied murine bone, when an appropriate propagation distance is chosen. Furthermore, this technique allows for simultaneous visualisation of the cortical bone microstructure including osteocyte lacunae and canal networks alongside the blood vessels themselves.

6.2 Methodology

6.2.1 Propagation-based phase contrast-enhanced X-ray tomography

Standard (attenuation-based) CT is the most common X-ray tomography imaging modality, which was presented in Chapter 2 and used to generate the data presented in chapters 4 and 5. However, SR offers other X-ray imaging modalities, where the main image contrast is not due to X-ray absorption. For example, in cases where standard μCT does not provide sufficient image contrast for feature identification and segmentation, such as for the vasculature or other low X-ray absorbing soft tissues, phase contrast can considerably improve the situation.

In general, X-rays, like any other electromagnetic waves, are attenuated and phase-shifted when passing through matter (Figure 6.1a). Classical absorption contrast relies on measuring the attenuation of the X-ray beam intensity due to the sample being in the beam

path. Phase-contrast CT takes advantage of the phase shift to capture additional information from the specimen. The refractive index n for this interaction is defined as

$$n = 1 - \delta + i\beta \qquad (6.1)$$

with β being related to μ (the absorption coefficient from the Beer-Lambert law in equation (2.1) via

$$\mu = \frac{4\pi}{\lambda}\beta \qquad (6.2)$$

λ being the wavelength and $i = \sqrt{-1}$. δ is the above equation relates to the phase shift

$$\Phi(\mathrm{x}, \mathrm{y}, \mathrm{z} = 0) = -\frac{2\pi}{\lambda}\int \delta(x, y, z)dz \qquad (6.3)$$

$z = 0$ being the contact plane (when the X-rays have just passed through the sample).

δ can be two to three orders of magnitude larger than β , thereby making phase-contrast imaging an important alternative to classical absorption-based imaging, especially if absorption contrast between different components of a sample is low, as is usually the case for soft-tissue samples. Readers interested in a deeper description of the physical principles behind phase-contrast imaging are invited to revise the following selection of manuscripts (Cloetens et al., 1999; Giorgio Margaritondo, 2002; Mayo et al., 2012; Pfeiffer et al., 2006).

The simplest phase contrast CT technique in terms of implementation is free space propagation, where the X-rays are allowed to propagate towards the detector without alteration. There are other phase-contrast X-ray tomography arrangements such as grating interferometry (Weitkamp et al., 2005) or diffraction enhanced imaging (Chapman et al., 1997) that will not be discussed here for simplicity.

When the imaging detector is placed immediately behind the sample only attenuation is measured (Figure 6.1b). In propagation-base phase-contrast imaging, the X-rays propagate for a certain distance before reaching the detector. It is a simple but

powerful approach to exploit the sample-induced phase shift and to increase image contrast for low-absorbing samples when using synchrotron light sources, or more generally coherent light sources. By leaving an appropriate space between the sample and the detector (Figure 6.1c) and through constructive and destructive interference of neighbouring and coherent X-ray waves the phase shift of the X-ray beam caused by the sample is transformed into intensity variations that are recorded by the detector and result in dark and bright fringes around the edges of detected object (Figure 6.1c). This arrangement increases the visibility of edges through interference fringes and allows the study of samples with either low X-ray absorption or multiple constituents (as it is the case of blood vessels embedded within the calcified bone matrix).

6.2.2 Sample imaging

Right murine tibiae (n=4, C57BL/6, 15 weeks of age) were mechanically fixed with wax to prevent sample movement and the tibiofibular junctions scanned using SR CT at the TOMCAT beamline of the SLS at a voxel size of 1.3 μm and 325 nm (with the highest the spatial resolution needed to detect the smallest intracortical capillaries) at two different sample-to-detector distances (15 and 25 mm, for standard X-ray tomography and phase-sensitive imaging respectively; Figure 6.1b/c) (Lovric et al., 2014; Weitkamp et al., 2011). 1501 projections were acquired over a range of 180 degrees, at a photon energy of 21 keV, 18 ms exposure time per projection, which were corrected for ring artefacts due to potential scintillator defects and reconstructed using filtered backprojection. Scans were centred at the tibiofibular junction and μCT datasets consisted of a stack of 2000 reconstructed μCT slices.

6.2.3 Image processing and analysis

μCT datasets were processed and analysed as described in Chapter 3 to detect the mineralised tissue, extract porosity and separate canals and lacunae from the lowest resolution datasets. Segmentation of the soft tissue comprising the blood vessels was only

possible at the highest resolution and for datasets with phase-sensitive propagation distances. Vascular segments were manually detected using commercial software AVIZO 9 (FEI, Oregon, USA).

Parameters for the quantification were defined as:

- Vascular canal density (%): volume of cortical canals in the CT dataset normalised with the total cortical tissue volume;

- Average canal diameter (microns): mean diameter dimension of the canals in the CT dataset;

- Osteocyte lacunar density (number per 100 cubic microns of mineralised volume): number of osteocyte lacunae in the CT dataset per unit of mineralised cortical bone;

- Canal occupancy (%): percentage of canal structures that are filled with a blood vessel (note that this parameter was quantified in both CT and histological data, for the CT data 60 reconstructed CT slices per dataset were inspected);

- Vascular space (%): area of the vascular structure normalised with the total canal area (parameter computed using 60 CT slices per dataset).

6.2.4 Histological evaluation

Histological evaluation was performed as described in Chapter 4 using Giemsa and Pentachrome stainings. Canal occupancy was quantified in 3 sections per tibiofibular junction. Quantification was performed on histological sections manually using the undivided cortical ring. Canals filled with blood vessels were counted and compared with the total number of intracortical canals.

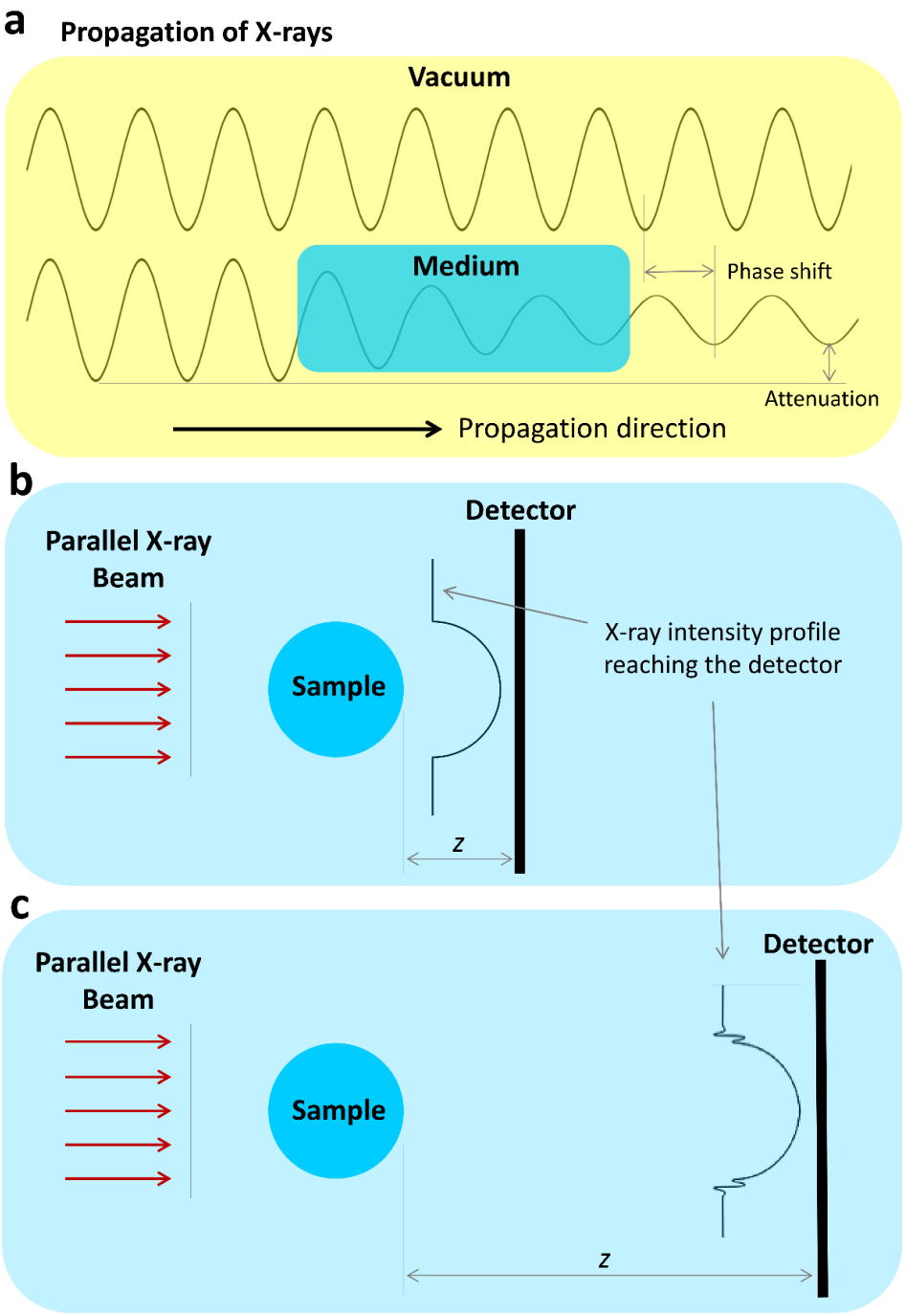

Figure 6.1. Propagation-based phase contrast-enhanced imaging. (A) Propagation of X-rays in vacuum vs medium. Schematic representation of a parallel beam inline synchrotron tomography set-up. A near-parallel X-ray beam passes through a sample with hidden internal microstructure. Radiographs (tomographic projections) are recorded on a detector placed at a single fixed distance z from the sample. In standard X-ray imaging (B) the detector is placed immediately behind the sample. By leaving an appropriate drift space between the sample and the imaging detector (C) visibility of the specimen interfaces is enhanced.

6.3 Results

6.3.1 Detection of intracortical blood vessel using propagation-based phase contrast-enhanced imaging.

Figure 6.2 shows the phase contrast-enhanced imaging ability to detect cortical vascular structures in bone. Figure 6.2a shows a schematic representation of an intracortical canal occupied by a blood vessel with image intensity profiles for both propagation distances (Figure 6.2b/d). The observed differences in the intensity profiles make possible the detection of the soft tissue comprising the blood vessel at a phase-sensitive propagation distance (and not for standard X-ray tomography) (Figure 6.2c/e). Larger vascular structures can be identified at a voxel size of 1.3 µm (Figure 6.3a) but the smallest intracortical capillaries (~5 µm diameter and >1 µm wall thickness) could only be detected at a voxel size of 325 nm as shown in Figure 6.3c.

6.3.2 Histological validation

Microscopic analysis of calcified bone sections stained with either Pentachrome or Giemsa revealed the presence of blood vessels within intracortical canals demonstrating that the structures identified by phase contrast-enhanced tomography are blood vessels (Figure 6.3b/d/f/h/j). Quantification of cortical canal occupancy by blood vessels was carried out on histological and CT data with high % of canal occupancy revealed by both techniques (86.91 ± 12.54 and 95.77 ± 1.55; respectively; Figure 6.3k).

6.3.3 Vascular parameters

Computations for canal volume density, canal diameter and canal space occupied by the vascular structure were performed on CT data with mean value and standard deviation results shown in Table 6.1 for n=4 datasets. % of canal volume was found to be 0.81 ± 0.12,

the average canal diameter was 7.98 ± 0.70 microns and vascular space 85.45 ± 2.85 % of the available canal space.

6.3.4 Simultaneous visualisation of the cortical porosity comprising the calcified intracortical microstructure

The cortical canal network and osteocyte lacunae were also assessed alongside with the soft tissue comprising the vasculature and cortical porosity extracted from standard X-ray data and classified into vascular canals and osteocyte lacunae (Figure 6.4). The assessment of the calcified cortical microstructure allowed the quantification of osteocyte lacunae density which was found to be 62.34 ± 0.72 lacunae per 100 cubic microns of mineralised tissue. Furthermore, the mineralised cortical geometry could be used to derive porosity measurements and mineralised tissue volume computations. 3D rendering of vascular structures within intracortical canals are shown in Figure 6.5.

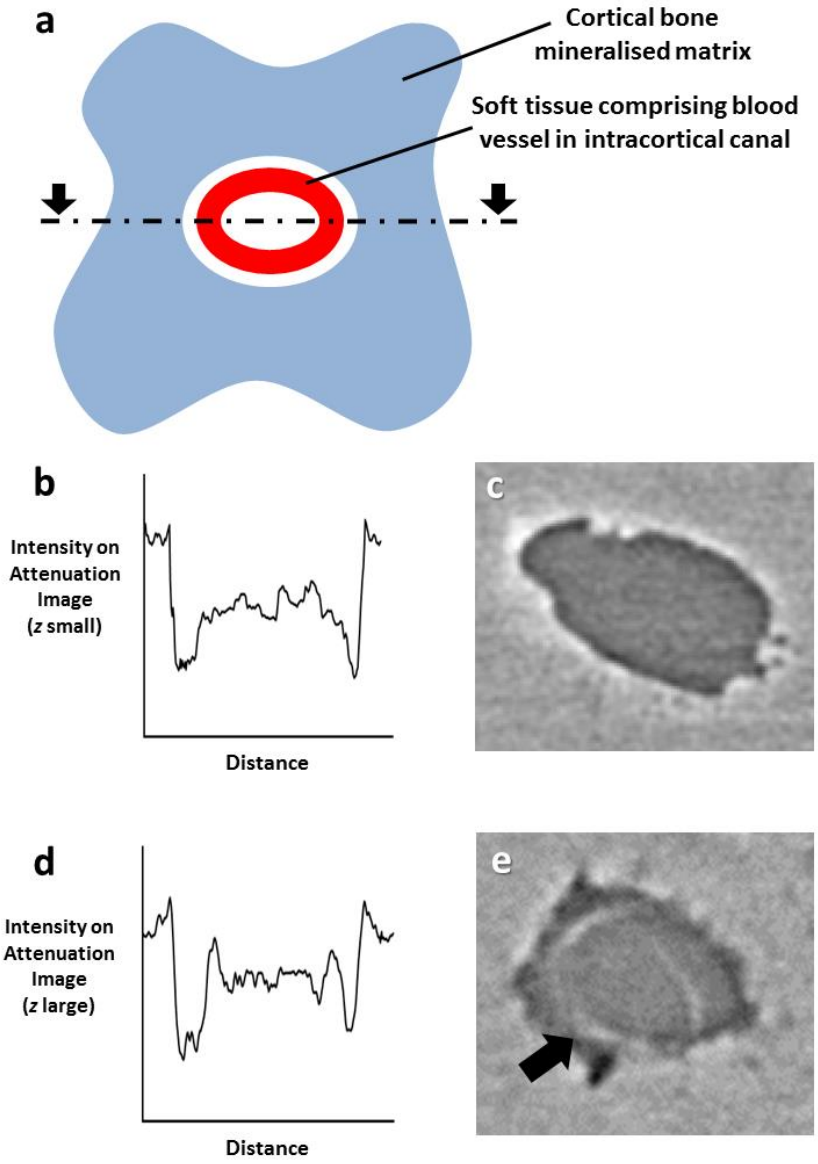

Figure 6.2. Phase contrast-enhanced visualisation of the soft tissue comprising blood vessels in calcified bone. (a) Schematic representation of an intracortical canal occupied by a blood vessel. Image intensity profile plotted along a line intercepting intracortical canal and internal blood vessel for standard X-ray micro-computed tomography (µCT) (b). Magnified area on µCT reconstructed slice containing an intracortical canal (0.325 µm voxel size, 15 mm propagation distance) (c). Image intensity profile plotted along a line intercepting intracortical canal and internal blood vessel for phase contrast-enhanced µCT (d). Magnified area on phase contrast-enhanced µCT reconstructed slice containing an intracortical canal with internal blood vessel visible and identified by the arrow (0.325 µm voxel size, 25 mm propagation distance) (e).

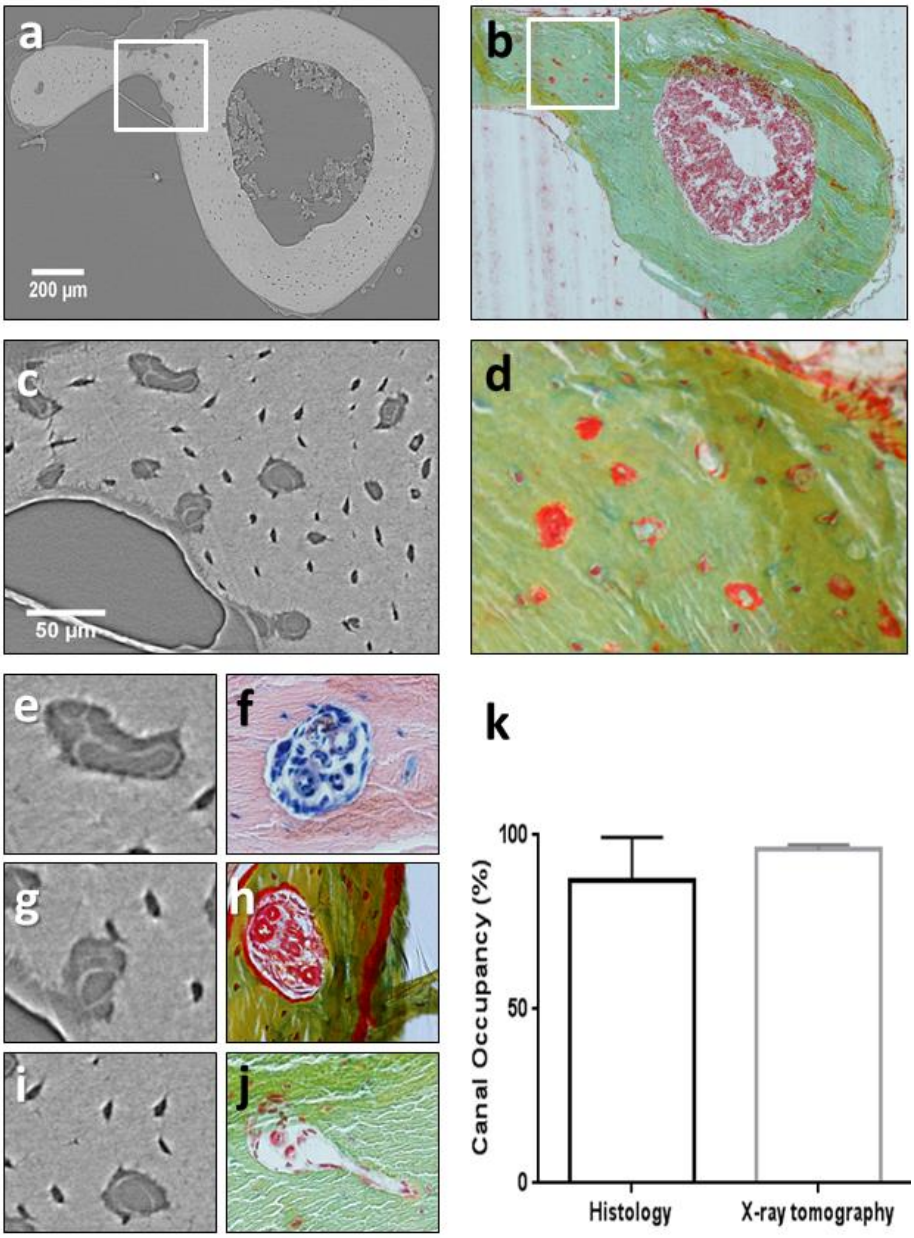

Figure 6.3. Detection of intracortical blood vessels by phase contrast-enhanced micro-computed tomography and validation by histology. (a) µCT slice of the murine tibiofibular junction with large blood vessels visible (1.3 µm voxel size) and square identifying region for higher magnification. (b) Histological cross-section of the tibiofibular junction (Pentachrome staining) and square identifying region for higher magnification. (c) Phase contrast-enhanced µCT slice with intracortical blood vessels visible (0.325 µm voxel size). (d) Identification of blood vessels (red) on histological section (Pentachrome). (e/g/i) Magnified cortical canal occupied by vasculature visible on CT data. (f) Magnified histological section with blood vessel visible (Giemsa staining). (h/j) Magnified histological section with blood vessel visible (Pentachrome staining). (k) Quantification of cortical canals filled with blood vessels in histological sections and CT slices (mean values and SD).

PARAMETER	Mean	SD
Canal Volume (%)	0.809	0.117
Canal Diameter (microns)	7.984	0.698
Canal Occupancy (%)	95.771	1.548
Vascular Space (%)	85.449	2.851
Osteocyte Density (# per 100 cubic microns)	62.335	0.719

Table 6.1. Indices for 15 weeks old C57BL/6 female mice. Indices are: canal volume normalised with total cortical volume, average canal diameter, canal occupancy by blood vessels, vascular volume normalised with cortical canal volume and osteocyte lacunae density normalised with cortical bone volume. Quantification performed in 4 X-ray tomography datasets, using the total scanned area for canal volume, canal diameter and osteocyte density indices and 60 sliced per dataset for canal occupancy and vascular space indices.

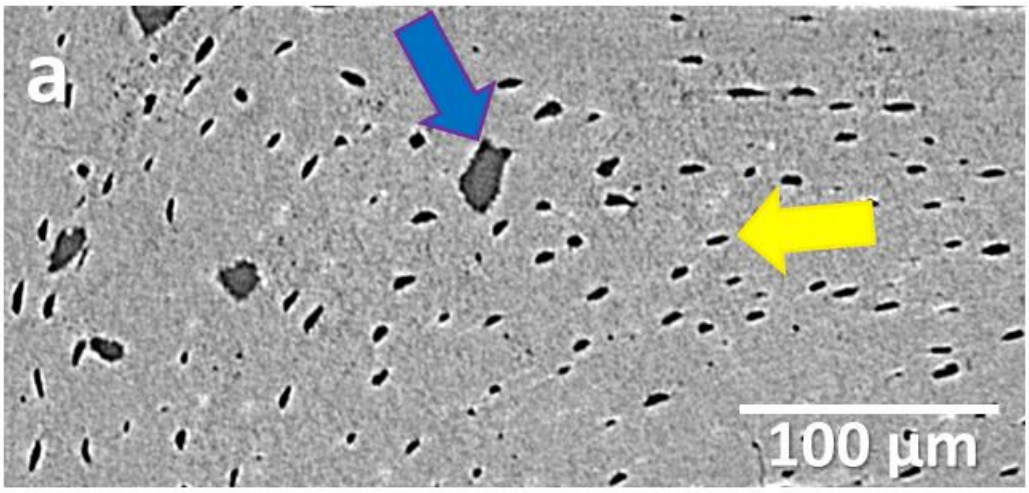

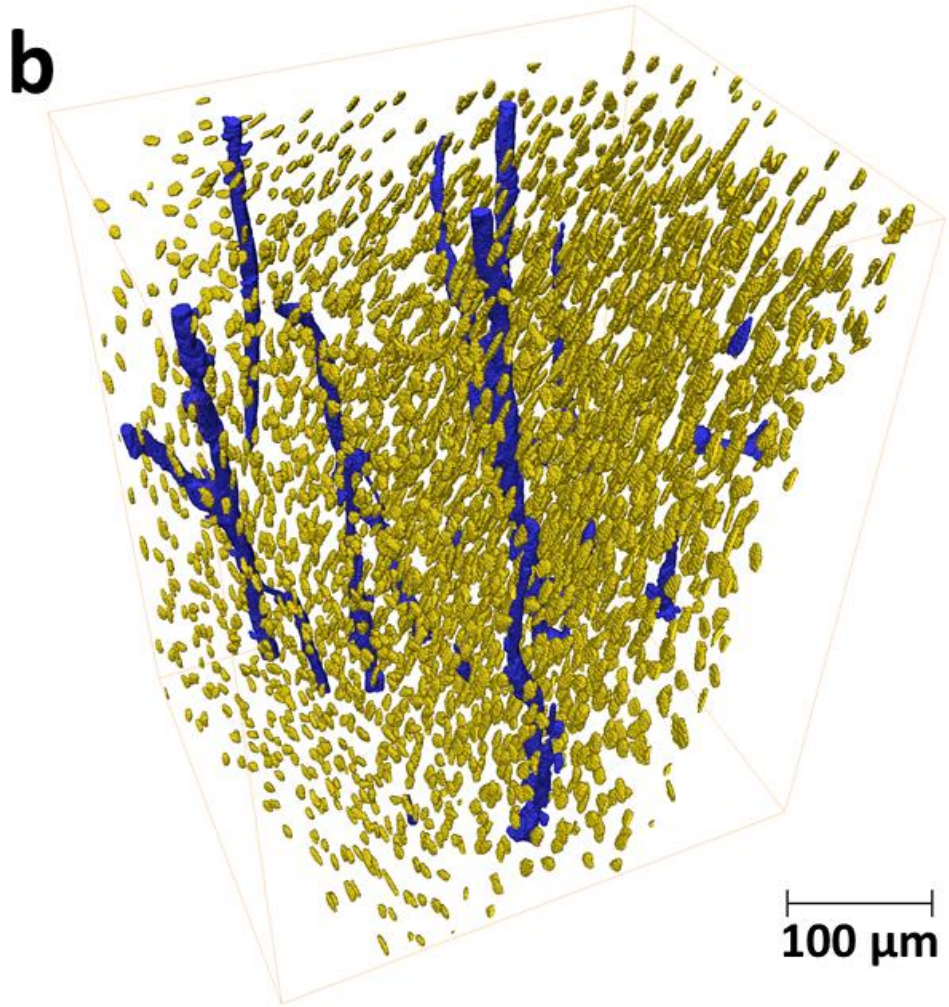

Figure 6.4. Cortical microstructure. Identification of intracortical canals (blue) and osteocyte lacunae (yellow) on micro-computed tomography (µCT) slice (a) and 3D rendering of intracortical canals (blue) and osteocyte lacunae (yellow) (b). Images extracted from 1.3 µm voxel size µCT dataset.

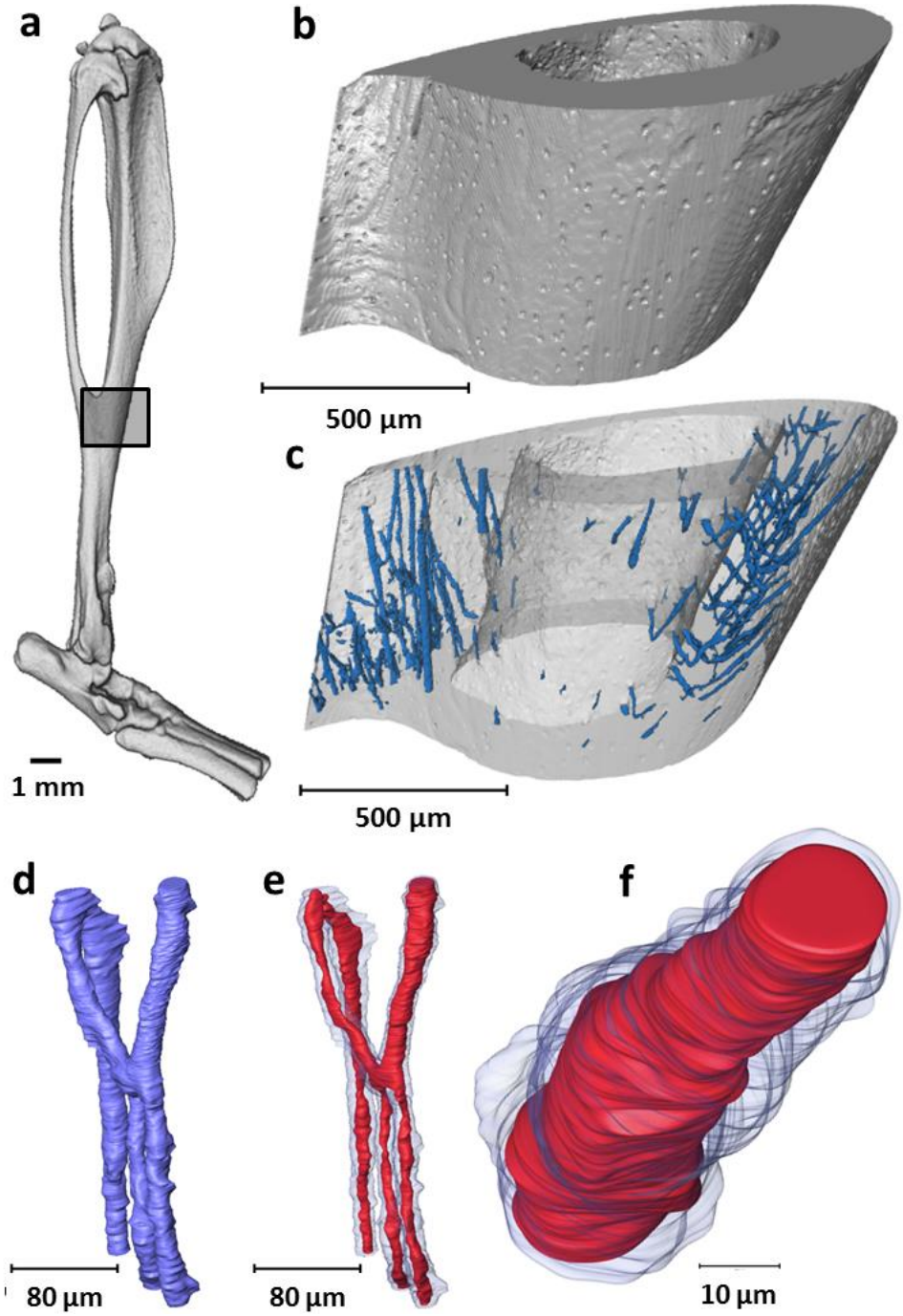

Figure 6.5. 3D visualisation of intracortical blood vessel. (a) 3D rendering of murine tibia with identification of the tibiofibular junction. (b) 3D rendering of scanned tibiofibular junction region (1.3 µm voxel size) and (c) detection of intracortical canals (blue) as a negative imprint of the mineralised tissue (extracted from 1.3 µm voxel size dataset). (d) Magnified area of the 3D intracortical network (extracted from 0.325 µm voxel size dataset) and (e) detection of the soft tissue comprising blood vessels (red) within intracortical canals (blue) (extracted from 0.325 µm voxel size dataset) and magnified region (f).

6.4 Discussion

The study presented in this chapter has demonstrated that phase contrast-enhanced tomography allows imaging of the intracortical vasculature in unstained, unperfused and undecalcified murine bone at sufficient spatial resolution to identify the presence of individual blood vessels within the cortical canals and their size. Importantly, the mineralised cortical geometry including vascular canals and osteocyte lacunae, could also be imaged in parallel with the soft tissue which contribute to bone porosity measurements, bone tissue volume computations and computational mechanics. Histological examination confirmed that the structures detected within the cortical canals are blood vessels, proving the ability of X-ray phase contrast-enhanced tomography to assess the cortical bone vasculature. The approach allows the quantification of vascular parameters such as vascular canal density, diameter, occupancy and vascular space. It has been also provided numerical values for these parameters in the young adult murine tibiofibular junction that can now be used to evaluate age-related and disease-associated deviations.

Compared with histological examination, bone specimens can be evaluated in 3D and non-destructively using μCT; not requiring special sample preparation. Although conventional absorption-based μCT is not sensitive enough to provide sufficient contrast for soft tissues, such as the vasculature, it has been used to provide spatial clues for the location of the blood vessels that reside within the intracortical canal network (Schneider et al., 2004; Schneider et al., 2007; Schneider et al., 2009; Schneider et al., 2013). The intracortical canal network can be extracted as a negative imprint of the calcified tissue from standard μCT images and several studies have done this in human (Cooper et al., 2003; Cooper et al., 2007a; Cooper et al., 2007b) and rodent (Britz et al., 2010; Schneider et al., 2007; Schneider et al., 2013; Thurner et al., 2010) bone using both lab-based and synchrotron X-ray sources. However, intracortical canals and blood vessels are not the same thing and from conventional absorption-based μCT data, it is not clear if specific "vascular" canals indeed contain blood vessels or not, unless additional histology has been performed. Further, we do not know if there are bone pathologies (or stages of pathologies) where blood vessels are lost from the canals, leaving the canals alone as a poor indicator of actual vessel structure. Therefore, the most significant limitation of conventional X-ray absorption-based μCT has been the inability to accurately assess both

calcified and soft tissues simultaneously. It has been proved within this chapter that limitation can be overcome with that phase contrast-enhanced tomography.

There are of course limitations associated with this study as the use of phase contrast SR CT in bone. The main disadvantage of SR CT imaging is the availability of, and access to, the few SR sources worldwide (http://www.lightsources.org/regions). Allocation of scanning time is generally granted with proposals awarded on a competitive basis, with proposals submitted a half year in advance. Another limitation of the approach here presented is that it has not been possible to observe vascular details at the submicron scale. Measurements of the vessel wall carried out on histological sections confirmed that the intracortical capillaries we are visualising generally have a wall thickness below the micrometre. At the current voxel size (325 nm) and resolution (2-3 times higher that voxel dimension), distinction of the two vessel surfaces (outer and luminal) is not currently possible. Thus, the single phase-related fringe observed corresponds to both outer and luminal surfaces of the microvessel; this is enough to determine the presence of the vascular structure within the canal and provide an indicator for its size. Increasing the spatial resolution will allow the detection of tube-like structures and access submicron vascular details which were beyond the scope of this work.

Synchrotron radiation dose for the described experiments is estimated to be below 6 MGy, and even though no damage leading to detrimental effects of the sample microstructure is expected (Dierolf et al., 2010; Schneider et al., 2013; Zeller-Plumhoff et al., 2017b), we cannot consider this technique as non-invasive. In fact, the invasiveness of synchrotron radiation is a matter of definition according the application. For example, it has been reported that a similar radiation dose can alter the mechanical properties of bone (Barth et al., 2010; Barth et al., 2011; Schneider et al., 2013), which means that we need to take this into account when planning to perform mechanical tests. On the other hand, similar radiation dose has been proven to be compatible with immunohistochemical techniques with preservation of the epitopes (Zeller-Plumhoff et al., 2017b).

It is also important to highlight that even though local tomography is associated with image distortion and small perturbations in the image intensity, such artefacts are

particularly a matter of concern in regions close to the boundary of the field of view and thus have been avoidable in this study. Furthermore, SR CT presents some advantages when compared with desktop X-ray sources; for instance, beam hardening effects are not present in SR CT since the radiation is monochromatic, in addition the fast acquisitions minimise artefacts related to sample movement or thermal stability.

The quantification of canal occupancy on CT images can be used as the ultimate proof that the cortical canals are the living space of the vasculature. Differences between occupancy measures undertaken on histological and CT images highlight the accuracy of the 3D method over the 2D one. Histological information gets damaged due to sample preparation and cutting, it is usual to find distortion, tearing and folding on the sectioned tissue that makes the interpretation of the results hard and somehow subjective. With all this, the approach presented in this chapter is most probably the closest we can get to the real *in situ* 3D arrangement of blood vessels in cortical bone.

Measurement of the vascular space within the canal reveals that there is a gap between canal surfaces and blood vessel since only 85 % of the canal space was taken by the capillary in average. It is important to note that the bone samples have been chemically fixed to allow visualisation of the soft tissue. This process could have altered the vessel geometry and it remains unclear if that gap exists in-vivo and the function of this perivascular space.

To conclude, it has now been shown that the bone vasculature and cortical bone microstructure in mice can be assessed simultaneously with no sample preparation. This study can provide new opportunities to quantitate and better evaluate the role the vasculature plays in specific skeletal sites and different animal models. Visualisation of the 3D bone vascular network is a prerequisite for improved understanding of its role in the regulation of bone health and disease. The presented approach has the potential to link vascular abnormality to the pathogenesis of various skeletal conditions and could revolutionise the way we treat and diagnose bone disease.

Chapter 7: General discussion

7.1 Research summary

Fragility fractures represent a socio-economic burden, yet effective systematic treatments for the prevention of osteoporotic fractures are still lacking. In this context, the bone vasculature is identified as a potential therapeutic target. The possibility to prevent age-related bone fragility by preserving the vasculature remains an open question.

This research started with the development of an imaging and analysis methodology for the assessment of vascularisation in cortical bone presented in Chapter 3. It was shown that the intracortical vascularisation and more specifically 3D spatial relationships between the vasculature and the osteocyte lacunae can be assessed with this imaging modality at a resolution close and above the micrometre, which is enough to detect the presence of the osteocyte lacunae, the smaller microstructural details of interest within this research. The mouse was used as a model and a skeletal site where the role of the vasculature in cortical bone could be further evaluated was identified. The bone tissue in the murine tibiofibular junction was purely cortical, the scans for this region were easy and fast to set up due to the clear anatomical landmark.

The young-adult murine tibiofibular junction was then characterised, and its vascularisation assessed in Chapter 4. The vasculature was found to be heterogeneously distributed. In particular, the posterior region was found to be very highly vascularised in the young-adult mouse. In contrast, lateral and medial compartments of the cortices presented very low presence of capillaries. The murine tibiofibular junction was then used to answer the biological question. The main biological hypothesis was that the intracortical vasculature is reduced with age. The results in Chapter 4 revealed that there is an age-related recession of the intracortical vascularisation in the posterior region of the tibiofibular junction which increased the distance between the osteocytes and the vasculature within this skeletal site. This alteration in the intracortical vasculature was accompanied by an age-related thinning of the cortices.

According to the scientific literature, the expression of the proangiogenic factor VEGF decays with age for several cell types and low serum levels of the signal have been found in postmenopausal osteoporotic women. In other to test whether VEGF had a deleterious effect on bone, the effect of osteoblast-derived VEGF deletion in a transgenic mouse was analysed. Results in Chapter 5 show that the lack of VEGF has an impact of cortical bone microstructure with a reduction in the mineralised tissue. The calcified matrix appeared disrupted in the transgenic animals lacking VEGF with clear regions of low mineralisation. The methodology developed in Chapter 3 failed to accurately detect vascular structures and osteocyte lacunae since it was optimised to deal with mineralised tissues. As a result, the areas of low mineralisation within the transgenic bone matrix were incorrectly detected as porosity with enlarged and interconnected osteocyte lacunae.

Phase-contrast enhanced tomography was explored in Chapter 6 in order to improve image contrast and visualise non-mineralised tissues in bone. Results revealed identification of soft tissue structures comprising capillaries within the intracortical network. The technique was proven to detect the bone vasculature in undecalcified bone without the use of contrast or staining agents or any sample preparation. The technique allowed the simultaneous visualisation of both the soft and the hard tissues within bone.

7.2 Relevance of the findings, limitations and future opportunities

The most exciting and promising achievement of this project was the ability to answer the proposed biological questions with the use of the developed methodology. The observed clear and early recession of the intracortical vasculature are consistent with previous investigations. Age-related reductions in limb blood flow and vascular conductance have been reported in rodents (Dinenno et al., 1999). Reduced vascularisation in the medullary cavity of the tibia have been found in rats (Mekraldi et al., 2003) and mice (Ding et al., 2011; Roche et al., 2012) using ovariectomy as a model for postmenopausal osteoporosis. This research has found a correlation between ageing and decreased intracortical vasculature but one of the limitations of the approach here presented is that causality cannot be proven. No severe signs of advanced bone deterioration were observed

in the older group of animals due to the age and it could be speculate that such early vascular alterations may initiate later bone changes. If this is found to be true in the future, if vascular changes precede bone loss, the vasculature could therapeutically target to treat bone fragility conditions and improve bone strength. Given this, future experiments could aim to assess bone vasculature non-invasively in vivo. Longitudinal studies will help us to shed light into the mechanisms by which blood vessels are disappearing from bone. This, together with an in vivo assessment of the bone microstructure will help us to better understand the role of the vasculature in adult bone remodelling.

In Chapter 3, the tibiofibular junction was presented as the ideal skeletal site to further investigate the role of the vasculature in bone within this thesis. The highly vascularised posterior region of the murine tibiofibular junction offers a skeletal site that can be used as a model in bone research. However, osteoporotic fractures of the tibia are very rare in humans which can question the selection of that skeletal site for the investigations here presented. The most clear structural difference between human and murine bone is that mice lack obvious osteonal or Haversian canals in cortical bone and, thus, secondary remodelling (Felder et al., 2017). For this, the use of this animal in bone research has been controversial. The research presented in this thesis shows potential similarities between the canals in the unusually thinker posterior region of murine tibiofibular junction and the Haversian canals in humans. If this is found to be true, the murine skeletal site could be used as a model and experiments could be carried out to better understand age-related bone changes in humans and the outcome of potential pharmacological interventions. Given this, future experiment could aim to better characterise the longitudinal canals present in the posterior region of the murine tibiofibular junction. In particular, the presence of osteoclasts on the surfaces of these canals could be detected, ideally in vivo and its activity assessed with time, to investigate if this region experiences remodelling. Evidence indicates that cortical porosity increases with age in humans accompanied by endosteal resorption (Cooper et al., 2007a; Zebaze and Seeman, 2015) but we still do not know how these age-related changes shape the bone vasculature. The author of this thesis believes that the concept of bone porosity requires redefinition in this context. The studies reporting increased cortical porosity in humans are

actually reporting a reduction in mineralised matrix. Whether the pre-existing pores and cavities (where the osteocyte cells and the blood vessels reside) enlarge or multiply with age remains to be elucidated. What we know is that bone is lost at the endosteal surface by the process of “trabecularisation”. As a result, the cortex is eroded, and new cavities are formed. Whether these new cavities contribute to cortical porosity measurements should be further evaluated.

The computation of 3D distances within this thesis provides an indicator for cortical bone vascularisation. The endosteum is a vascular membrane by definition. Blood cells are produced in the medullary cavity. The computation of distances to the nearest bone surface including endosteum, periosteum and intracortical vascular canals provides the minimum distance to a source of blood. However, some assumptions were made during the development of the methodology. In particular, endosteal and periosteal surfaces have been assumed to contribute equally in the computation of distances and this might not be the case. Perfusion rates through endosteal and periosteal surfaces could be completely different, and this is a limitation of the study. On the other hand, it is important to highlight that, when the computed tissue distances are particularised for the osteocyte lacunae, the result is not only an indicator for cell nutrition but also a measurement of how deeply embedded the osteocytes are within the matrix. Osteocytes are thought to sense changes in their mechanical environment and orchestrate bone formation and bone resorption events. Osteoblasts and osteoclasts can be found at the bone surfaces and the computed distances could also provide information about the quality of the communication between osteocytes and effector cells. More particularly, Chapter 4 reported an age-related increase on these distances which could have an impact in the way bone cells communicate in aged bone.

In Chapter 5, the lack of VEGF had a dramatic effect in matrix mineralisation and integrity. The exact mechanisms by which these deleterious changes are driven remain to be elucidated. As a possible explanation, it could be proposed that osteocyte cells can respond to VEGF, the lack of the proangiogenic factor could impact osteocyte capacity to mineralise or maintain its surrounding matrix. Alternatively, blood vessels in bone could react to the lack of VEGF and inhibit bone formation mechanisms. We know that VEGF expression is reduced in multiple cell types with age (Efimenko et al., 2011; Jiang et al.,

2008; Pola et al., 2004; Rivard et al., 1999; Wilson et al., 2010) and low serum levels of VEGF have been found in postmenopausal osteoporotic woman. Whether VEGF can be used to maintain structural integrity to improve bone strength remains answered. One of the limitations of the approach here presented is that X-ray tomography can only provide structural information. Given this, future experiments could shed light into the way bone cells and endothelial cells communicate and react to the lack of VEGF. Cell culture (and co-culture) experiments could help us to better understand how cells behave when VEGF is not present. In addition to this, at the organ level, mechanical testing could be used to assess bone mechanical competence when VEGF is supressed, overexpressed or rescued.

X-ray tomography was presented as the ideal tool for the investigation of the problem under consideration. However, in Chapter 5, the inability of standard (absorption based) CT to visualise soft tissue was highlighted. The lack of VEGF resulted in areas of low mineralisation within the bone matrix and CT failed to assess whether these areas were pores and cavities or non-mineralised osteoid. The methodology developed in Chapter 3 was optimised to work on mineralised tissues and failed to extract additional information about the microstructure of a low mineralised matrix. Phase-contrast enhanced X-ray tomography emerged in Chapter 6 as an alternative to provide soft tissue structure. It was proven that the imaging modality can accurately detect even the smallest capillaries in cortical bone. Presence of blood vessels within the intracortical canals was confirmed in undecalcified bone without special sample preparation. Interestingly, the technique proved an ability to detect both the soft and hard tissues within bone simultaneously. Comparison with histological examination highlighted the advantages of phase-contrast enhanced tomography. Phase-contrast CT is not only three-dimensional but also proved to be more accurate that histology for detection of vascular structures. The imaging modality could be easily incorporated in bone research. It will be particularly useful to interrogate interactions between soft and hard mineralised tissues. In the immediate future, phase-contrast CT could be used to visualise the soft tissue comprising the osteocyte cells, detecting their presence within the lacunae in a similar way it has been done in this thesis for the vascular canals. The bone vasculature could be studied in more detail. In particular, it will be interesting to evaluate the evolution of the vasculature with the progression of

different skeletal pathologies. However, CT phase-contrast imaging counts with some limitations. The radiation dose of the experiments within this thesis was estimated to be below 6 MGy which makes this imaging modality incompatible with any form of life. Measurements can only be performed ex vivo. Additionally, the technique cannot be considered non-invasive. In fact, the invasiveness of synchrotron radiation is a matter of definition according to the application. For example, it has been reported that a similar radiation dose can alter the mechanical properties of bone (Barth et al., 2010; Barth et al., 2011; Schneider et al., 2013). Surprisingly, similar radiation dose has been proven to be compatible with immunohistochemical techniques with preservation of the epitopes (Zeller-Plumhoff et al., 2017b). In the near future, advances in CT technology could results in the development of digital and 3D histological routines replacing conventional 2D sectioning.

7.3 Conclusions

This is the first investigation reporting an age-related recession of the intracortical vasculature in murine bone. The experiments described in this thesis indicate that a lack of VEGF impacts murine bone microstructure. The developed methodology has been proved to be suitable to provide these answers. The vasculature has been identified as a potential therapeutic target for the treatment of bone fragility problems in age-related degenerative diseases such as osteoporosis. The murine tibiofibular junction offers a context where the connection between vasculature and cortical bone can be specifically interrogated. The use of phase-contrast X-ray tomography in bone research has the potential to link vascular abnormality to skeletal pathology in animal models which could help us to shed light into the mechanisms leading to age-relate degeneration of the human skeleton and could impact the way we treat and diagnose bone conditions.

Appendices

Appendix A Tables

Appendix A

	15-week-old				Comparison A-P		Comparison A-L		Comparison A-M		Comparison P-L		Comparison P-M		Comparison L-M	
Parameter	Anterior	Posterior	Lateral	Medial	(%)	p	(%)	p	(%)	p	(%)	p	(%)	p	(%)	p
Ca.V/Ct.TV (%)	0.554 ± 0.122	1.261 ± 0.268	0.159 ± 0.037	0.166 ± 0.052	127.617	0.031	-71.300	0.031	-70.036	0.031	-87.391	0.031	-86.836	0.031	4.403	0.688
<Ca.Dm> (micrometres)	7.103 ± 0.620	8.039 ± 0.607	6.431 ± 0.710	6.754 ± 0.743	13.178	0.313	-9.461	0.219	-4.913	0.438	-20.002	0.031	-15.985	0.063	5.023	0.563
N.La/CT.BV (per 100 cubic micrometres)	63.585 ± 1.972	61.917 ± 3.386	62.878 ± 2.995	62.917 ± 2.985	-2.623	0.438	-1.112	0.844	-1.051	0.563	1.552	0.563	1.615	0.688	0.062	>0.999
La.S.Sp$_{95}$ (micrometres)	64.243 ± 1.193	70.373 ± 2.908	70.026 ± 1.455	70.733 ± 1.153	9.542	0.031	9.002	0.031	10.102	0.031	-0.493	>0.999	0.512	0.688	1.010	0.031
<La.S.Sp> (micrometres)	31.993 ± 0.592	32.629 ± 1.047	37.658 ± 1.509	37.248 ± 0.998	1.988	0.156	17.707	0.031	16.425	0.031	15.413	0.031	14.156	0.031	-1.089	0.156

Table A1. Characterisation of young-adult murine tibiofibular junction. n=6 mice, data expressed as mean ± SD.

Parameter	Anterior	Posterior	Difference (%)	U test
				p
Ca.Co	0.093 ± 0.011	0.269 ± 0.053	188.298	0.0313

Table A2. Connectedness for the anterior and posterior vascular canal network of the murine tibiofibular junction. n=6 mice, data expressed as mean ± SD.

Parameter	Intracortical Canals Included	Intracortical Canals Excluded	Difference (%)	U test
				p
Max tissue distance to bone surface (micrometres)	117.285 ± 5.785	191.180 ± 8.421	63.005	0.0313

Table A3. Effect of the exclusion of intracortical vasculature in tissue distances to bone surface in the young-adult murine tibiofibular junction. n=6 mice, data expressed as mean ± SD.

	Parameter	15-week-old	10-week-old	Difference (%)	t test *p*
µCT	Ct.Th (micrometres)	221.380 ± 5.956	192.510 ± 9.065	-13.041	0.002
	Ca.V/Ct.TV (%)	0.585 ± 0.111	0.444 ± 0.092	-24.076	0.056
	<Ca.Dm> (micrometres)	7.103 ± 0.621	7.261 ± 1.033	2.232	0.898
	N.La/Ct.BV (per 100 cubic micrometres)	61.566 ± 1.011	61.391 ± 1.153	-0.285	0.898
	$La.S.Sp_{95}$ (micrometres)	71.025 ± 1.857	76.246 ± 2.427	7.351	0.002
	<La.S.Sp> (micrometres)	34.264 ± 0.866	35.284 ± 0.706	2.978	0.093
Histology	Occupancy of canals (%)	79.226 ± 6.080	86.905 ± 12.543	9.692	0.800

Table A4. Age-related changes in the murine tibiofibular junction. n=6 mice per group, data expressed as mean ± SD.

	Anterior		Diff (%)	U test	Posterior		Diff (%)	U test	Lateral		Diff (%)	U test	Medial		Diff (%)	U test	ANOVA		
Parameter	15-week-old	10-month-old		*p*	15-week-old	10-month-old		*p*	15-week-old	10-month-old		*p*	15-week-old	10-month-old		*p*	Age	Region	Interaction
Ca.V/Ct.TV (%)	0.554 ± 0.122	0.607 ± 0.059	9.592	0.474	1.261 ± 0.268	0.674 ± 0.085	-46.538	0.002	0.159 ± 0.037	0.159 ± 0.055	-0.240	0.788	0.166 ± 0.052	0.157 ± 0.055	-5.347	0.571	<0.001	<0.0001	<0.0001
<Ca.Dm> (micrometres)	7.103 ± 0.620	7.261 ± 1.033	2.232	0.898	8.039 ± 0.607	8.017 ± 0.816	-0.271	0.898	6.431 ± 0.710	6.399 ± 0.789	-0.503	0.898	6.754 ± 0.743	6.016 ± 0.757	-10.939	0.132	0.495	<0.0001	0.534
N.La/CT.BV (per 100 cubic micrometres)	63.585 ± 1.972	64.479 ± 2.076	1.406	0.474	61.917 ± 3.386	61.502 ± 3.032	-0.670	0.898	62.878 ± 2.995	60.659 ± 1.972	-3.528	0.180	62.917 ± 2.985	61.352 ± 3.628	-2.487	0.305	0.340	0.194	0.549
$La.S.Sp_{95}$ (micrometres)	64.243 ± 1.193	59.068 ± 1.046	-8.055	0.002	70.373 ± 2.908	81.073 ± 5.048	15.204	0.004	70.026 ± 1.455	65.466 ± 1.531	-6.512	0.002	70.733 ± 1.153	66.289 ± 1.510	-6.283	0.002	0.209	<0.0001	<0.0001
<La.S.Sp> (micrometres)	31.993 ± 0.592	28.813 ± 0.413	-9.941	0.002	32.629 ± 1.047	37.194 ± 1.606	13.99	0.002	37.658 ± 1.509	33.560 ± 1.332	-10.881	0.002	37.248 ± 0.998	32.853 ± 1.520	-11.798	0.002	<0.0001	<0.0001	<0.0001

Table A5. Age-related changes in the four quadrants of the murine tibiofibular junction. n=6 mice per group, data expressed as mean ± SD.

Appendix B Reproducibility in porosity extraction

Appendix B

B.1 Introduction

The study of bone porosity entailed exposure X-radiation and the detection of photons, reconstruction of hundreds of projections to obtain a 3D dataset and several image processing operations. In order to test accuracy of the results after the application of all these concatenated steps, a bone specimen was scanned twice with the same machine parameters and image processing operations were carried out on the datasets to extract porosity.

B.2 Results

Figure B.1 shows two reconstructed images from the two datasets that were obtained from the same bone sample with the same machine parameters.

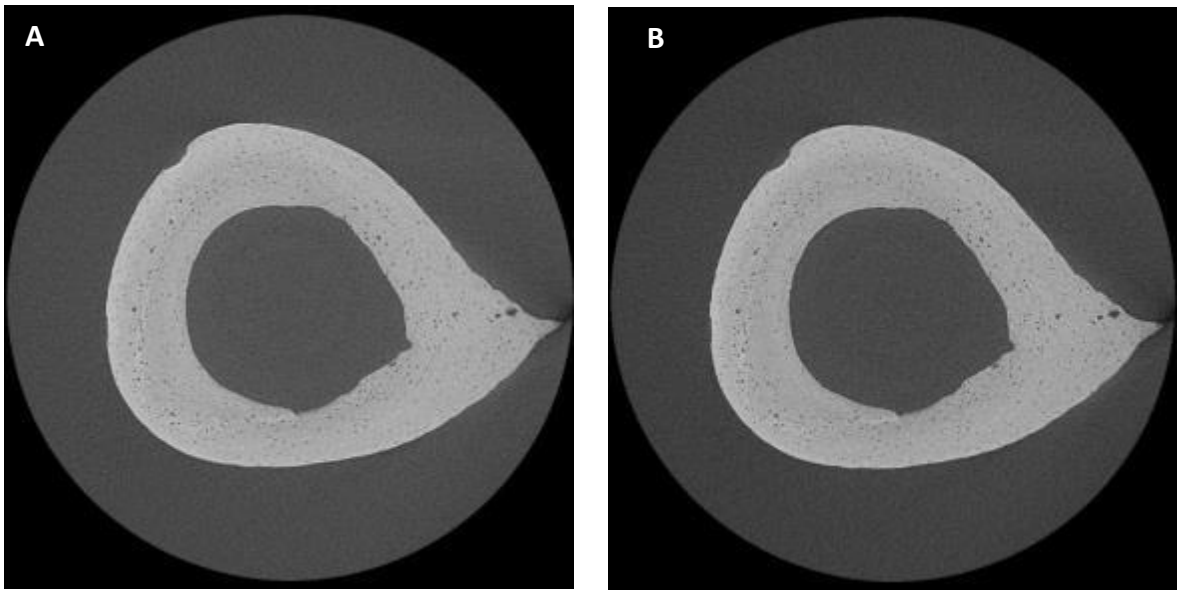

Figure B.1 Reconstructed images from the right tibia of a 15 weeks old C57BL6 female mouse – Data assessed at 1.7 µm voxel size. (A) Dataset 1 (B) dataset 2.

Datasets were thresholded to generate the binary images shown in Figure B.2.The porosity within the mineralised tissue was extracted from the binarised images shown in

Figure B.2 and the results are shown in Figure B.3. In order to see differences in porosity, the two images were compared, and the error image is shown in Figure B.4. A white pixel comes from a porosity pixel on image 1 that is a background pixel in image 2. A black pixel means that the pixel is porosity on image 2 and background on image 1. The fact that most of the pores are partially black and white on the error image means that most of the pores are present in both images. In most of the cases only some points of the boundary of the objects are detected as errors, this means that the object is present in both images, the error could be explained by differences in shape, volume or position of the object and could be reduced with a better alignment. Only objects that are completely white or black are pores that are not present on both images.

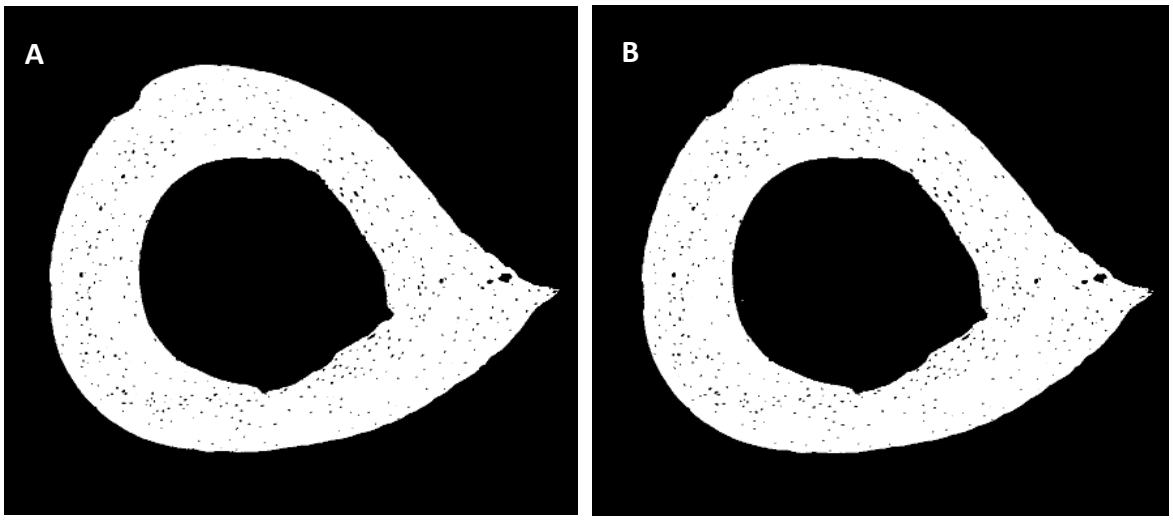

Figure B.2 Binarised images as a result of thresholding datasets in Figure B.1. Data assessed at 1.7 µm voxel size. (A) Dataset 1 and (B) dataset 2.

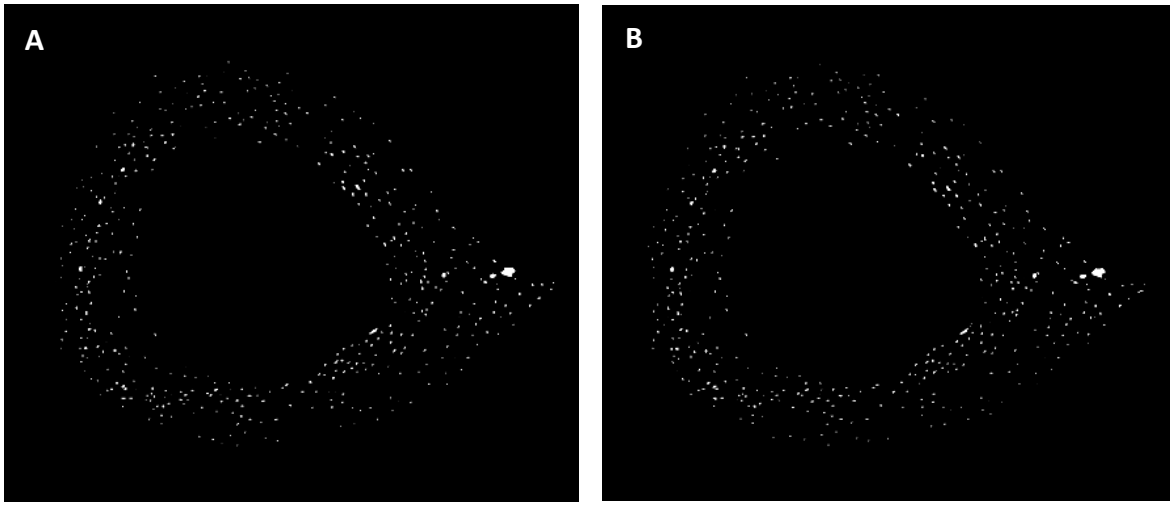

Figure B.3. Porosity images from the datasets in Figure B.1. Data assessed at 1.7 µm voxel size. (A) Dataset 1 and (B) dataset 2.

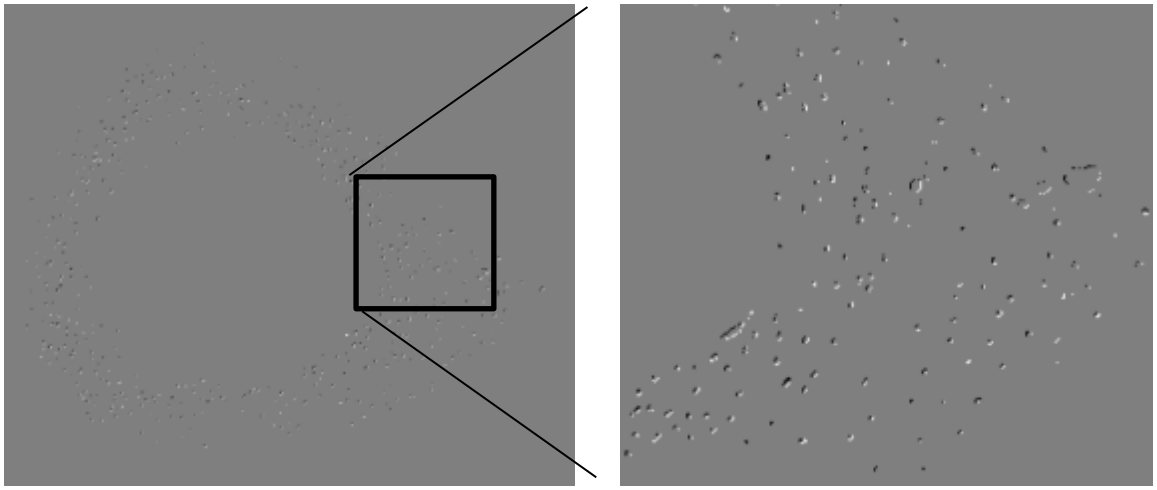

Figure B.4. Error image as a result of computing the difference between images 1 and 2. White and black pixels represent mismatch between the two images.

Even if it is possible to find objects completely white or black on the slices, it does not necessary mean that the pore is not present in one of the images. This could be caused by differences in shape, size and position in z direction or by a lack of alignment. In order to

further investigate this in 3D, 6 regions of interest were randomly selected and the 3D objects within them counted. Table B.1 summarises the results.

Appendix B

	Dataset 1	Dataset 2	Error (%)
Region 1 (100^3 voxels)	290	290	0
Region 2 (100^3 voxels)	254	257	1.17
Region 3 (100^3 voxels)	238	242	1.66
Region 4 (100^3 voxels)	227	227	0
Region 5 (100^3 voxels)	260	261	0.38
Region 6 (200^3 voxels)	1610	1609	0.06

Table B.1. 3D objects counting results for the reproducibility analysis in the extraction of cortical porosity.

Appendix B

References

Åkesson K, Marsh D, Mitchell PJ, McLellan AR, Stenmark J, Pierroz DD, Kyer C, Cooper C (2013) Capture the Fracture: a Best Practice Framework and global campaign to break the fragility fracture cycle. Osteoporos. Int. **24**: 2135–2152.

Alagiakrishnan K, Juby A, Hanley D, Tymchak W, Sclater A (2003) Role of vascular factors in osteoporosis. J. Gerontol. A. Biol. Sci. Med. Sci. **58**: 362–366.

Arnett TR (2010) Acidosis, hypoxia and bone. Arch. Biochem. Biophys. **503**: 103–109.

Arnett TR, Gibbons DC, Utting JC, Orriss IR, Hoebertz A, Rosendaal M, Meghji S (2003) Hypoxia is a major stimulator of osteoclast formation and bone resorption. J. Cell. Physiol. **196**: 2–8.

Aspenberg P, Schilcher J (2014) Atypical femoral fractures, bisphosphonates, and mechanical stress. Curr. Osteoporos. Rep. **12**: 189–193.

Barth HD, Launey ME, Macdowell AA, Ager JW 3rd, Ritchie RO (2010) On the effect of X-ray irradiation on the deformation and fracture behavior of human cortical bone. Bone **46**: 1475–1485.

Barth HD, Zimmermann EA, Schaible E, Tang SY, Alliston T, Ritchie RO (2011) Characterization of the effects of x-ray irradiation on the hierarchical structure and mechanical properties of human cortical bone. Biomaterials **32**: 8892–8904.

Barth RW, Williams JL, Kaplan FS (1992) Osteon morphometry in females with femoral neck fractures. Clin. Orthop. Relat. Res. **283**: 178–186.

Bell KL, Loveridge N, Power J, Garrahan N, Meggitt BF, Reeve J (1999) Regional differences in cortical porosity in the fractured femoral neck. Bone **24**: 57–64.

Bellido T, Jilka RL, Boyce BF, Girasole G, Broxmeyer H, Dalrymple SA, Murray R, Manolagas SC (1995) Regulation of interleukin-6, osteoclastogenesis, and bone mass by androgens. The role of the androgen receptor. J. Clin. Invest. **95**: 2886–2895.

Berman AG, Clauser CA, Wunderlin C, Hammond MA, Wallace JM (2015) Structural and Mechanical Improvements to Bone Are Strain Dependent with Axial Compression of the Tibia in Female C57BL/6 Mice. Ed. Deepak Vashishth. PLoS One **10**: e0130504.

Blahos J (2007) Treatment and prevention of osteoporosis. Wien. Med. Wochenschr. **157**: 589–592.

References

Boskey AL, Coleman R (2010) Critical reviews in oral biology & medicine: Aging and bone. J. Dent. Res.

Bouxsein ML, Boyd SK, Christiansen BA, Guldberg RE, Jepsen KJ, Muller R (2010) Guidelines for assessment of bone microstructure in rodents using micro-computed tomography. J. Bone Miner. Res. **25**: 1468–1486.

Britz HM, Jokihaara J, Leppanen O V, Jarvinen T, Cooper DML (2010) 3D visualization and quantification of rat cortical bone porosity using a desktop micro-CT system: a case study in the tibia. J. Microsc. **240**: 32–37.

Britz HM, Jokihaara J, Leppanen O V, Jarvinen TLN, Cooper DML (2012) The effects of immobilization on vascular canal orientation in rat cortical bone. J. Anat. **220**: 67–76.

Brommage R, Liu J, Hansen GM, Kirkpatrick LL, Potter DG, Sands AT, Zambrowicz B, Powell DR, Vogel P (2014) High-throughput screening of mouse gene knockouts identifies established and novel skeletal phenotypes. Bone Res. **2**: 14034.

Burkhardt R, Kettner G, Bohm W, Schmidmeier M, Schlag R, Frisch B, Mallmann B, Eisenmenger W, Gilg T (1987) Changes in trabecular bone, hematopoiesis and bone marrow vessels in aplastic anemia, primary osteoporosis, and old age: a comparative histomorphometric study. Bone **8**: 157–164.

Burr DB (2016) Cortical bone: a target for fracture prevention? Lancet **375**: 1672–1673.

Campbell GM, Sophocleous A (2014) Quantitative analysis of bone and soft tissue by micro-computed tomography: applications to ex vivo and in vivo studies. BoneKEy Rep **3**: 564.

Carano RAD, Filvaroff EH (2003) Angiogenesis and bone repair. Drug Discov. Today **8**: 980–989.

Carmeliet P, Ferreira V, Breier G, Pollefeyt S, Kieckens L, Gertsenstein M, Fahrig M, Vandenhoeck A, Harpal K, Eberhardt C, Declercq C, Pawling J, Moons L, Collen D, Risau W, Nagy A (1996) Abnormal blood vessel development and lethality in embryos lacking a single VEGF allele. Nature **380**: 435–439.

Carulli C, Innocenti M, Brandi ML (2013) Bone vascularization in normal and disease conditions. Front. Endocrinol. (Lausanne). **4**: 106.

de Castro LF, Maycas M, Bravo B, Esbrit P, Gortazar A (2015) VEGF Receptor 2 (VEGFR2) Activation Is Essential for Osteocyte Survival Induced by Mechanotransduction. J. Cell. Physiol. **230**: 278–285.

References

Chapman D, Thomlinson W, Johnston RE, Washburn D, Pisano E, Gmür N, Zhong Z, Menk R, Arfelli F, Sayers D (1997) Diffraction enhanced x-ray imaging. Phys. Med. Biol. **42**: 2015–25.

Chigurupati S, Kulkarni T, Thomas S, Shah G (2005) Calcitonin stimulates multiple stages of angiogenesis by directly acting on endothelial cells. Cancer Res. **65**: 8519–8529.

Clarke B (2008) Normal bone anatomy and physiology. Clin. J. Am. Soc. Nephrol. **3 Suppl 3**: S131-9.

Clarke BL, Khosla S (2010) Physiology of Bone Loss. Radiol. Clin. North Am. **48**: 483-95

Clarkin CE, Emery RJ, Pitsillides AA, Wheeler-Jones CPD (2008) Evaluation of VEGF-mediated signaling in primary human cells reveals a paracrine action for VEGF in osteoblast-mediated crosstalk to endothelial cells. J. Cell. Physiol. **214**: 537–544.

Clarkin CE, Gerstenfeld LC (2013) VEGF and bone cell signalling: an essential vessel for communication? Cell Biochem. Funct. **31**: 1–11.

Cleaver O, Melton DA (2003) Endothelial signaling during development. Nat Med **9**: 661–668.

Cloetens P, Ludwig W, Baruchel J, Van Dyck D, Van Landuyt J, Guigay JP, Schlenker M (1999) Holotomography: Quantitative phase tomography with micrometer resolution using hard synchrotron radiation x rays. Appl. Phys. Lett. **75**: 2912–2914.

Cooper C, Mitchell P, Kanis JA (2011) Breaking the fragility fracture cycle. Osteoporos. Int. **22**: 2049-2050.

Cooper DML, Turinsky AL, Sensen CW, Hallgrímsson B (2003) Quantitative 3D analysis of the canal network in cortical bone by micro-computed tomography. Anat. Rec. Part B New Anat. **274B**: 169–179.

Cooper DML, Thomas CDL, Clement JG, Turinsky AL, Sensen CW, Hallgrimsson B (2007a) Age-dependent change in the 3D structure of cortical porosity at the human femoral midshaft. Bone **40**: 957–965.

Cooper D, Turinsky A, Sensen C, Hallgrimsson B (2007b) Effect of voxel size on 3D micro-CT analysis of cortical bone porosity. Calcif. Tissue Int. **80**: 211–219.

Courtland H-W, Kennedy OD, Wu Y, Gao Y, Sun H, Schaffler MB, Yakar S (2013) Low levels of plasma IGF-1 inhibit intracortical bone remodeling during aging. Age (Dordr). **35**: 1691–1703.

Le Couteur DG, Lakatta EG (2010) A Vascular Theory of Aging. Journals Gerontol. Ser. A Biol. Sci. Med. Sci. **65A**: 1025–1027.

References

Cowin SC (1999) Bone poroelasticity. J. Biomech. **32**: 217–238.

Cummings SR, Melton LJ (2002) Osteoporosis I: Epidemiology and outcomes of osteoporotic fractures. Lancet. **359**: 1761-1767.

Dandajena TC, Ihnat MA, Disch B, Thorpe J, Currier GF (2012) Hypoxia triggers a HIF-mediated differentiation of peripheral blood mononuclear cells into osteoclasts. Orthod. Craniofac. Res. **15**: 1–9.

Davis TRC, Wood MB (1992) Endothelial control of long bone vascular resistance. J. Orthop. Res. **10**: 344–349.

Dawson-Hughes B, Fuleihan GE-H, Clark P (2013) Bone care for the postmenopausal woman. Int. Osteoporos. Found. **1**: 1-28.

Demontiero O, Vidal C, Duque G (2012) Aging and bone loss: New insights for the clinician. Ther. Adv. Musculoskelet. Dis. **4**: 61-76.

Dempster DW, Compston JE, Drezner MK, Glorieux FH, Kanis JA, Malluche H, Meunier PJ, Ott SM, Recker RR, Parfitt AM (2013) Standardized Nomenclature, Symbols, and Units for Bone Histomorphometry: A 2012 Update of the Report of the ASBMR Histomorphometry Nomenclature Committee. J. Bone Miner. Res. **28**: 2–17.

Dierolf M, Menzel A, Thibault P, Schneider P, Kewish CM, Wepf R, Bunk O, Pfeiffer F (2010) Ptychographic X-ray computed tomography at the nanoscale. Nature **467**: 436–439.

Dinenno FA, Jones PP, Seals DR, Tanaka H (1999) Limb blood flow and vascular conductance are reduced with age in healthy humans: relation to elevations in sympathetic nerve activity and declines in oxygen demand. Circulation **100**: 164–170.

Ding W, Wei Z, Liu J (2011) Reduced local blood supply to the tibial metaphysis is associated with ovariectomy-induced osteoporosis in mice. Connect. Tissue Res. **52**: 25–29.

Dong P, Haupert S, Hesse B, Langer M, Gouttenoire PJ, Bousson V, Peyrin F (2014) 3D osteocyte lacunar morphometric properties and distributions in human femoral cortical bone using synchrotron radiation micro-CT images. Bone **60**: 172–185.

Efimenko A, Starostina E, Kalinina N, Stolzing A (2011) Angiogenic properties of aged adipose derived mesenchymal stem cells after hypoxic conditioning. J. Transl. Med. **9**: 10.

Evans FG, Bang S (1967) Differences and relationships between the physical properties and the microscopic structure of human femoral, tibial and fibular cortical bone. Am. J. Anat. **120**: 79–88.

References

Fei J, Peyrin F, Malaval L, Vico L, Lafage-Proust M-H (2010) Imaging and quantitative assessment of long bone vascularization in the adult rat using microcomputed tomography. Anat. Rec. (Hoboken). **293**: 215–224.

Felder AA, Phillips C, Cornish H, Cooke M, Hutchinson JR, Doube M (2017) Secondary Osteons Scale Allometrically In Mammalian Humerus And Femur. R Soc Open Sci. **4**: 170431.

Ferguson VL, Ayers RA, Bateman TA, Simske SJ (2003) Bone development and age-related bone loss in male C57BL/6J mice. Bone **33**: 387–398.

Ferrara N, Carver-Moore K, Chen H, Dowd M, Lu L, O'Shea KS, Powell-Braxton L, Hillan KJ, Moore MW (1996) Heterozygous embryonic lethality induced by targeted inactivation of the VEGF gene. Nature **380**: 439–442.

Ferretti JL, Frost HM, Gasser JA, High WB, Jee WS, Jerome C, Mosekilde L, Thompson DD (1995) Perspectives on osteoporosis research: its focus and some insights from a new paradigm. Calcif. Tissue Int. **57**: 399-404.

Fogelman I, Blake GM (2000) Different approaches to bone densitometry. J. Nucl. Med. **41**: 2015–2025.

Fratini M, Bukreeva I, Campi G, Brun F, Tromba G, Modregger P, Bucci D, Battaglia G, Spanò R, Mastrogiacomo M, Requardt H, Giove F, Bravin A, Cedola A (2015) Simultaneous submicrometric 3D imaging of the micro-vascular network and the neuronal system in a mouse spinal cord. Sci. Rep. **5**: 8514.

Garlanda C, Dejana E (1997) Heterogeneity of Endothelial Cells. Arterioscler. Thromb. Vasc. Biol. **17**: 1193 LP-1202.

Georgiadis M, Muller R, Schneider P (2016) Techniques to assess bone ultrastructure organization: orientation and arrangement of mineralized collagen fibrils. J. R. Soc. Interface **13**: 20160088.

Gerard J. Tortora, Nielsen M (2013) Principles of Human Anatomy 13th Editi. WILEY.

Gerber HP, Hillan KJ, Ryan AM, Kowalski J, Keller GA, Rangell L, Wright BD, Radtke F, Aguet M, Ferrara N (1999) VEGF is required for growth and survival in neonatal mice. Development **126**: 1149–1159.

Giorgio Margaritondo (2002) Elements of Synchrotron Light: For Biology, Chemistry, and Medical Research. Oxford: Oxford University Press.

Glowacki J (1998) Angiogenesis in fracture repair. Clin. Orthop. Relat. Res.: S82-9.

References

Goggin PM, Zygalakis KC, Oreffo RO, Schneider P (2016) High-resolution 3D imaging of osteocytes and computational modelling in mechanobiology: insights on bone development, ageing, health and disease. Eur. Cell. Mater. **31**: 264–295.

Gonzalez-Tendero A, Zhang C, Balicevic V, Cardenes R, Loncaric S, Butakoff C, Paun B, Bonnin A, Garcia-Canadilla P, Munoz-Moreno E, Gratacos E, Crispi F, Bijnens B (2017) Whole heart detailed and quantitative anatomy, myofibre structure and vasculature from X-ray phase-contrast synchrotron radiation-based micro computed tomography. Eur. Heart J. Cardiovasc. Imaging **18**: 732–741.

Al Hadi H, Smerdon GR, Fox SW (2013) Hyperbaric oxygen therapy suppresses osteoclast formation and bone resorption. J. Orthop. Res. **31**: 1839–1844.

Halloran BP, Ferguson VL, Simske SJ, Burghardt A, Venton LL, Majumdar S (2002) Changes in Bone Structure and Mass With Advancing Age in the Male C57BL/6J Mouse. J. Bone Miner. Res. **17**: 1044–1050.

Ham AW (1952) Some histophysiological problems peculiar to calcified tissues. J. Bone Joint Surg. Am. **34**: 701–728.

Ham AW (1953) Histology. Philadelphia: Lippincott.

Hannah KM, Thomas CDL, Clement JG, De Carlo F, Peele AG (2010) Bimodal distribution of osteocyte lacunar size in the human femoral cortex as revealed by micro-CT. Bone **47**: 866–871.

Hernandez CJ, Beaupre GS, Carter DR (2000) A model of mechanobiologic and metabolic influences on bone adaptation. J. Rehabil. Res. Dev. **37**: 235–244.

Holguin N, Brodt MD, Silva MJ (2016) Activation of Wnt Signaling by Mechanical Loading Is Impaired in the Bone of Old Mice. J. Bone Miner. Res. **31**: 2215–2226.

Holzer G, von Skrbensky G, Holzer LA, Pichl W (2009) Hip fractures and the contribution of cortical versus trabecular bone to femoral neck strength. J. Bone Miner. Res. **24**: 468–474.

Hsieh J (2009) Computed Tomography Principles, Design, Artifacts, and Recent Advances Second Edi. WILEY.

Hu J, Li P, Yin X, Wu T, Cao Y, Yang Z, Jiang L, Hu S, Lu H (2017) Nondestructive imaging of the internal microstructure of vessels and nerve fibers in rat spinal cord using phase-contrast synchrotron radiation microtomography. J. Synchrotron Radiat. **24**: 482–489.

References

Hu K, Olsen BR (2016a) Osteoblast-derived VEGF regulates osteoblast differentiation and bone formation during bone repair. J. Clin. Invest. **126**: 509–526.

Hu K, Olsen BR (2016b) The roles of vascular endothelial growth factor in bone repair and regeneration. Bone. **91**: 30-38.

Hughes DE, Dai A, Tiffee JC, Li HH, Mundy GR, Boyce BF (1996) Estrogen promotes apoptosis of murine osteoclasts mediated by TGF-beta. Nat. Med. **2**: 1132–1136.

Isowa S, Shimo T, Ibaragi S, Kurio N, Okui T, Matsubara K, Hassan NMM, Kishimoto K, Sasaki A (2010) PTHrP regulates angiogenesis and bone resorption via VEGF expression. Anticancer Res. **30**: 2755–2767.

Jaffe HL (1930) The resorption of bone: A consideration of the underlying processes particularly in pathologic conditions. Arch. Surg. **20**: 355–385.

Javaheri B, Carriero A, Staines KA, Chang Y-M, Houston DA, Oldknow KJ, Millan JL, Kazeruni BN, Salmon P, Shefelbine S, Farquharson C, Pitsillides AA (2015) Phospho1 deficiency transiently modifies bone architecture yet produces consistent modification in osteocyte differentiation and vascular porosity with ageing. Bone **81**: 277–291.

Jee WS, Yao W (2001) Overview: animal models of osteopenia and osteoporosis. J. Musculoskelet. Neuronal Interact. **1**: 193–207.

Jiang S, Kh Haider H, Ahmed RPH, Idris NM, Salim A, Ashraf M (2008) Transcriptional profiling of young and old mesenchymal stem cells in response to oxygen deprivation and reparability of the infarcted myocardium. J. Mol. Cell. Cardiol. **44**: 582–596.

Johnell O, Kanis JA (2006) An estimate of the worldwide prevalence and disability associated with osteoporotic fractures. Osteoporos. Int. **17**: 1726–1733.

Joseph P. Weinmann (1955) Bone and bones: Fundamentals of Bone Biology. Br. J. Surg. **43**: 224.

Kalu DN (1991) The ovariectomized rat model of postmenopausal bone loss. Bone Miner. **15**: 175–191.

Kanis JA, Johnell O (2005) Requirements for DXA for the management of osteoporosis in Europe. Osteoporos. Int. **16**: 229–238.

Kanis JA (2002) Diagnosis of osteoporosis and assessment of fracture risk. Lancet **359**: 1929–1936.

Kusumbe AP, Ramasamy SK, Adams RH (2014) Coupling of angiogenesis and osteogenesis by a specific vessel subtype in bone. Nature **507**: 323–328.

Lespessailles E, Ibrahim-Nasser N, Toumi H, Chapurlat R (2017) Contribution of high

resolution peripheral quantitative CT to the management of bone and joint diseases. Joint. Bone. Spine. In press.

Liu XS, Zhang XH, Sekhon KK, Adams MF, McMahon DJ, Bilezikian JP, Shane E, Guo XE (2010) High-resolution peripheral quantitative computed tomography can assess microstructural and mechanical properties of human distal tibial bone. J. Bone Miner. Res. **25**: 746–756.

Liu Y, Berendsen AD, Jia S, Lotinun S, Baron R, Ferrara N, Olsen BR (2012) Intracellular VEGF regulates the balance between osteoblast and adipocyte differentiation. J. Clin. Invest. **122**: 3101–3113.

Losordo DW, Isner JM (2001) Estrogen and angiogenesis: A review. Arterioscler. Thromb. Vasc. Biol. **21**: 6–12.

Lovric G, Oberta P, Mohacsi I, Stampanoni M, Mokso R (2014) A robust tool for photon source geometry measurements using the fractional Talbot effect. Opt. Express **22**: 2745–2760.

M.D. Abràmoff; P.J. Magalhães; S.J. Ram (2004) Image Processing with ImageJ. Biophotonics Int. **11**: 36–42.

MacNabb C, Patton D, Hayes JS (2016) Sclerostin Antibody Therapy for the Treatment of Osteoporosis: Clinical Prospects and Challenges. J. Osteoporos. **2016**: 6217286.

Mader KS, Schneider P, Muller R, Stampanoni M (2013) A quantitative framework for the 3D characterization of the osteocyte lacunar system. Bone **57**: 142–154.

Maes C, Goossens S, Bartunkova S, Drogat B, Coenegrachts L, Stockmans I, Moermans K, Nyabi O, Haigh K, Naessens M, Haenebalcke L, Tuckermann JP, Tjwa M, Carmeliet P, Mandic V, David J-P, Behrens A, Nagy A, Carmeliet G, Haigh JJ (2010) Increased skeletal VEGF enhances beta-catenin activity and results in excessively ossified bones. EMBO J. **29**: 424–441.

Manolagas SC (2000) Birth and death of bone cells: basic regulatory mechanisms and implications for the pathogenesis and treatment of osteoporosis. Endocr. Rev. **21**: 115–137.

Marenzana M, Arnett TR (2013) The Key Role of the Blood Supply to Bone. Bone Res. **1**: 203–215.

Marieb EN (2015) Essential of Human Anatomy & Physiology. Pearson. Vol. 11.

References

Martin RB (2003) Fatigue damage, remodeling, and the minimization of skeletal weight. J. Theor. Biol. **220**: 271–276.

Masi L (2008) Epidemiology of osteoporosis. Clin. Cases Miner. Bone Metab. **5**: 11–3.

Matrecano M (2011) Porous media characterization by micro - tomographic image processing. Università degli Studi di Napoli Federico II. Thesis. 1-126

Matsuo K, Irie N (2008) Osteoclast-osteoblast communication. Arch. Biochem. Biophys. **473**: 201–209.

Mayo SC, Stevenson AW, Wilkins SW (2012) In-Line Phase-Contrast X-ray Imaging and Tomography for Materials Science. Materials (Basel). **5**: 937–965.

Mazess RB (1990) Fracture risk: a role for compact bone. Calcif. Tissue Int. **47**: 191-193.

Mekraldi S, Lafage-Proust M-H, Bloomfield S, Alexandre C, Vico L (2003) Changes in vasoactive factors associated with altered vessel morphology in the tibial metaphysis during ovariectomy-induced bone loss in rats. Bone **32**: 630–641.

Mithal A, Lau E (2009) The Asia Audit: Epidemiology, costs and burden of osteoporosis in Asia. Int. J. Oral Sci. Annual Report.

Müller R (2003) Bone microarchitecture assessment: current and future trends. Osteoporos. Int. **14 Suppl 5**: S89-S95; discussion S95-S99.

van Oers RFM, Ruimerman R, Tanck E, Hilbers PAJ, Huiskes R (2008) A unified theory for osteonal and hemi-osteonal remodeling. Bone **42**: 250–259.

Ollion J, Cochennec J, Loll F, Escude C, Boudier T (2013) TANGO: a generic tool for high-throughput 3D image analysis for studying nuclear organization. Bioinformatics **29**: 1840–1841.

Olubamiji AD, Zhu N, Chang T, Nwankwo CK, Izadifar Z, Honaramooz A, Chen X, Eames BF (2017) Traditional Invasive and Synchrotron-Based Noninvasive Assessments of Three-Dimensional-Printed Hybrid Cartilage Constructs In Situ. Tissue Eng. Part C. Methods **23**: 156–168.

Palacio-Mancheno PE, Larriera AI, Doty SB, Cardoso L, Fritton SP (2014) 3D assessment of cortical bone porosity and tissue mineral density using high-resolution μcT: Effects of resolution and threshold method. J. Bone Miner. Res. **29**: 142–150.

References

Parfitt AM (2013) Chapter 36 - Skeletal Heterogeneity and the Purposes of Bone Remodeling: Implications for the Understanding of Osteoporosis. In , ed. Robert MarcusDavid FeldmanDavid W DempsterMarjorie LuckeyJane A B T - Osteoporosis (Fourth Edition) Cauley, 855–872.

Parfitt AM (1994) Osteonal and hemi-osteonal remodeling: the spatial and temporal framework for signal traffic in adult human bone. J. Cell. Biochem. **55**: 273–286.

Parfitt AM (2000) The mechanism of coupling: a role for the vasculature. Bone **26**: 319–323.

Parfitt AM, Drezner MK, Glorieux FH, Kanis JA, Malluche H, Meunier PJ, Ott SM, Recker RR (1987) Bone histomorphometry: standardization of nomenclature, symbols, and units. Report of the ASBMR Histomorphometry Nomenclature Committee. J. Bone Miner. Res. **2**: 595–610.

Pereira AF, Javaheri B, Pitsillides AA, Shefelbine SJ (2015) Predicting cortical bone adaptation to axial loading in the mouse tibia. J. R. Soc. Interface **12**: 20150590.

Pfeiffer F, Weitkamp T, Bunk O, David C (2006) Phase retrieval and differential phase-contrast imaging with low-brilliance X-ray sources. Nat. Phys. **2**: 258–261.

Pola R, Aprahamian TR, Bosch-Marce M, Curry C, Gaetani E, Flex A, Smith RC, Isner JM, Losordo DW (2004) Age-dependent VEGF expression and intraneural neovascularization during regeneration of peripheral nerves. Neurobiol. Aging **25**: 1361–1368.

Prasad J, Wiater BP, Nork SE, Bain SD, Gross TS (2010) Characterizing gait induced normal strains in a murine tibia cortical bone defect model. J. Biomech. **43**: 2765–2770.

Prasadam I, Zhou Y, Du Z, Chen J, Crawford R, Xiao Y (2014) Osteocyte-induced angiogenesis via VEGF-MAPK-dependent pathways in endothelial cells. Mol. Cell. Biochem. **386**: 15–25.

Pufe T, Claassen H, Scholz-Ahrens KE, Varoga D, Drescher W, Franke ATM, Wruck C, Petersen W, Cellarius C, Schrezenmeir J, Gluer C-C (2007) Influence of estradiol on vascular endothelial growth factor expression in bone: a study in Gottingen miniature pigs and human osteoblasts. Calcif. Tissue Int. **80**: 184–191.

Rajendran P, Rengarajan T, Thangavel J, Nishigaki Y, Sakthisekaran D, Sethi G, Nishigaki I (2013) The Vascular Endothelium and Human Diseases. Int. J. Biol. Sci. **9**: 1057–1069.

References

Reeve J, Arlot M, Wootton R, Edouard C, Tellez M, Hesp R, Green JR, Meunier PJ (1988) Skeletal blood flow, iliac histomorphometry, and strontium kinetics in osteoporosis: a relationship between blood flow and corrected apposition rate. J. Clin. Endocrinol. Metab. **66**: 1124–1131.

Rivard A, Fabre JE, Silver M, Chen D, Murohara T, Kearney M, Magner M, Asahara T, Isner JM (1999) Age-dependent impairment of angiogenesis. Circulation **99**: 111–120.

Roche B, David V, Vanden-Bossche A, Peyrin F, Malaval L, Vico L, Lafage-Proust M-H (2012) Structure and quantification of microvascularisation within mouse long bones: What and how should we measure? Bone **50**: 390–399.

Rockville; Office of the Surgeon General (US) (2004) Bone Health and Osteoporosis: A Report of the Surgeon General. Rockville (MD): Reports of the Surgeon General.

Saha S, Hayes WC (1977) Relations between tensile impact properties and microstructure of compact bone. Calcif. Tissue Res. **24**: 65–72.

Schambach SJ, Bag S, Schilling L, Groden C, Brockmann M a (2010) Application of micro-CT in small animal imaging. Methods **50**: 2–13.

Schneider P, Krucker T, Meyer E, Ulmann-Schuler A, Weber B, Stampanoni M, Müller R (2009) Simultaneous 3D visualization and quantification of murine bone and bone vasculature using micro-computed tomography and vascular replica. Microsc. Res. Tech. **72**: 690–701.

Schneider P, Mohan N, Stampanoni M, Muller R (2004) Soft-tissue and phase-contrast imaging at the Swiss Light Source. In , **5368:** 281–291.

Schneider P, Stauber M, Voide R, Stampanoni M, Donahue LR (2007) Ultrastructural Properties in Cortical Bone Vary Greatly in Two Inbred Strains of Mice as Assessed by Synchrotron Light Based Micro- and Nano-CT **22**: 1557–70.

Schneider P, Voide R, Stampanoni M, Donahue LR, Müller R (2013) The importance of the intracortical canal network for murine bone mechanics. Bone **53**: 120–8.

Senel K, Baykal T, Seferoglu B, Altas EU, Baygutalp F, Ugur M, Kiziltunc A (2013) Circulating vascular endothelial growth factor concentrations in patients with postmenopausal osteoporosis. Arch. Med. Sci. **9**: 709–712.

Silbermann M, Weiss A, Reznick AZ, Eilam Y, Szydel N, Gershon D (1987) Age-related trend for osteopenia in femurs of female C57BL/6 mice. Compr. Gerontol. A. **1**: 45–51.

Somerville JM, Aspden RM, Armour KE, Armour KJ, Reid DM (2004) Growth of C57BL/6 mice and the material and mechanical properties of cortical bone from the tibia. Calcif. Tissue Int. **74**: 469–475.

References

De Souza RL, Matsuura M, Eckstein F, Rawlinson SCF, Lanyon LE, Pitsillides AA (2005) Non-invasive axial loading of mouse tibiae increases cortical bone formation and modifies trabecular organization: A new model to study cortical and cancellous compartments in a single loaded element. Bone **37**: 810–818.

Stevenson JC (2011) Prevention of osteoporosis: one step forward, two steps back. Menopause Int. **17**: 137–141.

Ström O, Borgström F, Kanis J, Compston J, Cooper C, McCloskey E, Jönsson B (2011) Osteoporosis: burden, health care provision and opportunities in the EU. Arch. Osteoporos. **6**: 59–155. doi:10.1007/s11657-011-0060-1.

Taylor D (2000) Scaling effects in the fatigue strength of bones from different animals. J. Theor. Biol. **206**: 299–306.

Terribile F, FitzPatrick EA (1992) The application of multilayer digital image processing techniques to the description of soil thin sections. Geoderma **55**: 159–174.

Thurner PJ (2009) Atomic force microscopy and indentation force measurement of bone. Wiley Interdiscip. Rev. Nanomed. Nanobiotechnol. **1**: 624–649.

Thurner PJ, Chen CG, Ionova-Martin S, Sun L, Harman A, Porter A, Ager JW, Ritchie RO, Alliston T (2010) Osteopontin deficiency increases bone fragility but preserves bone mass. Bone **46**: 1564–73.

Tommasini SM, Trinward A, Acerbo AS, de Carlo F, Miller LM, Judex S (2012) Changes in intracortical microporosities induced by pharmaceutical treatment of osteoporosis as detected by high resolution micro-CT. Bone **50**: 596–604.

Utting JC, Robins SP, Brandao-Burch A, Orriss IR, Behar J, Arnett TR (2006) Hypoxia inhibits the growth, differentiation and bone-forming capacity of rat osteoblasts. Exp. Cell Res. **312**: 1693–1702.

Utting JC, Flanagan AM, Brandao-Burch A, Orriss IR, Arnett TR (2010) Hypoxia stimulates osteoclast formation from human peripheral blood. Cell Biochem. Funct. **28**: 374–380.

Varray F, Mirea I, Langer M, Peyrin F, Fanton L, Magnin IE (2017) Extraction of the 3D local orientation of myocytes in human cardiac tissue using X-ray phase-contrast micro-tomography and multi-scale analysis. Med. Image Anal. **38**: 117–132.

Vaughan TJ, Verbruggen SW, McNamara LM (2013) Are all osteocytes equal? Multiscale modelling of cortical bone to characterise the mechanical stimulation of osteocytes. Int. j. numer. method. biomed. eng. **29**: 1361–1372.

References

Verbruggen SW, Vaughan TJ, McNamara LM (2012) Strain amplification in bone mechanobiology: a computational investigation of the in vivo mechanics of osteocytes. J. R. Soc. Interface **9**: 2735–2744.

Wachter NJ, Augat P, Krischak GD, Sarkar MR, Mentzel M, Kinzl L, Claes L (2001) Prediction of strength of cortical bone in vitro by microcomputed tomography. Clin. Biomech. (Bristol, Avon) **16**: 252–256.

Warner SE, Sanford DA, Becker BA, Bain SD, Srinivasan S, Gross TS (2006) Botox induced muscle paralysis rapidly degrades bone. Bone **38**: 257–264.

Weiner S, Wagner D. H (1998) THE MATERIAL BONE: Structure-Mechanical Function Relations. Annu. Rev. Mater. Sci. **28**: 271–298.

Weiss A, Arbell I, Steinhagen-Thiessen E, Silbermann M (1991) Structural changes in aging bone: osteopenia in the proximal femurs of female mice. Bone **12**: 165–172.

Weitkamp T, Haas D, Wegrzynek D, Rack A (2011) ANKAphase: software for single-distance phase retrieval from inline X-ray phase-contrast radiographs. J. Synchrotron Radiat. **18**: 617–629.

Weitkamp T, Diaz A, David C, Pfeiffer F, Stampanoni M, Cloetens P, Ziegler E (2005) X-ray phase imaging with a grating interferometer. Opt. Express **13**: 6296.

Wilson A, Shehadeh LA, Yu H, Webster KA (2010) Age-related molecular genetic changes of murine bone marrow mesenchymal stem cells. BMC Genomics **11**: 229.

Yao Z, Lafage-Proust M-H, Plouet J, Bloomfield S, Alexandre C, Vico L (2004) Increase of both angiogenesis and bone mass in response to exercise depends on VEGF. J. Bone Miner. Res. **19**: 1471–1480.

Young KA, Womble M, Wise JA, DeSaix P, Kruse DH, Poe B, Johnson E, Johnson JE, Korol O, Betts JG (2003) Anatomy & Physiology. OpenStax College.

Zebaze R, Seeman E (2015) Cortical bone: a challenging geography. J. Bone Miner. Res. **30**: 24–9.

Zeller-Plumhoff B, Roose T, Clough GF, Schneider P (2017a) Image-based modelling of skeletal muscle oxygenation. J. R. Soc. Interface **14**: 20160992.

Zeller-Plumhoff B, Roose T, Katsamenis OL, Mavrogordato MN, Torrens C, Schneider P, Clough GF (2017b) Phase contrast synchrotron radiation computed tomography of muscle spindles in the mouse soleus muscle. J. Anat. **230**: 859–865.

Zhang J, Liu W, Ye P, D'Ercole AJ (2007) Pitfalls of PCR-based strategy for genotyping cre-loxP mice. Biotechniques. **42**: 281-282

References